

UNIVERSITY OF NAPLES “FEDERICO II”

DEPARTMENT OF CHEMICAL, MATERIALS AND INDUSTRIAL PRODUCTION
ENGINEERING



PHD IN INDUSTRIAL PRODUCT AND PROCESS ENGINEERING
XXXIV CYCLE

**Oil core- functionalized graphene oxide shell as
multifunctional theranostic nanotool for cancer
therapy**

Supervisor:

Prof. Dr. Paolo Antonio Netti

Advisor:

Dr. Ing. Raffaele Vecchione

Coordinator:

Prof. Andrea D'Anna

Candidate:

Immacolata Tufano

Academic year 2021/2022

Contents

List of Figures	vii
List of Tables	viii
List of Abbreviations	viii
1 nano-Graphene Oxide in Cancer Therapy	1
1.1 State of art	2
1.1.1 Synthetic Approaches	11
1.1.2 Mechanism of graphene oxide formation and breakage . .	17
1.1.3 Nano Graphene oxide in cancer therapy	21
1.1.4 Multi-stage approach in Cancer Therapy	26
1.1.5 Oil/Water Nanoemulsions (O/W NEs)	27
1.2 Aim of the PhD project	29
References	31
2 photo-Fenton reaction graphite ball milled to obtain nano-GO	42
2.1 Abstract	43
2.2 Introduction	44
2.3 Methods	47
2.3.1 Materials	47
2.3.2 Preparation of GO by Ball Milling	47
2.3.3 Photo-Fenton Reaction of GO Ball Milled	48
2.3.4 Instrumentations	48
2.4 Results	50

2.4.1	Synthesis	50
2.4.2	Morphological Characterization and Size Evaluation	51
2.4.3	Products Composition	56
2.5	Conclusion	61
2.6	Supporting Information	62
References		65
3	Optimize nano-Graphene Oxide for biological applications	71
3.1	Abstract	72
3.2	Introduction	72
3.3	Methods	75
3.3.1	Materials	75
3.3.2	Instrumentation	76
3.3.3	Graphene Oxide Preparation	78
3.3.4	Amino-modified GOQDs Preparation	78
3.3.5	Conjugation of GOQDs-NH ₂ with HA	79
3.3.6	Curcumin Loading and Release	79
3.3.7	Cell culture	80
3.3.8	GOQDs-NH ₂ and GOQDs-HA 3D Dermis Microtissue (HDF μ TPs) internalization	82
3.4	Results and Discussion	83
3.4.1	Amino-modified GOQDs Preparation	83
3.4.2	Conjugation of GOQDs-NH ₂ with HA	84
3.4.3	Morphological Characterization and Size Evaluation	85
3.4.4	Product Composition	91
3.4.5	Optical Properties	94
3.4.6	Curcumin loading and release	95
3.4.7	Cellular Internalization and Cell viability	98
3.4.8	GOQDs-NH ₂ and GOQDs-HA 3D Dermis Microtissue (HDF μ TPs) internalization	100
3.5	Conclusion	106
3.6	Supporting Information	107

References	110
4 Oil core- functionalized graphene oxide shell	115
4.1 Abstract	115
4.2 Introduction	115
4.3 Methods	119
4.3.1 Materials	119
4.3.2 Instrumentation	119
4.3.3 Oil/Water Nanoemulsion (O/WNE) preparation	121
4.3.4 Modification of Chitosan with Fluorescein Isothiocyanate .	121
4.3.5 Amino-modified GOQDs Preparation	122
4.3.6 GOQDs-Rhodamine B labelling	122
4.3.7 Conjugation of GOQDs-NH ₂ with HA	122
4.3.8 Layer by Layer GOQDs-HA Deposition on Secondary na- noEmulsion	123
4.3.9 Cell culture	123
4.4 Result and Discussion	125
4.4.1 GOQDs-HA coating Oil/Water secondary Emulsion	125
4.4.2 Cellular Internalization and Cell viability	133
4.5 Conclusion	136
4.6 Future Perspectives	136
References	138
5 Conclusion	142

List of Figures

1.1	Chemical structure of Graphene Oxide based on Lerf-Klinowski model	8
1.2	Bio-applications of Graphene Oxide in Cancer Therapy. Reproduced from Reference 33	9
1.3	Stage of conversion of bulk graphite in graphene oxide solution with corresponding micrographic images. Reproduced from ref. 75	19
1.4	Mechanism of the breakage by variation of reaction parameters. Reproduced from ref. 78	21
1.5	Mechanism of the breakage by ultrasonication. Reproduced from ref. 7	22
1.6	Illustration of photoluminescence mechanism of nano-GO	25
1.7	Schematic depiction of the multistage nanoparticle drug delivery system	27
1.8	Example of controlled deposition of polymeric multilayer film on oil core based nanocapsules	28
2.1	Graphite flakes (left), graphite ball milled (right) photographs . . .	51
2.2	SEM micrographs at different magnifications of (a,b) pristine graphite G; (c,d) GO ball milled GO_{bm} ; (e,f) GO-Fenton GO_{F32h}	52
2.3	EDX spectra of a) GO ball milled GO_{bm} ; b) GO Fenton GO_{F32h} . . .	53
2.4	Cryo-Tem image and Size Distribution GO_{F32h}	54
2.5	AFM Images (top) and height profile of the AFM images (bottom) of a) GO ball milled GO_{bm} ; b) GO Fenton GO_{F32h}	55
2.6	Low (left) and high (right) Frequency Raman spectra of G, GO_{bm} , and GO_{F32h}	56

2.7	XPS Survey spectra of a) G; b) GO _{bm} , c) GO _{F32h} ; d) spectra overlap	58
2.8	De-convoluted C1s core level XPS spectra for a) G; b) GO _{bm} , c) GO _{F32h}	59
2.9	FTIR spectra of G; GO _{bm} , GO _{F32h}	59
2.10	ζ potential values of GO _{bm} (a) and GO _{F32h} (b); UV-Vis absorption spectra GO _{bm} (red), GO _{F32h} (blue) (c); PL emission spectra λ _{EX} 335 nm (d)	60
2.11	DLS Size distribution GO _{bm} (left) and GO _{F32h} (right)	63
2.12	De-convoluted O1s core level XPS spectra for a) G, b) GO _{bm} , c) GO _{F32h}	63
3.1	TEM image and Size Distribution GO _{Hummer} (a), Cryo-TEM image and Size Distribution GOQDs-NH ₂ (b) and GOQDs-HA (c)	86
3.2	EDX spectra of a) GO _{Hummer} ; b) GOQDs-NH ₂ ; c)GOQDs-HA	87
3.3	AFM Images (left) and height profile of the AFM images (right) of a) GO _{Hummer} ; b) GOQDs-NH ₂ ; c)GOQDs-HA	88
3.4	a) Low (left) and high (right) Frequency Raman spectra of GO _{Hummer} ; GOQDs-NH ₂ ; GOQDs-HA; b,c,d) SAED pattern of GO _{Hummer} ; GOQDs-NH ₂ ; GOQDs-HA	89
3.5	XPS survey spectra of a) graphite; b) GO _{Hummer} ; c) GOQDs-NH ₂ ; d) GOQDs-HA	92
3.6	De-convoluted C1s core level XPS spectra for a) GO _{Hummer} ; b) GOQDs-NH ₂ ; c) GOQDs-HA	93
3.7	FTIR spectra of GOQDs-NH ₂ (blue) and GOQDs-HA (red)	94
3.8	a) Temporal evolution of PL emission during preparation of GOQDs-NH ₂ ; b) PL emission spectrum of GOQDs-NH ₂ , λ _{EX} 350 nm, λ _{EM} 370-650 nm; c) PL emission spectrum of GOQDs-NH ₂ , λ _{EX} 405nm, λ _{EM} 648-700 nm; d) UV-VIS	95
3.9	Cur release from a) GOQDs-NH ₂ , b) GOQDs-HA a pH 7.4 (blue), 5.5 (red)and a 60° C (orange)	97

3.10 a) Calibration curves from GOQDs-NH ₂ and GOQDs-HA; b) Internalization of GOQDs-NH ₂ (blue) and GOQDs-HA (orange) in MCF10A and MDA-MB231 cells; c) Internalization of GOQDs-NH ₂ (blue) and GOQDs-HA (orange) in HDFs cells	99
3.11 Cell viability of HDFs cell treated with 0.01mg/ml of GOQDs-NH ₂ and GOQDs-HA	100
3.12 a) Representative confocal images of HDFs cells incubated with GOQDs-HA-Rhod. b) Integrated fluorescence per unit area (Statistical comparisons were performed with a student's unpaired test. **, P < 0.01)	101
3.13 Confocal analysis GOQDs-HA-Rhod.B in 3D μ TPs after 24 h incubation at 0.1 mg/ml (top). Fluorescence Intensity Quantification .	103
3.14 Confocal analysis GOQDs-HA-Rhod.B in 3D μ TPs after 24 h incubation at 0.1 mg/ml (top). Fluorescence Intensity Quantification .	104
3.15 a) Life-Time (left) and Fluorescence Intensity (right) of μ TPs treated with GOQDs-HA-Rhod.B 0.1mg/ml from FRET analysis. b) Fluorescence spectra of supernatants obtained after GOQDs-HA-Rhod.B μ TPs incubation	105
3.16 Frame of the proceeding of the formation reaction of GOQDs-NH ₂ (top), GOQDs-NH ₂ obtained after purification (down)	107
3.17 De-convoluted O1s core level XPS spectra for a) GO _{Hummer} , b) GOQDs-NH ₂ , c) GOQDs-HA	108
3.18 De-convoluted N1s core level XPS spectra for a) GOQDs-NH ₂ , b) GOQDs-HA	108
3.19 Calibration Curve of RhodamineB	109
4.1 DLS Size Distribution of a) O/W NE 20% Oil; b) Monolayer 1%Oil _{0.01%CT} 127	
4.2 Saturation Curve Bilayer 0.5%Oil-0.05%CT-X%GOQDs-HA	127
4.3 a) DLS Size Distribution and ζ Potential Bilayer 0.5%Oil-0.05%CT-0.12%GOQDs-HA after 180 day; b) NTA Size Distribution and frame of nanoparticles detected by NTA camera (insert).	129
4.4 AFM images (left) and height profile (right) of a) Bilayer 0.5%Oil-0.05%CT-0.12%GOQDs-HA, b) Bilayer 0.5%Oil-0.05%CT-0.12%HA	130

4.5	Fluorescence spectra of a) GOQDs-HA λ_{EX} 350nm, λ_{EM} 370-650 nm; b) Bilayer 0.5%Oil-0.05%CT-0.12%GOQDs-HA λ_{EX} 350nm, λ_{EM} 370-650 nm; c) Bilayer 0.5%Oil-0.05%CT-FITC-0.12%GOQDs-HA-Rhod.B; d) Bilayer 0.5%Oil-0.05%CT-FITC-0.12%GOQDs-HA-Rhod.B	131
4.6	Multifoton Confocal images of Bilayer 0.5%Oil-0.05%CT-FITC-0.12%GOQDs-HA-Rhod.B a) FITC Fluorescence, b) Rhodamine Fluorescence; c) Bright field; d,e) overlay	132
4.7	Multifoton Confocal images of Bilayer 0.5%Oil-0.05%CT-FITC-0.12%GOQDs-HA-Rhod.B irradiated at 780 nm	132
4.8	Calibration curves from GOQDs-HA-Rhod b) Internalization of GOQDs-HA-Rhod.B in MCF10A and MDA-MB-231 cells.	133
4.9	Calibration curves of Bilayer 0.5%Oil-0.005%CT-FITC-0.12%HA in MCF10A cells and MDA-MB-231 cells b) Calibration curves of Bilayer 0.5%Oil-0.005%CT-FITC-0.12%GOQDsHA-Rhod in MCF10A cells and MDA-MB-231 cells, c) cell internalization	134
4.10	Cell viability of a) HDFs cell treated with 0.01mg/ml of GOQDs-HA-Rhod. and b) HDFs cell treated with 0.01mg/ml of Bilayer 0.5%Oil-0.005%CT-FITC-0.12%HA and 0.01 mg/ml Bilayer 0.5%Oil-0.005%CT-FITC-0.12%GOQDsHA	135
4.11	Confocal images of HDFs incubated with GOQDs-HA-Rhod, Bilayer 0.5%Oil-0.005%CT-0.12%GOQDsHA-Rhod and Bilayer 0.5%Oil-0.005%CT-FITC-0.12%HA	135

List of Tables

1.1	List of methods for controlling the size of nGO sheets.	13
2.1	Raman parameters for G, GO _{bm} and GO _{F32h}	56
2.2	C1s and O1s Atomic Concentrations and their ratio from XPS Survey Spectra	57
2.3	Binding Energy Values in C1s level from XPS analysis	57
2.4	Production methods of graphene oxide by ball milling	62
2.5	Binding Energy Values in O1s level from XPS analysis	64
3.1	Raman parameters for G, GO _{Hummer} , GOQDs-NH ₂ and GOQDs-HA	90
3.2	Binding Energy Values in C1s level from XPS analysis	91
3.3	Binding Energy Values in C1s level from XPS analysis	93
3.4	Binding Energy Values in O1s level from XPS analysis	107
3.5	Binding Energy Values in N1s level from XPS analysis	109

List of Abbreviations

2D	Two-dimensional
AFM	Atomic Force Microscopy
BE	Binding Energy
C/O	Carbon to Oxygen ratio
CPT	Camptotecin
cryo-TEM	Cryogenic Transmission Electron Microscopy
Cur	Curcumin
DLS	Dynamic Light Scattering
DOX	Doxorubicine
ECM	Extracellular Matrix
EDX	Energy Dispersive X-ray Spectroscopy
EPR	Enhanced Permeability and Retention
FITC	Fluorescein Isothiocyanate
FLIM	Fluorescence Lifetime Imaging Microscopy
FTIR	Fourier Transform Infrared Spectroscopy
G	Pristine Graphite

GIC Graphite Intercalation Compound

GO Graphene Oxide

GO_{bm} Graphene Oxide ball milled

GO_{F16h} Graphene Oxide after 16h of Fenton reaction

GO_{F32h} Graphene Oxide after 32h of Fenton reaction

GO_{F48h} Graphene Oxide after 48h of Fenton reaction

GO-NH₂ Amine-functionalized-Graphene Oxide

GOQDs Graphene Oxide Quantum Dots

GOQDs-HA Hyaluronin Acid coated Graphene Oxide Quantum Dots

GOQDs-NH₂ amino-functionalized Graphene Oxide Quantum Dots

HA Hyaluronic Acid

HDF Human Dermal Fibroblasta Cell

HOMO Highest Occupied Molecular Orbital

LbL Layer by Layer

LUMO Lowest Unoccupied Molecular Orbital

MCF10A non-transformed Epithelial Breast Cell

MDA-MB-231 Invasive Breast Adenocarcinoma Cell

MMP-2 Matrix Metalloproteinase-2

MWCO Molecular Weight Cut-off

n-GO-PEG Polyethylene glycol-functionalized nano-GO

nano-GO Nanometer scale Graphene Oxide

NC Nano-Carrier

NGS-PEG Amine-terminated six-arm branched Polyethylene glycol

NIR Near Infrared Radiation

NP Nanoparticles

O/W NE Oil/Water Nanoemulsion

PBS Phosphate Buffer Saline

PEG Polyethylene glycol

PT Photothermal Therapy

PTT Photothermal Therapy

RES Reticuloendothelial System

Rhod.B Rhodamine B isothiocyanate

ROS Reactive Oxygen species

SAED Selected Area Electron Diffraction

SEM Scanning Electron Microscopy

SiC Silicon carbide

UV Ultraviolet radiation

XRD X-ray Diffraction

Chapter 1

nano-Graphene Oxide in Cancer Therapy

Part of this Chapter has been published:

TUFANO, Immacolata; VECCHIONE, Raffaele; NETTI, Paolo Antonio. Methods to Scale Down Graphene Oxide Size and Size Implication in Anti-cancer Applications. *Frontiers in Bioengineering and Biotechnology*, 2020, 8: 1381.

1.1 State of art

In accordance with the latest report of the International Agency for Research on Cancer, the incidence of cancer is increasing worldwide[1]. Diagnosis has progressively increased from 14.8 million in 2014 to 18.1 million in 2018 (of which 23.4% in Europe) and 29.5 million are expected in 2040. Global cancer mortality has increased from 8.2 million in 2014 to 9.6 million in 2018. Patients surviving five years after diagnosis are currently 43.8 million. Despite considerable progress in the comprehension of the mechanisms involved in the origin and development of cancer, with improved diagnosis and treatment, this disease remains a major public health challenge with a considerable impact on the social and economic system, as well as on the individual[2]. Current cancer treatment requires surgical resection (for solid tumors), followed by radiation therapy, chemotherapy, or immunotherapy to kill the remaining cancer cells. The term cancer is used to define a series of critical diseases associated with replication and uncontrolled cellular spread. The abnormal proliferation of cells develops a tumor malformation characterized by a heterogeneous and complex microenvironment, which includes blood vessels, immune cells and signalling molecules. This dynamic microenvironment strongly influences the growth and evolution of the tumor and the success of therapies. The impressive progress achieved in recent decades on the etiology of cancer has not likewise translated into tangible progress in therapy[3]. It is well known that most conventional chemotherapeutic drugs show unfavorable chemical-physical and pharmacological properties such as low aqueous solubility, irritating nature, lack of stability, rapid metabolism, and nonselective drug distribution[4]. These properties cause several adverse effects, including lower therapeutic activity, dose-limiting side effects, low bioavailability of the anticancer drug at the site of action as well as high organ toxicity limiting the maximum tolerated dose and patient quality of life. Besides, resistance to many of the most active cytotoxic agents used in cancer therapy can occur in many tumors. Some tumors, initially responsive, recur, and become resistant not only to the initial therapeutic agents but also to other drugs not used for treatment[5]. Therefore, it is necessary to develop highly efficient therapeutic

systems able to overcome biological barriers, selectively distinguish cancerous tissues from healthy ones and react "intelligently" to the heterogeneous and complex tumor microenvironment for the on-demand release of therapeutic agents in the optimal dosage range[6]. As early as 2006, the National Cancer Institute recognized nanotechnology as the science that can effectively change the basis for the diagnosis, treatment, and prevention of cancer, allowing the study and treatment of this disease at a molecular scale, in real-time and during the early stages of the process[7]. Although particles between 10 and 100 nm are known since ancient times as components of pigments and dyes, the concept of nanotechnology as a potential manipulation of matter on the atomic scale is quite recent[8]. The application of nanotechnology to disease treatment, diagnosis, monitoring, and control of biological systems is referred to as "Nanomedicine". The success of nanotechnology in the healthcare field is due to the possibility of working at the same scale as many biological processes, cellular mechanisms, and organic molecules[9]. The traditional application of nanotechnology in cancer therapy is to improve pharmacokinetics and reduce the side effects of chemotherapy through nanocarriers that target selectively and deliver anti-cancer drugs to tumor tissues. The nanocarriers used for drug delivery are manufactured from both soft (organic and polymeric) and hard (inorganic) materials assembled in different architectures such as polymeric micelles, nanoparticles (NP), liposomes, and dendrimers, which share the dimensional characteristic of the nanometric scale. The active cargo can be easily encapsulated or covalently bonded with the nanocarriers exploiting the chemical-physical properties of the materials that compose them[10]. The nanostructured transport systems are originally designed to increase cellular uptake and accumulation due to their nanometric size. One of the unique features of almost all solid tumors is "leaky" tumor vascularization and compromised lymphatic drainage. As previously described, a growing tumor mass generates a network of abnormal blood vessels (angiogenesis) for increasing oxygen and nutrients supply. This feature, combined with the poor lymphatic clearance typical of tumor masses, allows particles between 10 and 100 nm in size to passively penetrate through the pores of blood vessel walls and accumulate preferentially in tumor sites rather than in other healthy tissues. This effect,

known as enhanced permeability and retention (EPR), has shown promising results compared to standard therapies in terms of reduced toxicity in healthy tissues and increased drug concentration at the target site. Over the past 20 years, a variety of nano-carriers such as liposomes, micelles, albumin NP and polymeric conjugates have been approved for the treatment of various tumors[11]. However, the nanocarrier exploiting the EPR effect must necessarily have a long circulation time in the blood to arrive at the target area. One of the approaches commonly used to increase the efficiency of drug transport to cells and cancerous tissues is to modify the surface of nanocarriers with water-soluble polymers such as polyethylene glycol (PEG). Because of their hydrophilic nature, PEG chains create a hydrated cloud that protects the surface from aggregation, opsonization, and phagocytosis, increasing blood circulation time[12]. Doxil[®], PEG-coated liposomal doxorubicin was approved by the US FDA in 1995 and is used for the treatment of breast cancer through the passive accumulation. The passive targeting of drug carrier systems through the EPR effect has some limitations. First, the EPR effect is highly biologically dependent on the degree of vascularization and angiogenesis of the tumor. Also, the high interstitial pressure in the central area of the tumor not only inhibits the delivery of the drug by convection but also compresses new blood vessels. As a result, blood is led away from the center of the tumor to the periphery[13]. An ideal nanocarrier should simultaneously show a high accumulation in the tumor and cellular internalization after achieving tumor tissue. However, the EPR effect does not enhance the uptake of nanoparticles into the cells. For this reason, next-generation therapeutic nanoparticles have an active targeting mechanism. Active targeting is usually performed by binding a variety of specific ligands to the surface of the nanocarrier that can recognize specific surface molecules that are overexpressed by tumor cells but not present in normal cells. Through this mechanism, it is possible to increase the affinity of the nanocarrier for the surface of cancer cells or tumor tissue and thus significantly increase the amount of drug delivered to the target cell compared to the free drug or passive targeting nanosystems[14]. The stochastic nature of ligand-receptor interactions in active targeting and the lack of cell, tissue, and organ specificity of the laws governing the spread of the nanocarrier within the body in passive targeting, result

in these processes being poorly applied in the clinic and suggest the need for more efficient delivery strategies[15]. One way to improve effectiveness and reduce side effects is to consider responsive stimuli delivery systems that provide tailor-made release profiles with excellent spatial and temporal control. Compared to traditional nanocarriers, responsive stimuli delivery systems are designed to improve solubility, bioavailability and to prolong the blood circulation time, besides, they can be chemically optimized to achieve selective drug release at desired action sites, which can enable them to bypass physiological or pathological barriers and achieve higher therapeutic efficacy[16]. Commonly this approach has been realized with biocompatible materials properly engineered to undergo a specific protonation, a hydrolytic rupture, a conformational change in response to a specific stimulus. The stimuli investigated include endogenous stimuli (e.g. reactive oxygen species (ROS), redox, pH, and enzymes) and exogenous stimuli (e.g. light, temperature, magnetic field, and ultrasound)[15]. Another aspect to consider in designing an effective therapy plan is the real-time monitoring of the therapy. With conventional treatments, diagnosis, therapy, and evaluation of the effect of the therapy are independent processes. This prolongs healing times and increases the suffering of cancer patients, especially when considering that contrast agents used in classical imaging techniques are not free of side effects. To overcome these obstacles, a promising clinical application consists of systems able to combine drug and diagnostic agents on the same nanocarriers to detect disease status and also provide therapeutic agents to target sites with real-time monitoring of pharmacokinetics, distribution and accumulation of drugs in tumors, leading to effective tumor inhibition as soon as possible[17]. Nano-systems that can integrate imaging and therapy are referred to as nano-theranostics. If the materials selected for nano-theranostic systems are responsive to electromagnetic, sound, or thermal fields, it is also possible to combine chemotherapy and imaging with other treatments. One of the most studied topics in recent years is the combination of chemotherapy with photothermal therapy (PTT) since photothermal therapy is a minimally invasive and potentially effective treatment. PTT is a physical-chemical therapy for the treatment of cancer that employs optical radiation in the near infrared radiation (NIR) wavelength range (700-900

nm). When a laser is focused on a tissue, the photons are absorbed by the inter-cellular and intracellular areas and the energy of the photons is converted into heat. As a result, the temperature of the tissues increases, leading to the death of cells and tissues[18]. The local increase in temperature due to radiation not only causes the ablation of tumors but improves the permeability of the cell membrane, making the accumulation of nanoparticles in tumor cells more effective and hinders the repair of DNA damage caused by anticancer drugs in tumor cells, increasing the effects of chemotherapy agents[19]. In addition, the NIR radiation used, also known as "optical window" or "therapeutic window", is the wavelength range that has the greatest depth of penetration into tissues. The most widely accepted NIR photothermal agents include fluorescent dyes, two-dimensional inorganic materials (e.g. carbon nanotubes, graphene oxide, and gold materials), and polydopamine[20]. Ultra-thin two-dimensional (2D) nanomaterials are a large class of nanomaterials with sheet-like structures, lateral dimensions greater than 100 nm, and thickness less than 5 nm[21]. This class of materials is in continuous evolution and includes nanomaterials of different chemical compositions and crystalline structures. Generally speaking, ultra-thin 2D nanomaterials are distinguished as layered 2D nanomaterials and non-layered 2D nanomaterials. In layered nanomaterials, the atoms in each layer are connected by strong chemical bonds, while the layers stack together to form bulk crystals through weak Van der Waals interactions. In contrast, non-layered nanomaterials crystallize in three dimensions through atomic or chemical bonds to form bulk crystals.[21] The study of 2D nanomaterials was first reported in 2004 when Novoselov et al. succeeded in exfoliating graphene from graphite[22], and since then research on ultra-thin 2D nanomaterials has grown exponentially in the fields of condensed matter physics, materials science, chemistry, and nanotechnology. The unique characteristics of 2D nanomaterials have raised important and exciting questions about their interactions with biological systems. Being the thinnest materials, 2D nanomaterials have the highest specific surface areas among all known materials, which means that they can efficiently load and deliver therapeutic agents. Also, the planar nanostructure gives these nanomaterials special physicochemical properties (e.g. light, ultrasonic and magnetic responses) and biological behav-

iors such as endocytosis, biodistribution, biodegradation, and excretory pathways, which lead to their use in various biomedical applications[23,24]. Among 2D nanomaterials, graphene and its derivatives have attracted enormous attention in cancer diagnosis and therapy because they combine, in a unique material, extremely small size, NIR absorption, delocalized electrons, extremely high surface area, and versatile surface functionality. Graphene is an allotropic form of carbon defined as a single layer (monolayer) of carbon atoms sp^2 -bonded, which are densely packed in a hexagonal honeycomb lattice[25]. Since its recent discovery, this material has attracted enormous attention for its unique and, sometimes surprising, properties. Graphene is the thinnest and lightest compound known, it has a maximum tensile strength that is hundreds of times higher than steel; the electronic mobility exhibited by graphene even at room temperature, makes it an excellent heat conductor and also the best conductor of electricity and it has a great ability of optical transmittance[26]. In the original study of Novoselov, single or a few layers of pristine graphene were obtained with the "scotch tape" method of mechanical exfoliation of the graphite using adhesive tape. However, this method is not scalable, and therefore other approaches have been proposed, including chemical vapour deposition[27], arc discharge[28], and epitaxial growth on Silicon carbide (SiC)[29].

To date, the most widely used method when large scale graphene production is required is the wet chemical exfoliation of graphite[30]. This method involves the liquid-phase exfoliation of graphite which, as it is well known, is composed of layers of graphene assembled parallel to each other and linked together by Van der Waals interactions. To break the interactions that hold together the graphene layers in the graphite, intense oxidation of the aromatic system is necessary. The oxidation generates an intermediate, known as graphite oxide with a high density of oxygenated functional groups and which is then transformed into reduced graphene oxide by chemical or electrochemical reduction. Graphite oxide, obtained from the oxidation of graphite, can be exfoliated in solution to form graphene oxide (monolayer), or partially exfoliated to form few-layers graphene oxide[31]. Graphene Oxide (GO), initially considered as an intermediate of one of the graphene production processes, has become a material that can be considered both for fundamental research and

for its potential applications. The simple, scalable, and economical production process, coupled with the peculiar chemical-physical characteristics, make GO one of the most promising nanomaterials in several fields and, notably, in the cross-section of nanotechnology and biotechnology. GO is a single or a few-layer material with a high oxygen content, typically characterized by atomic carbon to oxygen ratios (C / O) below 3.0 and generally closer to 2.0. Unlike the perfectly ordered crystalline structure of graphene, graphene oxide has a two-dimensional structure in which crystalline regions and regions with amorphous defects of sp^3 hybridized carbons and functional groups containing oxygen, coexist[32]. (Fig.1.1) The different oxygenated functions located on one or both sides of the GO sheet, make this material soluble and processable in water and many organic solvents and make the surface of GO very versatile for functionalization or chemical changes to finely modify its properties or to increase biocompatibility[33]. The aromatic structure instead allows noncovalent inter-

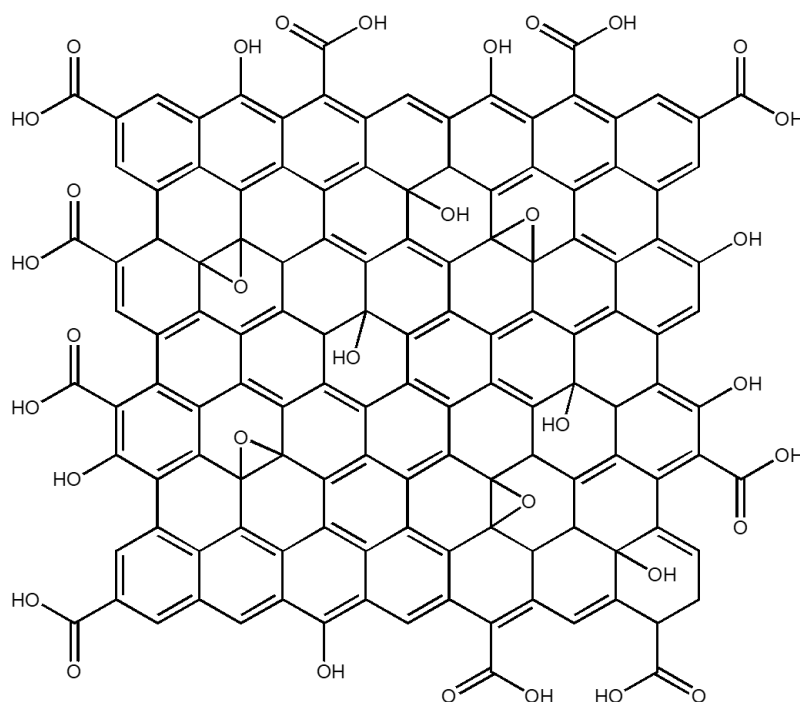


Figure 1.1: Chemical structure of Graphene Oxide based on Lerf-Klinowski model

action with π conjugated molecules and confers to the graphene oxide the abil-

ity to absorb light in the range of NIR (700-900 nm). This property is particularly interesting when considering cellular hyperthermia in the treatment of tumors as a minimally invasive alternative to surgery[34]. Furthermore, functionalized graphene oxide and nanocomposites based on graphene oxide have interesting optical and magnetic properties and can be employed as contrast agents for various biological imaging modalities including fluorescence imaging, photoacoustic imaging, and magnetic resonance imaging[35]. The era of graphene oxide in cancer therapy started in 2008 with pioneering Dai's group study. They demonstrated that polyethylene glycol-functionalized nanographene oxide (n-GO-PEG) was able to efficiently complex water-insoluble aromatic drug molecules via non-covalent Van der Waals interactions. This new nanocarrier showed in vitro cellular uptake and killing potential for some cancer cell lines[36]. Subsequently, graphene oxide was conjugated with biopolymers, biomolecules, inorganic nanoparticles, metals, and metal oxides to create intelligent nanoplat-forms able to respond at every stage of the cancer treatment process, from targeting to imaging and therapy[33] (Fig. 1.2). Although it seems that graphene

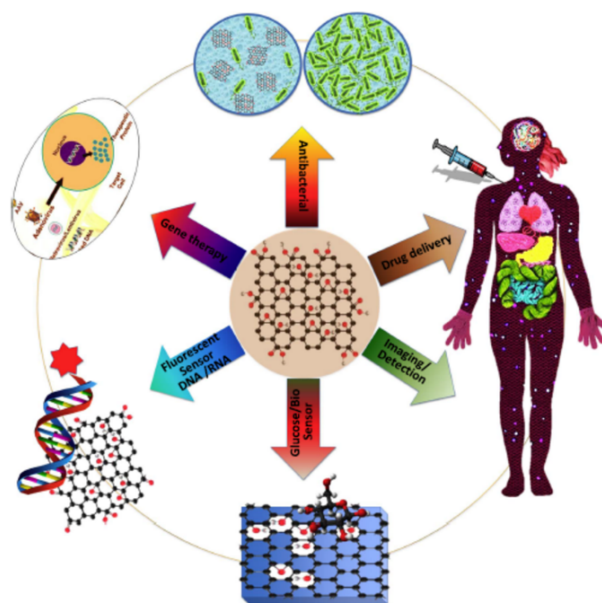


Figure 1.2: Bio-applications of Graphene Oxide in Cancer Therapy. Reproduced from Reference 33

oxide applications in the field of cancer therapy are limited only by the creativ-

ity of scientists, to date, no biomedical nanomaterial based on graphene oxide has been successfully translated into clinical use in patients. This is partly due to the relatively recent application of GO in the biomedical field, but, above all, it depends on the inhomogeneity of the material. GO is a heterogeneous material consisting of sheets with different sizes, number of layers, degree of oxidation, and chemical surface. Moreover, most of the synthetic methods used for the production of graphene oxide, although simple, low cost and scalable, lack reproducibility as they require a long and tedious work-up that can heavily affect the chemical-physical characteristics of the material obtained. Numerous workup procedures are reported in the literature, the common denominator of all being an extensive dilution of acids[37,38]. During the process huge quantities of water are used to neutralize the acids and to remove the salts formed by the oxidation mixture. The waste water obtained therefore contains various manganese, potassium and sulphur ions and their treatment and subsequent disposal represent a bottleneck in the marketing of GOs on a large scale. Another issue that deserves attention in the large-scale GO production and marketing process concerns the large amount of sulphuric acid required for the oxidation of graphite. Generally, more than 15 mL of concentrated sulphuric acid is required for each gram of graphite[39]. Such a large amount of acid is needed to stabilize the Mn_2O_7 intermediate that is formed from the reaction of H_2SO_4 and $KMnO_4$, and that if it does not react further with other acid it could cause explosions[40]. This represents a major limit both for the risks associated with the use of large quantities of concentrated acids and for the costs relating to disposal. Another problem to be addressed in the design of graphene oxide-based theranostic nanoplatfoms is to obtain a starting material with suitable and homogeneous dimensions. Graphene oxide has size-dependent properties. First, the colloidal stability of graphene oxide sheets in aqueous solution and biological media is size-dependent. Nanometer-scale GO (nano-GO) sheets form more stable colloidal dispersions due to the high density of charge resulting from the ionized -COOH groups at their edges. It is well known that the chemical-physical properties of materials, particularly their size, may regulate the cellular response to them. The size of the material impacts on cellular uptake, renal clearance, transport to blood or brain barriers, and even partly

the biological or toxicological effects induced by the material[41]. Graphene materials have sizes ranging from 10 nm, the size of some proteins, to more than 20 μm , larger than many cells. Large sheets can therefore adhere to the plasma membrane and spread into the cells, while small sheets can be internalized via one or more receptor-mediated endocytosis mechanisms[42]. In nanomedicine applications, therefore, the synthesis of highly pure graphene oxide with precise dimensions and narrow size distribution is crucial. Unfortunately, graphene oxide sheets are often prepared by chemical exfoliation of graphite and the lateral dimensions of the GO prepared by this convenient method are very polydisperse in the range from tens of nanometers to a hundreds of micrometres. Therefore, it is important to design methods during or post-synthesis to satisfy the above requirements. For this purpose, a variety of methods have been developed which can generally be distinguished in direct controllable synthesis and post synthesis separation. The direct controllable synthesis approach involves intervention during the chemical oxidation process by using different precursors, or by tuning the reaction parameters (amount of oxidants, time and temperature) or by employing physical promoters which mechanically break pristine graphite or graphene oxide sheets obtained. The post synthesis separation involves instead the graphene oxide bulk fractionation through centrifugation or selective precipitation in organic solvents, or different pH aqueous solution. The main methods for controlling the size of nano-GO sheets are summarized in Table 1.1.

1.1.1 Synthetic Approaches

Graphite, the precursor of GO, has a highly ordered crystalline structure composed of layers of sp^2 hybridized carbon atoms connected within each layer by covalent and metallic bonds and by weak Van der Waals interactions between the layers. As a consequence, graphite is anisotropic, being a good electrical and thermal conductor in-plane and a weak electrical and thermal conductor perpendicular to the plane. The carbon layers in graphite are known as graphene layers[60]. Anisotropy allows graphite to undergo chemical reactions

	General Method	Specific strategy	Feature size	Ref.
Controllable Synthesis	Different Precursors	Graphite Nanofibers: very small graphite plates (diameter about 130 nm and length up to 5 mm) stacked in particular conformations	100-50 nm	[43]
		Arc-discharge Material: carbon material highly flexible and defective obtained by electrical breakdown	20-40 nm	[44]
		Aphanatic Graphite: kind of graphite with disorder structure obtained by thermal decomposition of deep metamorphic	4.5 nm	[45]
	Reaction Parameters	Time and Oxidant Amounts: increase in the amount of oxidizing agent and timescale of oxidation in the same batch	50-20 nm	[46,47]
		More Oxidation Cycles: for each cycle the obtained product was isolated, purified and re-oxidized	10-5 nm	[48]
	Physical Promoters	Ultra Sonication: application of sound energy in a water bath or through probes to break GO sheets in low temperature conditions	100-500 nm	[49,50]
		Ball Milling: graphite with or without solvents or oxidants was mechanochemical oxidized in a rotating cylindrical jar filled with loose grinding balls.	100mm-50 nm	[51,52]

	General Method	Specific strategy	Feature size	Ref.
Post-synthesis Separations	Centrifugation	Differential Centrifugation Method: GO sheets to be separated was divided in several fractions according to their size by varying the centrifugal force applied	250-900 nm	[53,54]
		Density Gradient Centrifugation: GO to be separated was placed on the surface of a vertical column of liquid with increased density from top to bottom and centrifuged. The particles migrated through the solvent gradient and settled where their buoyancy density equaled that of the gradient	40-500 nm	[55,57]
	Flocculation by Solvent	Protonation in Organic Solvents: large GO sheets precipitated selectively in organic solvents by protonation of carboxyl groups on the edges	500-100 μm	[58]
		pH Assisted Precipitation: nano-GO sheets were recovered from the strongly acidic precipitate obtained from the work-up of the classic oxidation reaction by increasing pH value to 1.7 with 1M NaOH	90 nm	[59]

Table 1.1: List of methods for controlling the size of nGO sheets.

called intercalation reactions in which the reagents can penetrate between the graphene layers of graphite to form graphite intercalation compounds (GIC_s) that are electrically more conductive than graphite and then develop into other compounds like graphite oxide. Because of the considerable thermodynamic stability of graphite, the conversion of graphite to graphite oxide requires very drastic reaction conditions involving concentrated acidic media and strong oxidizing agents. The recipes for graphite oxidation still used today, although with some modifications, are almost all based on three main methods: Brodie's method of 1855[61], Staudenmaier's method of 1989[62], and the Hummer's method of 1958[63]. Brodie's method consists of heating graphite at 60°C for 3-4 days in a mixture of potassium chlorate, an oxidizing agent, in fuming nitric acid. The oxidation step must be repeated for 4-7 cycles and before each step, the partially oxidized product must be isolated, washed, and dried. Staudenmaier works on Brodie's method to speed up the reaction and increase yield. He discovered that by replacing fuming nitric acid with a mixture of concentrated sulphuric acid: fuming nitric acid 3:1 and slowly adding potassium chlorate in multiple portions, the reaction continues in a single vessel. However, this reaction requires 4 days to complete. More than 100 years after Brodie's discovery, Hummers and Offemann proposed a new, faster, and safer method for graphite oxidation. This method involves three reaction steps at controlled temperatures. At low temperature (below 5°C) it occurs the slow addition of an excess of potassium permanganate (three eq.) to a suspension of graphite and sodium nitrate in concentrated sulphuric acid. The reaction continues for 30 min at mid-temperature (~ 35 °C) and the mixture becomes more homogenous. After this time, warm water is added to the mixture causing heat generation, the temperature reaches 98°C and the reaction is maintained at this temperature for 15 min by an exothermal heat, then the reaction is quenched with a hydrogen peroxide solution to reduce the residual permanganate and manganese dioxide to soluble colourless manganese sulphate. The formation of a bright yellow pasty mixture is the evidence of the successful conversion of pristine graphite in graphene oxide. The oxidation products obtained with the three methods differ slightly in chemical composition and degree of oxidation. In general, graphene oxide obtained with the Hummer method has a higher degree of ox-

idation as revealed by the lower C/O (GO-Hummers 1.12 < GO-Staudenmaier 1.77 < GO-Brodie 2.52) and by the higher spatial distance between the layers observed in the X-ray diffraction (XRD) patterns (GO-Hummers 0.8133 nm > GO-Staudenmaier 0.7226 nm > GO-Brodie 0.7084 nm)[64]. Although the methods using KClO_3 and HNO_3 suffer from long reaction times and the evolution of acid fog resulting from fuming nitric acid, and the highly explosive ClO_2 gas generated when chlorate is mixed with strong acids, they remain the most powerful and well-known oxidative methods for producing GO on a preparative scale[65]. Instead, the fastest, easiest and safest Hummer method is the most widely used approach to obtain graphite oxide on a large scale[63]. Because of its satisfactory characteristics, this method has been widely used to investigate the mechanism of graphene oxide formation, as well as widely revisited and modified. One of the most popular modifications of the Hummers method was proposed by Marcano et al. in 2010[66]. The Marcano method, known as the improved Hummers method, involves using a quantity of oxidizing agent (KMnO_4) twice as much as the Hummers method, and the replacement of sodium nitrate with phosphoric acid (H_3PO_4). The use of a higher amount of oxidizer results in a product with a higher degree of oxidation, the use of phosphoric acid, instead, allows to obtain a product with a more regular structure and with a greater number of isolated aromatic rings preserved. Also, the elimination of nitrate from the synthetic procedure avoids the evolution of NO_2 and N_2O_4 toxic gases. Chen et al. compared GO samples obtained from the same graphite source with the Hummer method without or with the use of NaNO_3 , demonstrating that the exclusion of sodium nitrate from the reaction formula does not affect the chemical-physical properties (dispersibility, chemical structures, thicknesses, and lateral dimensions) of the product and the overall yield[67]. The authors provide a convenient method for the purification of wastewater collected from the graphene oxide purification process. The pollutant Mn^{2+} ions from wastewater can be easily converted into a precipitate of Mn_3O_4 by adding KOH . The post-treatment of waste from nanomaterial production processes is a low considered issue, but essential for commercialization. Another version of the modified Hummers method without sodium nitrate consists of pre-oxidization of graphite flakes with a mixture of

sulphuric acid, phosphorus pentoxide P_2O_5 , and persulfate ions ($S_2O_8^{2-}$) for 5 h at $80^\circ C$ [68]. The oxidative pre-treatment increases the distance between the graphite layers in the graphite and renders it more available for the subsequent oxidation process. This two-step method results in GO samples with higher oxygen content. The increased interest in the properties of this material encouraged researchers to look for more rapid, cost-effective, green (free of toxic gases and polluting heavy metals) and safe (no risk of explosion) synthesis methods. In this scenario, oxidizers other than potassium permanganate were considered. For example, benzoyl peroxide (BPO) heated to $110^\circ C$ in an open vessel with graphite powder oxidizes the pristine graphite in 10 min under acid and metal-free conditions[69]. Although this method is highly efficient, the high instability of benzoyl peroxide and the structural damage in the oxidation product due to the high operating temperature render this procedure not applicable on a large scale. Peng et al. in 2015 proposed a completely new method for graphene oxide synthesis using potassium ferrate (K_2FeO_4) as oxidant[70]. K_2FeO_4 has a higher oxidation efficiency than $KMnO_4$ in an acid environment, it can be handled without risk of explosion at temperatures as high as $100^\circ C$ and it does not generate toxic or polluting by-products. In this approach, highly water-soluble graphene oxide is obtained after only 1 h stirring of a mixture of concentrated sulphuric acid, K_2FeO_4 , and graphite flake at room temperature. The graphene oxide sheets prepared with K_2FeO_4 have a single layer morphology (~ 0.9 nm thickness as measured by Atomic Force Microscopy (AFM)) with an average numerical width of $\sim 10 \mu m$ (from Scanning Electron Microscopy (SEM) images) and a degree of oxidation nearly equal to that of the GO produced using $KMnO_4$. The authors claim that the high oxidation and exfoliation state is due to the synergy between FeO_4^{2-} ions and atomic oxygen [O] produced in situ. Since the reaction process is extremely simple and requires no energy transfer (neither heating nor cooling), it is straightforward to scale up. Besides, the work-up of this method allows to recover the sulphuric acid used for centrifugation and to reuse it for at least another 10 times without affecting the reaction time and the quality of the product. This eco-friendly, safe, highly efficient, scalable, and low-cost approach is unfortunately difficult to reproduce because the strong oxidizing power of ferrate (VI) is directly related

to its instability, particularly in acidic environments[71]. In high-acid aqueous solutions, potassium ferrate (VI) decomposes in a few seconds via an autocatalytic process, which limits its applications in chemical synthesis. Moreover, it is not widely commercially available and its synthesis involves the use of chlorine gas which is highly toxic. Among the modern approaches, particular attention is focused on the production of graphene oxide by electrochemical exfoliation which is simple, environmentally friendly, and substrate-free. Typically, graphene oxide flakes are generated taking advantage of the electrical conductivity of graphite (e.g., foil, rod or flakes, flexible paper) in aqueous electrolytes (H_2SO_4 or H_3PO_4). A typical apparatus for electrochemical exfoliation of graphite consists of an electrochemical cell with two electrodes of graphite in an aqueous solution of electrolytes[72]. At first, a static potential of 1 V is applied to the two electrodes to wet the electrode surface and facilitate the accumulation of charges around the anode. The applied potential is then increased to +7 V and maintained for 5-10 min. At this potential value, the anions in the electrolytic solution are guided to intercalate between the galleries of the graphene layers. By alternating the potential between +7 and -7 V it is possible to obtain exfoliation of both electrodes. After only a few minutes of electrolysis, a change in color of the aqueous electrolyte from transparent to dark is observed, which indicates the formation of GO. Similar to chemical oxidation, various sources of graphite or metals such as platinum and titanium can be used as electrodes and a variety of electrolytes including inorganic aqueous solutions, surfactants, molten salts, and ionic liquids. The electrochemical exfoliation of graphite is a tunable process because the chemical and chemical-physical properties of the oxidation product (morphology and degree of oxidation) can be easily adapted by adjusting the experimental set-up (type and geometry of the electrodes, solution, electrolytic, applied voltage, time and temperature).

1.1.2 Mechanism of graphene oxide formation and breakage

Knowing the formation mechanism of GO is a key step in the development of new materials with the desired properties. However, despite the remark-

able progress in understanding the chemistry and structure of GO, the mechanism of its formation received little attention from the scientific community. The majority of the reported studies are theoretical and focus on the introduction of oxygen atoms into the graphene lattice with the formation of C-O bonds[73,74]. In an elegant work of 2014, Dimiev and Tour have illuminated the steps that occur during the oxidation of graphite with potassium permanganate into concentrated sulphuric acid both within the solid graphite (between the graphene layers) and at the solid/liquid interface[75]. Starting from the assumption that the characterization of the final graphite oxide obtained with the Hummer method, washed with water and dried is not very informative in mechanistic terms, the intermediate products that are formed in the various steps of addition of permanganate have been isolated. The characterization, through optical microscopy and Raman spectrometry, of the obtained intermediates permitted to identify three distinct independent steps in the chemical oxidation of graphite with strong oxidants in concentrated mineral acids. The first step is the classic graphite intercalation reaction in which H_2SO_4 molecules and HSO_4^- ions intercalate between graphite galleries without creating an orderly structure. The intercalation compound is formed after a few minutes that the graphite is exposed to the acid medium and imparts an intense blue colour to the graphite. The intercalation is a necessary step for successful oxidation because it increases the distance between the graphene layers in the graphite making the tunnels between the layers accessible to the oxidizing agent. The second step is the conversion of GIC into the oxidized form of graphite called pristine graphene oxide. In this step, the oxidizing agent molecules are inserted into the pre-occupied graphite galleries. Optical microscopies of the graphite flakes isolated at this stage clearly show that the conversion from intercalation compound (blue colour at the center of the flake) to pristine graphene oxide (pearly white colour at the edges) propagates from the edges of the flakes to the center. (Fig. 1.3) Theoretically, in the conversion from the intercalation product to the oxidation product, the oxidant molecules should replace or intercalate with the acid molecules present in the graphite interlayers. The experimental data show, instead, that the speed of the oxidation reaction is greater than the rate of diffusion, in other words, before the

oxidizing agent diffuses between the graphite layers, it reacts rapidly with the nearby carbon atoms. So the pristine graphite oxide formation is the step that determines the rate of the entire graphene oxide formation process. The fi-

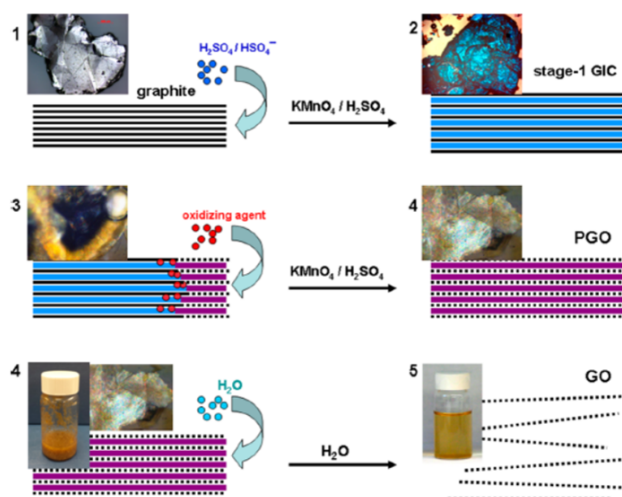


Figure 1.3: Stage of conversion of bulk graphite in graphene oxide solution with corresponding micrographic images. Reproduced from ref. 75

nal step is the conversion of pristine graphite oxide to graphene oxide by reaction with water during quenching and washing procedures. At this stage the graphite oxide, if sufficiently oxidized, delaminates spontaneously into single atomic layer sheets. To obtain exfoliation hydrogen bonds and electrostatic interactions between water and graphene oxide must overcome the electrostatic interaction between graphene layers and intercalants (within each layer) and water molecules must be able to hydrolyze covalent sulphates that cross-link neighbouring layers. Very recently the same authors have corrected the mechanism by reconsidering the role of water in the formation of graphene oxide. To investigate the nature of the effective oxidizing species attacking graphite layers, they found that the rate of oxidation reaction increases by a factor of 12 when the reaction is carried out in slightly diluted sulphuric acid (92% - 88%) rather than in commercially available H_2SO_4 at a concentration of 95% - 98% [76]. This observation opens an important perspective on the reaction mechanism. Following the same procedure of isolation and characterization of intermediates, the authors conclude that the species attacking the carbon

atoms in the Hummers method are water molecules and not oxidant molecules. However, manganese species (VII) cannot be completely omitted from the reaction equation because they are consumed during the reaction and because once the first equivalent of permanganate is consumed, the reaction does not go on unless another one is added. The authors claim that the reaction occurs directly between the H_2SO_4 graphite intercalation compound and water according to a mechanism very similar to the hydration of aromatic hydrocarbons in acid media where water nucleophilically attacks the carbon atoms of graphene and the Mn (VII) species accept the electrons that are released, reducing to Mn (IV). Since the formation of graphene oxide is a process controlled by the rate at which oxidizing molecules or water molecules diffuse between the graphite layers, smaller graphite flakes oxidize faster than larger ones. And since no any graphite flake is equal to another, it is not surprising that graphene oxide is a material with a wide size distribution ranging from a few nanometers to hundreds of micrometers. However, it is possible to select graphene oxide sheets of nanometric size through post-synthesis methods or reduce the sheet size by adjusting the parameters of the chemical reaction or by using mechanical promoters. The structural characteristics of the obtained nano-GO and the breaking mechanism are very dependent on the method used for breaking. In general, when acting on the chemical reaction (by varying the amount of oxidants, the time or temperature of the reaction) graphene oxide nanosheets with a higher oxygen content are obtained[47], while when using physical methods to promote breakage (ultrasonication) nanosheet with a higher C / O ratio is obtained[77]. These experimental observations reflect a different breaking mechanism. As it is known, crystalline and amorphous regions coexist in the structure of graphene oxide. The breakage of graphene oxide into sheets with lower lateral size occurs through the formation and propagation of cracks over defects zones, in particular regions with the sp^3 bond like -C-OH and O-C-O. When graphene oxide is fragmented by increasing the amount of oxidants or prolonging the reaction time, the reaction mechanism is similar to that of oxidizing olefins with KMnO_4 in aqueous solution and has been demonstrated experimentally following the gradual opening of carbon nanotubes as the exposure time of the system in oxidizing medium increases[78]. This mechanism

involves the formation of a manganese ester in the rate-determining stage of the reaction. The ester further oxidizes to dione in the dehydrating medium and distorts the nearby double bonds making them more available to the next permanganate attack. The ketones can be further converted, through their O-protonated forms, to the carboxylic acids that will line the edges of the nanosheet (Fig. 1.4). When the breaking of GO occurs by applying an external energy

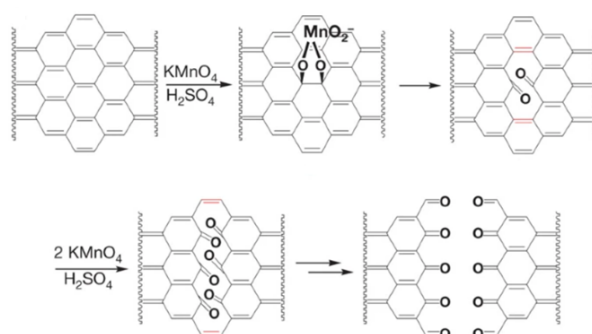


Figure 1.4: Mechanism of the breakage by variation of reaction parameters. Reproduced from ref. 78

source, the mechanism involves the breaking of chemical bonds. The breaking starts from defects zones, in particular regions with the sp^3 bonds like -C-OH and O-C-O, as previously said. After propagation of cracks, smaller sheets are obtained (Fig. 1.5). If the process continues, a smaller but also more hydrophobic material will form. The use of ultrasound generates a local increase in temperature and pressure that promotes the decomposition of water molecules in the medium into hydroxyl radicals. $[\cdot\text{OH}]$ radicals have the potential to reduce carboxylic and carbonyl groups by restructuring the aromatic carbon network and forming a more hydrophobic material(77). This mechanism is defined as confined hot spot atomic reduction of GO.

1.1.3 Nano Graphene oxide in cancer therapy

The intrinsic properties of nano-GO make this material very interesting in the field of biomedicine. The oxygen atoms chemically bonded to the carbon lattice by treatment with strong oxidizing agents in an acidic environment are

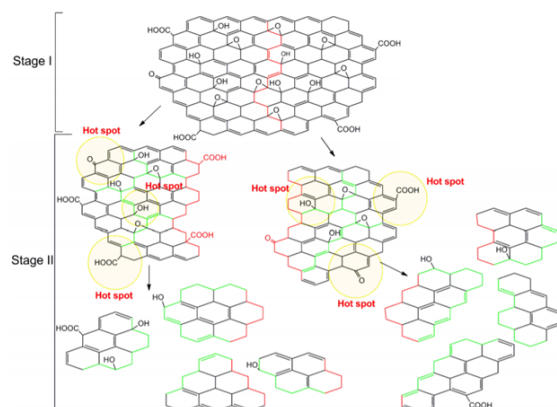


Figure 1.5: Mechanism of the breakage by ultrasonication. Reproduced from ref. 7

defects introduced in the ideal graphite plane, but they provide the GO with unique properties such as hydrophilicity, i.e., the ability to dissolve and to form stable colloidal solutions in water and some low molecular weight alcohols. The oxygenated groups present on the surface of the GO and the nanometric dimensions are not enough to balance the screening of the electrostatic charges when the nano-GO is in biological media, consequently, the nano-GO tends to aggregate in physiological solutions with salts and proteins[79]. The surface functionalization of GO increases solubility under physiological conditions and opens the scenario to a wide range of biomedical applications. In general, the chemical functionalization of the GO may be of covalent or non-covalent type. Covalent functionalization involves the conversion of the functional groups present on the GO and/or the chemical bond between the functional groups and external species such as small molecules, polymers, and inorganic particles. Non-covalent functionalization, on the other hand, exploits the large, atomically flat surface of GO as an anchor for other chemical species through secondary interactions such as Van der Waals forces and π - π interactions[80]. GO can be used as an efficient nanocarrier for the loading and transport of water-insoluble aromatic molecules using non-covalent interactions. Approximately 50% of GO carbon atoms are sp^2 carbons and therefore can interact with conjugated π molecules. After the pioneering study by Dai and collaborators[81] many other research groups have confirmed the excellent

drug loading ability of the nano-GO. In this context Zhang et al., first demonstrated the ability of nano-GO to load simultaneously two drugs [doxorubicin (DOX) and camptotecin (CPT)] with synergistic action and a loading efficacy comparable to the loading of a single drug[82]. This approach is very advantageous because it allows the reduction of multidrug resistance to anticancer drugs, the phenomenon that occurs when cancer cells develop resistance to anticancer drugs with different structures and mechanisms of action[83]. According to widely agreed Lerf and Klinowski's model, GO sheets have chemically reactive oxygenated functions, such as carboxylic acid groups at the edges and epoxy and hydroxylic groups on the basal planes. These oxygenated functionalities provide useful sites for the covalent functionalization of the GO. Covalent functionalization includes a variety of reactions as esterification, amidation, click chemistry, nitrene chemistry, and radical addition[84] and is widely used for drug loading, coating the nano-GO with biocompatible polymers, or bonding targeting motives. Although there are examples of functionalization of the hydroxyl and epoxy groups located in the basal plane of the GO[85,86] the chemistry of GO is dominated by the chemistry of the carboxylic and carbonyl functional groups located at the edges[87,88]. Most approaches exploit the protocols of carboxylic acid conversion reactions into esters or amides. The introduction of substituted amines is one of the most common covalent functionalization methods and the final products are designed for various applications. An example of the use of GO functionalized amine (GO-NH₂) for biological applications is provided by the work of Singh et al.[89] They synthesized GO-NH₂ by activation of GO carboxylic acid groups with thionyl chloride in dimethylformamide and subsequent reaction with sodium azide and demonstrated that it was a safer alternative for biomedical applications, compared to oxygenated derivatives. It is known that GO, when administered intravenously in mice, has the potential to cause a strong aggregation response in platelets on a scale comparable to that caused by thrombin, one of the most powerful physiological platelet agonists, and triggers extensive pulmonary thromboembolism, consistent with the prothrombotic nature of this material[90]. In vivo and in vitro tests showed that GO-NH₂, being positively charged, was more biocompatible than GO, had no stimulating action toward platelets and did not in-

duce pulmonary thromboembolism in mice. As discussed extensively earlier, one way to increase nanocarrier accumulation at the tumor site is to bond ligand at the nanocarrier surface to selectively recognize specific molecules that are over-expressed by tumor cells and tissues, but are not present in healthy cells and tissues. Wu et al. used the same chemical route to functionalize a nano-GO with hyaluronic acid (HA)[91], a naturally occurring polysaccharide with excellent physicochemical properties, such as biodegradability, biocompatibility, and non-immunogenicity. HA is also recognized as binding to various invasive cancer cells that over-express CD44, a type I transmembrane glycoprotein. The obtained nano-GO-HA system showed a high loading capacity of the anti-tumor drug DOX and high cytotoxicity to cervical cancer cells. The *in vivo* toxicity studies showed very low cytotoxicity, good blood compatibility, and no evident toxic effects in mice. GO-HA/DOX could selectively accumulate in the malignant tumor tissues by receptor-mediated endocytosis and inhibit tumor growth. As described above, GO exhibits size-dependent photoluminescence. The photoluminescence of GO is due to the functionalization of the carbon lattice, which induces the opening of the energy gap. When the absorption of an incident photon occurs, an electron is promoted to a higher energy level orbital, leaving a positively charged hole below (Figure 1.6). This electron-hole pair, created for the absorption of a photon is called an exciton. The creation of an exciton is followed by the non-radiative decay of the electron at the lowest unoccupied molecular orbital (LUMO) and the hole at the highest occupied molecular orbital (HOMO). After this process, a radiative recombination of the exciton generates the emission of a photon with lower energy than the incident photon. Among the non-radiative processes involved, conversion to thermal energy is used for photothermal therapy (PT) of GO. PT uses an optical absorbing agent to generate heat as a result of light radiation, producing a temperature increase that kills the cancer cells[35]. Electromagnetic radiation with a wavelength between 650 and 900 nm (NIR) is very interesting for medical applications because in this window absorption by the skin and tissues is minimal and penetration is intense[92]. The results of GO as a photothermal agent for tumor ablation were presented for the first time in 2010[93]. In this study, single or double layer GO nano-sheets with lateral dimensions between

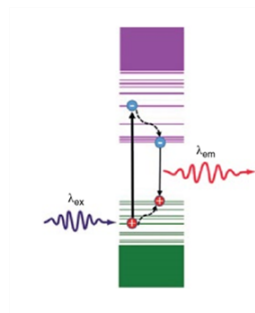


Figure 1.6: Illustration of photoluminescence mechanism of nano-GO

10 and 50 nm coated with amine-terminated six-arm branched PEG (NGS-PEG) were used. To verify the potential in photothermal therapy, an aqueous dispersion of NGS-PEG at a concentration of 0.5 mg/mL was irradiated with a NIR laser at 808 nm with a power density of 2 W cm^{-2} , using water as a control. In contrast to the water sample, the NGS-PEG solution showed a rapid increase in T. The intrinsic photoluminescence of nano-GO and the unique photostability make this material also applicable in the field of biomedical imaging and contrast agent-based imaging techniques used for the early detection of tumors, for understanding the distribution of the nanocarrier in tumors and other organs, for evaluating the therapeutic efficacy, and for post-treatment monitoring[94]. Sun et al. proposed nano-GO sheets with lateral dimensions below 10 nm, obtained by a density gradient ultracentrifugation method used for live cell imaging in the near-infrared (NIR)[81]. In this work, nano-GO was coated with polyethylene glycol and covalently conjugated with a specific Rituxan B-cell antibody (anti-CD20) for selective targeting of B-cell lymphoma cells (nano-GO-PEG-Rituxan). NIR fluorescence images showed that the nano-GO-PEG-Rituxan conjugate was effectively internalized and exhibited luminescence in the visible and NIR regions, although the quantum fluorescence yield was difficult to quantify due to the inhomogeneous species in the sample. The system was also assessed as an anticancer nanocarrier, by loading DOX through non-covalent interactions π -stacking, demonstrating a high loading capacity and selective inhibition of cell growth.

1.1.4 Multi-stage approach in Cancer Therapy

Many of the literature mentioned examples combine simultaneously diagnostics and therapy by exploiting the unique properties of GO nanoparticles. This type of approach, defined with the term theranostics, has great potential in revolutionizing modern medicine. Despite the premises and the enormous achievements, the use of nanosystems in medicine still presents significant challenges. One of the best known problems concerns clearance from the body. As widely described so far, the dimensional reduction of GO in the 10-50 nm range (nano-GO or GOQDs) allows both the increase of some properties already existing in the bulk, such as the surface area and functionalization sites, and the emergence of new properties, such as the light response. Furthermore, GOQDs can be readily internalized by cells via one or more receptor-mediated endocytosis[42]. However, in most applications, the theranostic system is administered intravenously whereby the nanoparticles are delivered directly into the blood circulation and most of the nanoparticles are captured by the Reticuloendothelial system (RES)[95]. The problem of rationally designing nanoparticles able of reaching the site of action without compromising their properties is a general question that does not only concern GOQDs. In 2010, Wong et al proposed a multistage approach in which nanoparticles change their size to facilitate transport by adapting to each physiological barrier[96]. In this approach, gelatin nanoparticles (Gelatin NPs) of 100 nm encapsulated 10 nm quantum dots in the core. After the accumulation in the tumor vasculature by the EPR effect, Gelatin NPs did undergo a size shrinking triggered by matrix metalloproteinase-2 (MMP-2) that are highly expressed in tumor microenvironment and released the 10 nm QDs into the tumor interstitial space (Fig.1.7). The release of QDs with small sizes (~10 nm) enhanced their diffusion in dense collagen matrix of the interstitial space. This innovative approach combines both the long circulation half-life required for the EPR effect and the deep tumor penetration required for release into the tumor dense collagen matrix. If large nanoparticles have long blood circulation time and they are made up of biodegradable materials, the multistep approach can effectively overcome the difficulties in using nanoparticles in the biomed-

cal field.



Figure 1.7: Schematic depiction of the multistage nanoparticle drug delivery system

1.1.5 Oil/Water Nanoemulsions (O/W NEs)

Biodegradable Oil / water nanoemulsions (O/W NEs) were developed in 2014 by the Vecchione team and consist of a biocompatible formulation of drops of soybean oil and Lipoid E80 lecithin dispersed in an aqueous medium. They have the ability to dissolve large quantities of hydrophobic drugs and protect their cargo from hydrolysis and enzymatic degradation. A high-pressure homogenizer is used to achieve the systems long-term stability directly related to their monodispersity[97]. Subsequently, the structure of the nanoemulsions is optimized by progressive depositions around the oil core of natural polymers shells via layer by layer (LbL) technique but with control almost at the molecular scale (Fig.1.8). The secondary nanoemulsions obtained had significant pharmaceutical and clinical advantages, such as ease of manufacture, scalable production, good biocompatibility, biodegradability, reasonable stability and the possibility of incorporating hydrophobic drugs and inorganic nanoparticles. In fact, they have already been tested both to load and release hydrophobic and nutraceutical chemotherapy drugs[98], and to load inorganic contrast agents[99], proving to be promising systems for drug delivery and diagnostics. LbL technology uses the charge-charge interaction between the substrate

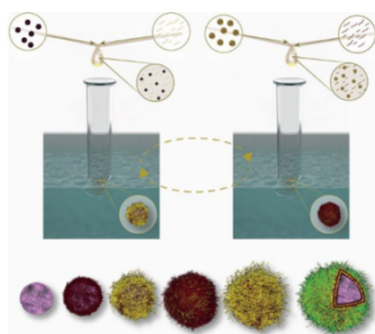


Figure 1.8: Example of controlled deposition of polymeric multilayer film on oil core based nanocapsules

and polyelectrolyte monolayers to construct a multi-layered nano-architecture held together by electrostatic forces. The formation of LbL systems are attributed to electrostatic interactions, hydrogen bonding, hydrophobic interactions and van der Waals forces. However, the electrostatic interactions are weak and easily breakable in physiological environment. Then the architecture of the secondary nanoemulsions has been further improved introducing a covalent bond among layers by means of a metal catalyst-free, light initiated click reaction, namely the thiol-ene reaction[100]. Cross-linked multilayers resulted in more stable systems than those stabilized with just electrostatic forces. The cross-linking between the polymeric layers was then exploited to create stimuli responsive drug delivery systems. In particular, a nanocarrier based on an oil-core and polyelectrolyte layers cross-linked via a MMP-2 cleavable peptide was designed and prepared[101]. MMP-2 cleavable peptide is an octapeptide that contains the sequence Leu-Gly, known to be very sensitive to the action of MMP-2 a family of proteolytic enzymes playing a central role in tumor angiogenesis, progression and invasion by remodelling of the extracellular matrix (ECM). In this elegant structure, the peptide linker plays a dual role for the system. On one side, it enhances nanocarrier stability through the covalent stabilization provided to the shell, which in turn limits off-site toxicity. On the other side, it promotes nano-carrier (NC) disruption in tumor tissues via enzymatic cleavage, hence enabling a site-specific drug release.

1.2 Aim of the PhD project

This thesis aims to develop a multifunctional nanocomposite integrating selective targeting and therapeutics delivery with combined chemo/photothermal therapy. The approach we aim to explore is a multistage approach whereby the complete platform should have the potential to remain relatively stable during blood circulation after intravenous injection and then accumulate in tumor tissues through a passive targeting mechanism based on the EPR effect. The original ~100-nm system preferentially extravasates from the leaky regions of the tumor vasculature. After extravasation into tumor tissue, following an endogenous or exogenous stimulus, smaller 10 nm particles are released and can penetrate the tumor due to their size and their superficial functionalization. To this aim we select nano-graphene oxide animated by the enormous potential of this material. GO is one of the most explored materials in nanomedicine due to its extraordinary intrinsic properties. GO has a high surface area that can be exploited for the loading of drugs and biomolecules, forms stable colloidal dispersions in water and its structure contains a variety of oxygenated functional groups useful for the covalent modification. Furthermore, GO has interesting optical properties useful for phototherapy and biomedical imaging. We decided to prepare GO by wet chemical oxidation of graphite. Already during the first stages of GO preparation we became aware of the problems related to the preparation of this material for biological applications. In particular, our attention was focused on the problems related to obtaining a pure product, in large quantities, with an environmentally friendly method and with dimensions below 50 nm. Enormous efforts have been made in this direction allowing to obtain, as illustrated in **Chapter 2**, a new eco-friendly method to obtain nano-GO in the absence of acid, by combination of mechanical grinding (ball milling) and photo-Fenton reaction. The dry ball milling of graphite allows to obtain a material with a low level of oxidation, but sufficient to create a dispersion in water stable enough to undergo subsequent oxidation by the [OH] radicals generated in the photo-Fenton reaction. Although other studies are needed to increase yields and reduce reaction times, the material obtained with this strategy showed nanometric dimensions around 30 nm, a high degree

of oxidation, excellent stability in water and optical properties similar to the nanometric carbon materials obtained from conventional graphene oxide. At the same time, different types of treatments during synthesis or post-synthesis have been explored in order to obtain or isolate graphene oxide nanosheets with uniform dimensions and less than 50 nm starting from the GO obtained with the classic chemical oxidation of graphite. As described in **Chapter 3**, the best results were obtained by applying an environmentally friendly oxidative cutting promoted by hydrogen peroxide and ammonia. With this approach amino-modified nano-graphene oxide particles with uniform lateral dimensions of less than 20 nm were obtained. Then the surface of the nano-GO nanoparticles was functionalized with hyaluronic acid to increase biocompatibility and to exploit the active targeting properties of this natural polymer. Finally, in **Chapter 4**, we proposed a multistep approach in which the nano-GO nanoparticles were deposited on the O / W nanoemulsion either via layer-by-layer deposition (exploiting the electrostatic interactions) so that small nano-GO nanocarriers can be released upon spontaneous nanoemulsion degradation or through a peptide linker sensitive to metalloproteinases with a faster and more selective release of nano-GO nanocarriers at the tumour site.

References

- [1] Bray F, Ferlay J, Soerjomataram I, Siegel RL, Torre LA, Jemal A. Global cancer statistics 2018: GLOBOCAN estimates of incidence and mortality worldwide for 36 cancers in 185 countries; in *Cancer J Clin*. 2018;68(6):394–424.
- [2] Torre LA, Bray F, Siegel RL, Ferlay J, Lortet-Tieulent J, Jemal A. Global cancer statistics, 2012. CA; in *Cancer J Clin*. 2015;65(2):87–108.
- [3] Srinivasan M, Rajabi M, Mousa SA. Nanobiomaterials in cancer therapy; in *Nanobiomaterials in Cancer Therapy*. Elsevier 2016; p.57–89.
- [4] Iwamoto T. Clinical application of drug delivery systems in cancer chemotherapy: review of the efficacy and side effects of approved drugs; in *Biol Pharm Bull* 2013;36(5):715–8.
- [5] Tomida A, Tsuruo T. Tomida A, Tsuruo T. Drug resistance pathways as targets; in *Anticancer drug Dev* 2002;77–90.
- [6] Sun T, Zhang YS, Pang B, Hyun DC, Yang M, Xia Y. Engineered nanoparticles for drug delivery in cancer therapy; in *Angew Chemie Int* 2014;53(46):12320–64.
- [7] Available from: <http://nano.cancer.gov/resourcecenter/nanocritical.asp>.
- [8] Thrall JH. Nanotechnology and medicine; in *Radiology* 2004;230(2):315–8.

- [9] Liu Y, Miyoshi H, Nakamura M. Nanomedicine for drug delivery and imaging: a promising avenue for cancer therapy and diagnosis using targeted functional nanoparticles; in *Int J cancer* 2007;120(12):2527–37.
- [10] Fleige E, Quadir MA, Haag R. Fleige E, Quadir MA, Haag R. Stimuli-responsive polymeric nanocarriers for the controlled transport of active compounds: concepts and applications; in *Adv Drug Deliv Rev* 2012;64(9):866–84.
- [11] Ventola CL. Progress in nanomedicine: approved and investigational nanodrugs; in *Pharm Ther* 2017;42(12):742
- [12] Suk JS, Xu Q, Kim N, Hanes J, Ensign LM. PEGylation as a strategy for improving nanoparticle-based drug and gene delivery; in *Adv Drug Deliv Rev* 2016;99:28–51.
- [13] Attia ME, Anton N, Wallyn J, Omran Z, Vandamme TF Attia ME, Anton N, Wallyn J, Omran Z, Vandamme TF. An overview of active and passive targeting strategies to improve the nanocarriers efficiency to tumour sites; in *J Pharm Pharmacol* 2019;71(8):1185–98.
- [14] Qiao Y, Wan J, Zhou L, Ma W, Yang Y, Luo W, et al. Stimuli-responsive nanotherapeutics for precision drug delivery and cancer therapy; in *Wiley Interdiscip Rev Nanomedicine Nanobiotechnology* 2019;11(1):e1527.
- [15] Mura S, Nicolas J, Couvreur P. Stimuli-responsive nanocarriers for drug delivery; in *Nat Mater* 2013;12(11):991–1003.
- [16] Vijayakameswara Rao N, Ko H, Lee J, Park JH. Recent progress and advances in stimuli-responsive polymers for cancer therapy; in *Frontiers in Bioengineering and Biotechnology* 2018 :110.
- [17] Zhao CY, Cheng R, Yang Z, Tian ZM. Nanotechnology for cancer therapy based on chemotherapy; in *Molecules* 2018;23(4):826.
- [18] Lo KKW. Inorganic and Organometallic Transition Metal Complexes with Biological Molecules and Living Cells; in *Academic press* 2016.

- [19] Park JH, Von Maltzahn G, Ong LL, Centrone A, Hatton TA, Ruoslahti E, et al. Cooperative nanoparticles for tumor detection and photothermally triggered drug delivery; in *Adv Mater* 2010;22(8):880–5.
- [20] Sakudo A. Near-infrared spectroscopy for medical applications: Current status and future perspectives; in *Clinica Chimica Acta* 2016;455:181–8.
- [21] Tan C, Cao X, Wu XJ, He Q, Yang J, Zhang X, et al. Recent Advances in Ultrathin Two-Dimensional Nanomaterials; in *Chemical Reviews* 2017;117(9):6225–31.
- [22] Novoselov KS, Geim AK, Morozov S V., Jiang D, Zhang Y, Dubonos S V., et al. Electric field in atomically thin carbon films; in *Science* 2004;306(5696):666–9.
- [23] Hu T, Mei X, Wang Y, Weng X, Liang R, Wei M. Two-dimensional nanomaterials: fascinating materials in biomedical field; in *Science Bulletin* 2019;64(22):1707–27.
- [24] Chimene D, Alge DL, Gaharwar AK. Two-Dimensional Nanomaterials for Biomedical Applications: Emerging Trends and Future Prospects; in *Adv Mater* 2015;27(45):7261–84.
- [25] Suryanto. Nanotechnologies Vocabulary Part 13: Graphene and Related Two-Dimensional (2D) Materials; in *ISO: Geneva, Switzerland* 2017.
- [26] Rajakumar G, Zhang XH, Gomathi T, Wang SF, Ansari MA, Mydhili G, et al. Current use of carbon-based materials for biomedical applications-A prospective and review; in *Processes* 2020;8(3):355.
- [27] Obraztsov AN. Making graphene on a large scale; *Nat Nanotechnol* 2009;4(4):212–13.
- [28] Subrahmanyam KS, Panchakarla LS, Govindaraj A, Rao CNR. Simple method of preparing graphene flakes by an arc-discharge method; *J Phys Chem C* 2009;113(11):4257–59.

- [29] Camara N, Rius G, Huntzinger JR, Tiberj A, Mestres N, Godignon P, et al. Selective epitaxial growth of graphene on SiC; *Appl Phys Lett* 2008;93(12):123503.
- [30] Eigler S, Enzelberger-Heim M, Grimm S, Hofmann P, Kroener W, Geworski A, et al. Wet chemical synthesis of graphene; in *Adv Mater* 2013;25(26):3583–87.
- [31] Bianco A, Cheng HM, Enoki T, Gogotsi Y, Hurt RH, Koratkar N, et al. All in the graphene family - A recommended nomenclature for two-dimensional carbon materials; *Carbon* 2013;65:1–6.
- [32] He H, Klinowski J, Forster M, Lerf A. A new structural model for graphite oxide; in *Chem Phys Lett* 1998;287(1–2):53–6.
- [33] Singh DP, Herrera CE, Singh B, Singh S, Singh RK, Kumar R. Graphene oxide: An efficient material and recent approach for biotechnological and biomedical applications; *Materials Science and Engineering C* 2018;86:173–97.
- [34] Gonçalves G, Vila M, Portolés MT, Vallet-Regi M, Gracio J, Marques PAAP. Nano-graphene oxide: A potential multifunctional platform for cancer therapy; *Adv Healthc Mater* 2013;2(8):1072–90.
- [35] Yang K, Feng L, Shi X, Liu Z. Nano-graphene biomedicine: Theranostic applications; in *Chem Soc Rev* 2013;42(2):530–47.
- [36] Liu Z, Robinson JT, Sun X, Dai H. PEGylated nanographene oxide for delivery of water-insoluble cancer drugs; *J Am Chem Soc* 2008;130(33):10876–7.
- [37] Ceriotti G, Romanchuk AY, Slesarev AS, Kalmykov SN. Rapid method for the purification of graphene oxide; in *RSC Adv* 2015;5(62):50365–71.
- [38] Tiliakos A, Cucu A, Ceaus C, Trefilov AMI, Serban EC, Stamatina I. Graphite Oxide Post-Synthesis Processing Protocols; *2nd CommScie International Conference Challenges for Sciences and Society in the Digital Era* 2015 : 33–7.

- [39] Sun L. Structure and synthesis of graphene oxide; *Chinese J Chem Eng* 2019;27(10):2251–60.
- [40] Luo D, Zhang F, Ren Z, Ren W, Yu L, Jiang L, et al. An improved method to synthesize nanoscale graphene oxide using much less acid; *Mater Today Phys* 2019;9:10097.
- [41] Salatin S, Maleki Dizaj S, Yari Khosroushahi A. Effect of the surface modification, size, and shape on cellular uptake of nanoparticles; *Cell Biology International* 2015;39(8):881–90.
- [42] Sanchez VC, Jachak A, Hurt RH, Kane AB. Biological interactions of graphene-family nanomaterials: An interdisciplinary review; *Chemical Research in Toxicology* 2012;25(1):15–34.
- [43] Luo J, Cote LJ, Tung VC, Tan ATL, Goins PE, Wu J, et al. Graphene oxide nanocolloids; *J Am Chem Soc* 2010;132(50):17667–9.
- [44] Rosillo-Lopez M, Salzmann CG. A simple and mild chemical oxidation route to high-purity nano-graphene oxide; *Carbon* 2016;106:56–63.
- [45] Shen S, Wang J, Wu Z, Du Z, Tang Z, Yang J. Graphene quantum dots with high yield and high quality synthesized from low cost precursor of aphanitic graphite; *Nanomaterials* 2020;10(2):375.
- [46] Zhang L, Liang J, Huang Y, Ma Y, Wang Y, Chen Y. Size-controlled synthesis of graphene oxide sheets on a large scale using chemical exfoliation; *Carbon* 2009;47(14):3365–68.
- [47] Zhang H, Peng C, Yang J, Lv M, Liu R, He D, et al. Uniform ultrasmall graphene oxide nanosheets with low cytotoxicity and high cellular uptake; *ACS Appl Mater Interfaces* 2013;5(5):1761–67.
- [48] Fan T, Zeng W, Tang W, Yuan C, Tong S, Cai K, et al. Controllable size-selective method to prepare graphene quantum dots from graphene oxide; in *Nanoscale Res Lett* 2015;10(1):1–8.

- [49] Farazas A, Mavropoulos A, Christofilos D, Tsiaoussis I, Tsipas D. Ultrasound assisted green synthesis and characterization of graphene oxide; *Int J Nanosci Nanotechnol* 2018;14(1):11–17.
- [50] Méndez-Romero UA, Pérez-García SA, Fan Q, Wang E, Licea-Jiménez L. Lateral size reduction of graphene oxide preserving its electronic properties and chemical functionality; *RSC Adv* 2020;10(49):29432–40.
- [51] Posudievsky OY, Khazieieva OA, Koshechko VG, Pokhodenko VD. Preparation of graphene oxide by solvent-free mechanochemical oxidation of graphite; in *J Mater Chem* 2012;22(25):12465–67.
- [52] Mahmoud AED, Stolle A, Stelter M. Sustainable Synthesis of High-Surface-Area Graphite Oxide via Dry Ball Milling; *ACS Sustain Chem Eng* 2018;6(5):6358–69.
- [53] Chen J, Zhang X, Zheng X, Liu C, Cui X, Zheng W. Size distribution-controlled preparation of graphene oxide nanosheets with different C/O ratios; *Mater Chem Phys* 2013;139(1):8–11.
- [54] Huang JJ, Yuan YJ. A sedimentation study of graphene oxide in aqueous solution using gradient differential centrifugation; *Phys Chem Chem Phys* 2016;18(17):12312–22.
- [55] Sun X, Luo D, Liu J, Evans DG. Monodisperse chemically modified graphene obtained by density gradient ultracentrifugal rate separation; *ACS Nano* 2010;4(6):3381–89.
- [56] Li S, Zhu F, Meng F, Li H, Wang L, Zhao J, et al. Separation of graphene oxide by density gradient centrifugation and study on their morphology-dependent electrochemical properties; *J Electroanal Chem* 2013;703:135–45.
- [57] Bidram E, Sulistio A, Amini A, Fu Q, Qiao GG, Stewart A, et al. Fractionation of graphene oxide single nano-sheets in water-glycerol solutions using gradient centrifugation; *Carbon* 2016;103:363–71.

- [58] Zhang W, Zou X, Li H, Hou J, Zhao J, Lan J, et al. Size fractionation of graphene oxide sheets by the polar solvent-selective natural deposition method; *RSC Adv* 2015;5(1):146–52.
- [59] Hu X, Yu Y, Wang Y, Zhou J, Song L. Separating nano graphene oxide from the residual strong-acid filtrate of the modified Hummers method with alkaline solution; *Appl Surf Sci* 2015;329:83–86.
- [60] Chung DDL. Review: Graphite; *Journal of Materials Science* 2002;37(8):1475–89.
- [61] Brodie BC. on the atomic weight of graphite; *Royal Society of London* 1858.
- [62] Staudenmaier L. Procedure for the preparation of graphitic acid; *Ber Dtsch Chem Ges* 1899;32:1394.
- [63] Hummers WS, Offeman RE. Preparation of Graphitic Oxide; *J Am Chem Soc* 1958;80(6):1339.
- [64] Shamaila S, Sajjad AKL, Iqbal A. Modifications in development of graphene oxide synthetic routes; in *Chemical Engineering Journal* 2016;294:458–77.
- [65] Brisebois PP, Siaj M. Harvesting graphene oxide-years 1859 to 2019: A review of its structure, synthesis, properties and exfoliation; *Journal of Materials Chemistry C* 2020;8(5):1517–47.
- [66] Marcano DC, Kosynkin D V, Berlin JM, Sinitskii A, Sun Z, Slesarev A, et al. Improved synthesis of graphene oxide; *ACS Nano* 2010;4(8):4806–14.
- [67] Chen J, Yao B, Li C, Shi G. An improved Hummers method for eco-friendly synthesis of graphene oxide; *Carbon* 2013;64:225–29.
- [68] Batalha W, Gargarella P, Kiminami CS. Novo Protocolo De Obtenção De Óxido De Grafite; 22^o CBECiMat - Congr Bras Eng e Ciência dos Mater Natal, RN, Bras 2016.

- [69] Shen J, Hu Y, Shi M, Lu X, Qin C, Li C, et al. Fast and facile preparation of graphene oxide and reduced graphene oxide nanoplatelets; *Chem Mater* 2009;21(15):3514–20.
- [70] Peng L, Xu Z, Liu Z, Wei Y, Sun H, Li Z, et al. An iron-based green approach to 1-h production of single-layer graphene oxide; *Nat Commun* 2015;6(1):1–9.
- [71] Sofer Z, Luxa J, Jankovský O, Sedmidubský D, Bystroň T, Pumera M. Synthesis of Graphene Oxide by Oxidation of Graphite with Ferrate(VI) Compounds: Myth or Reality?; *Angew Chemie - Int Ed* 2013;128(39):12144–8.
- [72] Liu J, Yang H, Zhen SG, Poh CK, Chaurasia A, Luo J, et al. A green approach to the synthesis of high-quality graphene oxide flakes via electrochemical exfoliation of pencil core; *RSC Adv* 2013;3(29):11745–50.
- [73] Gao X, Jiang DE, Zhao Y, Nagase S, Zhang S, Chen Z. Theoretical insights into the structures of graphene oxide and its chemical conversions between graphene; *Journal of Computational and Theoretical Nanoscience* 2011;8(12):2406–22.
- [74] Li C, Chen X, Shen L, Bao N. Revisiting the Oxidation of Graphite: Reaction Mechanism, Chemical Stability, and Structure Self-Regulation; *ACS Omega* 2020;5(7):3397–3404.
- [75] Dimiev AM, Tour JM. Mechanism of graphene oxide formation; *ACS Nano* 2014;8(3):3060–8.
- [76] Dimiev AM, Shukhina K, Khannanov A. Mechanism of the graphene oxide formation. The role of water, "reversibility" of the oxidation, and mobility of the C-O bonds; *Carbon* 2020;166:1–14.
- [77] Gonçalves G, Vila M, Bdikin I, De Andrés A, Emami N, Ferreira RAS, et al. Breakdown into nanoscale of graphene oxide: Confined hot spot atomic reduction and fragmentation; *Sci Rep* 2014;4(1):1–8.

- [78] Kosynkin D V., Higginbotham AL, Sinitskii A, Lomeda JR, Dimiev A, Price BK, et al. Longitudinal unzipping of carbon nanotubes to form graphene nanoribbons; *Nature* 2009;458(7240):872–6.
- [79] Muñoz R, Singh DP, Kumar R, Matsuda A. Graphene Oxide for Drug Delivery and Cancer Therapy; *Nanostructured Polymer Composites for Biomedical Applications* 2019; 447–4888.
- [80] Lonkar SP, Deshmukh YS, Abdala AA. Recent advances in chemical modifications of graphene; *Nano Research* 2015;8(4):1039–74.
- [81] Sun X, Liu Z, Welsher K, Robinson JT, Goodwin A, Zaric S, et al. Nano-graphene oxide for cellular imaging and drug delivery; *Nano Res* 2008;1(3):203–12.
- [82] Zhang L, Xia J, Zhao Q, Liu L, Zhang Z. Functional graphene oxide as a nanocarrier for controlled loading and targeted delivery of mixed anti-cancer drugs; *Small* 2010;6(4):537–44.
- [83] Szakács G, Paterson JK, Ludwig JA, Booth-Genthe C, Gottesman MM. Targeting multidrug resistance in cancer; *Nature Reviews Drug Discovery* 2006;35(3):219–34.
- [84] Layek RK, Nandi AK. A review on synthesis and properties of polymer functionalized graphene; *Polymer* 2013;54(19):5087–5103.
- [85] Layek RK, Samanta S, Chatterjee DP, Nandi AK. Physical and mechanical properties of poly(methyl methacrylate)-functionalized graphene/poly(vinylidene fluoride) nanocomposites: Piezoelectric β polymorph formation; *Polymer (Guildf)* 2010;51(24):5846–56.
- [86] Sydlik SA, Swager TM. Functional graphenic materials via a Johnson-Claisen rearrangement; *Adv Funct Mater* 2013;23(15):1873–82.
- [87] Zhang X, Huang Y, Wang Y, Ma Y, Liu Z, Chen Y. Zhang X, Huang Y, Wang Y, Ma Y, Liu Z, Chen Y; *Carbon* 2009;47(1):334–7.

- [88] Yu D, Yang Y, Durstock M, Baek JB, Dai L. Soluble P3HT-grafted graphene for efficient bilayer-heterojunction photovoltaic devices; *ACS Nano* 2010;4(10):5633–40.
- [89] Singh SK, Singh MK, Kulkarni PP, Sonkar VK, Grácio JJA, Dash D. Amine-modified graphene: Thrombo-protective safer alternative to graphene oxide for biomedical applications; *ACS Nano* 2012;6(3):2731–40.
- [90] Singh SK, Singh MK, Nayak MK, Kumari S, Shrivastava S, Grácio JJA, et al. Thrombus inducing property of atomically thin graphene oxide sheets; *ACS Nano* 2011;5(6):4687–96.
- [91] Wu H, Shi H, Wang Y, Jia X, Tang C, Zhang J, et al. Hyaluronic acid conjugated graphene oxide for targeted drug delivery; in *Carbon* 2014;69:379–89.
- [92] Weissleder RA. A clearer vision for in vivo imaging; *Nat Biotechnol* 2001;19(4):316–7.
- [93] Yang K, Zhang S, Zhang G, Sun X, Lee ST, Liu Z. Graphene in mice: Ultra-high in vivo tumor uptake and efficient photothermal therapy; *Nano Lett* 2010;10(9):3318–23.
- [94] Stankovich S, Dikin DA, Piner RD, Kohlhaas KA, Kleinhammes A, Jia Y, et al. Synthesis of graphene-based nanosheets via chemical reduction of exfoliated graphite oxide; *Carbon* 2007;45(7):1558–65.
- [95] Choi HS, Liu W, Misra P, Tanaka E, Zimmer JP, Ipe BI, et al. Renal clearance of quantum dots; *Nat Biotechnol* 2007;25(10):1165–70.
- [96] Wong C, Stylianopoulos T, Cui J, Martin J, Chauhan VP, Jiang W, et al. Multi-stage nanoparticle delivery system for deep penetration into tumor tissue; *Proc Natl Acad Sci U S A* 2011;108(6):2426–31.
- [97] Vecchione R, Ciotola U, Sagliano A, Bianchini P, Diaspro A, Netti PA. Tunable stability of monodisperse secondary O/W nano-emulsions; *Nanoscale* 2014;6(15):9003–7.

- [98] Vecchione R, Quagliariello V, Calabria D, Calcagno V, De Luca E, Iaffaioli R V, et al. Curcumin bioavailability from oil in water nano-emulsions: In vitro and in vivo study on the dimensional, compositional and interactional dependence; *J Control Release* 2016;233:88–100.
- [99] Vecchione R, Quagliariello V, Giustetto P, Calabria D, Sathya A, Marotta R, et al. Oil/water nano-emulsion loaded with cobalt ferrite oxide nanocubes for photo-acoustic and magnetic resonance dual imaging in cancer: in vitro and preclinical studies; *Nanomedicine Nanotechnology, Biol Med* 2017;13(1):275–86.
- [100] Calcagno V, Vecchione R, Sagliano A, Carella A, Guarnieri D, Belli V, et al. Biostability enhancement of oil core - polysaccharide multilayer shell via photoinitiator free thiol-ene "click" reaction; *Colloids Surfaces B Biointerfaces* 2016;142:281–9.
- [101] Iaccarino G, Profeta M, Vecchione R, Netti PA. Matrix metalloproteinase-cleavable nanocapsules for tumor-activated drug release; *Acta Biomater* 2016;89:265–78.

Chapter 2

**photo-Fenton reaction graphite ball
milled to obtain nano-GO**

2.1 Abstract

Graphene oxide (GO) is a material that has aroused enormous scientific and application interest due to its properties that make it versatile in many technological and industrial fields and for its role as a precursor in the large-scale production of graphene. The classical large-scale preparation of GO, although much studied, still involves the liquid phase oxidation of graphite with strong oxidants and concentrated acid media. This method raises many concerns due to the high amount of acids used and the disposal of waste water. It is therefore desirable to find safe, economical and environmentally sustainable preparation methods. Here we report a strategy to obtain nano-GO in the absence of acid, by combination of mechanical grinding (ball milling) and photo-Fenton reaction. The dry ball milling of graphite allows to obtain a material with a low level of oxidation, but sufficient to create a dispersion in water stable enough to undergo subsequent oxidation by the OH radicals generated in the photo-Fenton reaction.

2.2 Introduction

Graphene oxide (GO) is a single or few-layered material with a high oxygen content, characterized by a non-stoichiometric atomic composition with an atomic C / O ratio typically between 3.00 and 2.00[1]. Despite extensive theoretical and experimental studies, there is still no unambiguous definition or reference standard for this material[2]. Over the years, different formulas have been proposed to describe its chemical composition[3,4] and numerous models to explain its structure[5-11]. In 1998, Lerf and Klinowski, using modern scientific techniques, proposed a model, still very popular, considering GO a two-dimensional material consisting of both aromatic and conjugated non-oxidized crystalline regions and amorphous regions with sp^3 hybridized carbon atoms linked to oxygen-containing functional groups, such as alcohols and epoxides on the basal planes and carbonyl/carboxyl groups and 5-, 6-membered lactol rings on the edges[9]. Initially considered an intermediate in the graphene production process by wet chemical exfoliation of graphite, GO was then treated as an independent material for both basic research and practical applications due to its unique properties. Unlike the perfectly ordered aromatic structure of graphene, GO exhibits a defective structure rich in oxygenated functional groups which give this material the ability to form stable colloidal solutions in water and low molecular weight alcohols[12]. The hydrophilic nature of GO allows applications in an aqueous environment, such as biomedical applications as a platform for the delivery of pharmacological molecules[13], catalysis[14], purification treatments of wastewater[15], and production of transparent conductive films[16]. Furthermore, the oxygenated functionalities located on the edges and the basal planes of the structure provide functionalization sites to suitably tuning the chemical-physical properties of the material. The chemical structure and properties of GO depend on the degree of oxidation and the synthesis method prepare the material[17]. GO is usually prepared by graphite oxidation with strong chemical oxidants[18], high temperatures[19], ozone[20], or electrochemical processes[21]. Among these methods, the chemical oxidation of graphite in solution remains the most economical and scalable method for obtaining good quality GO in large yields. The recipes for graphite oxidation

still used today, although with some modification, are almost all based on the method proposed by Hummers and Offeman in 1958[22]. This method involves treating flaked or powdered graphite with strong chemical oxidants (KMnO_4) in a concentrated acid medium (H_2SO_4 , H_3PO_4 , or their mixture). After a controlled dilution step, the resulting mixture is treated with H_2O_2 to exfoliate the formed GO sheets. The yellow-brown solid formed is separated from the acid mixture and washed with dilute HCl to remove metal ion impurities and then washed thoroughly with water to neutralize the solution[23]. Although this method has undergone several revisions over the years and many modifications have been proposed to improve the quality of the material obtained and environmental sustainability[24-26], it remains a method that requires extensive and tedious workup[27]. Numerous workup procedures are reported in the literature, the common denominator of all being an extensive dilution of acids[28,29]. During the process, huge quantities of water are used to neutralize the acids and to remove the salts formed by the oxidation mixture. The wastewater obtained, therefore, contains various manganese, potassium, and sulphur ions, and their treatment and subsequent disposal represent a bottleneck in the marketing of GO on a large scale. Another issue that deserves attention in the GO production and marketing process concerns the amount of sulphuric acid required for the oxidation of graphite. Generally, more than 15 mL of concentrated sulphuric acid is required for each gram of graphite[30]. Such a large amount of acid is needed both to intercalate the graphene layers tightly packed in the crystal lattice of graphite and to stabilize the Mn_2O_7 intermediate that is formed from the reaction of H_2SO_4 and KMnO_4 , and that if it does not react further with other acids it could cause explosions[31]. This represents a major limit both for the risks associated with the use of large quantities of concentrated acids and for the costs relating the disposal. Moreover, since the graphene oxide formation depends on the rate at which the oxidants intercalate between the graphene layers in the graphite, the dimensional heterogeneity of the starting material results in a heterogeneous size distribution of the product. Therefore, the graphene oxide obtained with the classic wet exfoliation of graphite has a wide distribution of dimensions between few nanometers to hundreds of micrometers. Obtaining a material with a narrow dimensional dis-

tribution and in the nanometer range is crucial for many applications such as batteries[32], desalination[33], cellular imaging and drug delivery[34], Among the recognized methods for increasing the distance between graphene layers of graphite and facilitating the access of reagents, mechanochemical milling is considered an efficient and sustainable approach. The method was developed in 1970 by John Benjamin to synthesize oxide dispersion strengthened capable of withstanding high temperature and pressure[35]. The process consists of inserting the powder to be ground, possibly together with solvents or surfactants, into a rotating selected to cylindrical grinding jar (ball mill) filled with loose grinding balls[36]. During rotation, collisions between the balls and the jar create impact forces and shear forces that reduce the size of the powder and generate enough kinetic energy to break the bonds in the aromatic structure of the powder. Hence, the mechanical stress produced in the ball mill not only reduces the size of the material but also increases the proportion of highly active regions on its surface through the cleavage of strong bond interactions[37]. Several research groups have applied mechanical milling to produce GO, both in dry conditions with powder oxidants and in wet conditions with stoichiometric quantities of acids. Table 2.4 in the supporting information summarizes the main works in this direction. Also, it is possible to use mechanochemical ball milling for the GO production without additional oxidants other than air that fills the jar[38]. Dry milling of graphite using only oxygen from the atmosphere in the closed reaction vessel results in a GO with an oxygen content that increases with increasing milling time, but which does not exceed the value of 14% by weight[39]. However, the formed material can achieve a degree of oxidation that makes it dispersible in water and therefore act as an active precursor for other environmentally friendly processes. In 1894, H.J. Fenton describes the oxidation of tartaric acid by hydrogen peroxide catalysed by ferrous ions[40]. Since then, the Fenton reaction has been extensively used in various fields especially in the decomposition of organic pollutants in water[41-43]. In the presence of Fe^{3+}/Fe^{2+} catalysis, H_2O_2 can be efficiently decomposed to generate hydroxyl radicals ($\cdot OH$) with strong oxidizing power, and degrade various organic compounds into CO_2 , H_2O and other small molecules[44]. It was later shown that the Fenton reaction rate increases in the presence of external ir-

radiation, such as ultraviolet (UV) light (photo-Fenton reaction)[45]. This improvement in the reaction can be attributed to the continuous regeneration of Fe^{2+} due to the photochemical effect of light. This reverse cycle of $\text{Fe}^{2+} \rightarrow \text{Fe}^{3+} \rightarrow \text{Fe}^{2+}$ will generate hydroxyl ions as long as hydrogen peroxide is present in solution[46]. The photo-Fenton reaction was also applied to graphene and GO, mainly to investigate the biodegradation products of these carbon nanomaterials[47] and to prepare graphene quantum dots with a controlled quality and typology of oxygenated functional groups[48]. Understanding the urgency to find more environmentally friendly methods for the production of highly oxidized GO, and inspired by the fact that already Brodie in his first work on the preparation of GO observes that sunlight can favour the formation of GO, in the present study we present a new, sustainable way to prepare GO by combining mechanical milling and the Photo-Fenton reaction by completely avoiding the use of acids. To the best of our knowledge, this is the first time that a completely acid-free protocol exploiting ball milling and Photo-Fenton reaction has been used for the production of GO at the nanoscale.

2.3 Methods

2.3.1 Materials

Graphite (flakes, +100 mesh), 30% hydrogen peroxide (H_2O_2), ferric chloride ($\text{FeCl}_3 \cdot 6\text{H}_2\text{O}$) were purchased from Sigma-Aldrich. Dialysis membranes were purchased from Spectrum Laboratories Inc. All of the reagents were used as received. Deionized water was used throughout the experiments.

2.3.2 Preparation of GO by Ball Milling

Graphite flakes (8g) were milled in a 125 mL zirconia milling jar with 5 mm zirconia milling balls (balls:graphite weight ratio 7:1), by means of a Retsch PM100 planetary ball mill (Retsch GmbH, Haan, Germany). The rotation speed of the mill was set to 500 rpm. The milling was carried out for a total time of 36 h; after 24 h, the jar was opened to allow fresh air inside, then the milling was contin-

ued for further 12 h. The oxidized graphite obtained was dispersed in water (2 mg/mL) for 1 h using ultrasound (ultrasonic bath Falc Instruments) with a power of 20 W to achieve exfoliation. The prepared dispersion was subjected to centrifugation at 4000 rpm for 1 h and the upper half of their volume was selected for the next reaction. Concentration of the solution was calculated by taking a portion of the suspension, evaporating water to dryness under vacuum, and measuring mass of the residue.

2.3.3 Photo-Fenton Reaction of GO Ball Milled

The photo-Fenton reaction of GO ball milled was carried out in a photoreactor (Multirays, Helios Italquartz) equipped with ten 15W lamps with a maximum at 366 nm (UVA). In a typical experiment, 125 mL of 0.5mg/mL GO ball milled aqueous suspension was mixed with 100 mL of 20 mM H₂O₂, and 500 μ L of 1.0 mM FeCl₃ under vigorous stirring. The resulting mixture was transferred into 10 quartz tubes and irradiated for 36h. The reaction product was recovered, dialyzed in ultrapure water (MWCO 100-500 Da), lyophilized and stored at room T for characterizations.

2.3.4 Instrumentations

The morphology of the graphene oxide sheet was imaged using scanning electron microscopy (SEM) equipped with energy dispersive X-ray spectroscopy (EDX). 20 μ l of graphene oxide (1mg/mL) were deposited on a standard SEM pin stub and analysed by FESEM ULTRA-PLUS (Zeiss) (Milan, Italy) with the SE2 detector. Cryo-TEM analysis was performed using a Tecnai G2 F20 transmission electron microscope (FEI Company, the Netherland) equipped with a Shotky field emission gun operating at an acceleration voltage of 200 kV and recorded at low dose with a 2k x 2k Ultrascan (Gatan, USA) CCD camera. Frozen hydrated samples were prepared by applying a 3 μ l aliquot to a previously glow discharged 200 mesh holey carbon grid (Ted Pella, USA). Before plunging into nitrogen cooled liquid ethane, the grid was blotted for 1.5 s in a chamber at 4 °C and 90% humidity using a FEI Vitrobot Mark IV (FEI company, the Netherlands). The thickness of the graphene oxide sample was measured on a mica

surface by using a Multimode Nanoscope V scanning probe microscopy system (Bruker, USA) with a AFM cantilever tips with a force constant of ~ 50 N/m and resonance vibration frequency of ~ 350 kHz (Bruker, USA). The samples were prepared by solution casting the aqueous suspensions of GO on a freshly cleaved mica surface and drying in air. The size distribution and the ζ potential in solution of the GO sample was detected using dynamic light scattering (DLS) instrument (Zetasizer zs nano series ZEN 3600, Malvern Instruments Ltd., Malvern, U.K., λ 632.8 nm). All the samples were diluted up to a droplet concentration of approximately 0.025 wt% by using milli-Q water. A detecting angle of 173° was used. A default refractive index ratio (1.5900) and 5 runs for each measurement (1 run lasting 100 s) were used in the calculations of the particle size distribution. ζ -potential analysis was carried out by setting 50 runs for each measurement. The chemical information was revealed by X ray photoelectron spectroscopy (XPS) using a PHI5000 VersaProbeII XPS spectrometer with a monochromatic Al-K- α source of 1486.68 eV. The high resolution C1s spectra were acquired at high power (100 W) with a Pass Energy of 23.5 eV, 0.1 eV step size, and averaged over 20 scans. Spectra from insulating samples were corrected by shifting all peaks to the adventitious carbon C1s spectral component binding energy set at 284.8 eV. Multipack software was used to process all the spectra. The Fourier transform infrared spectroscopy (FTIR) spectrum was recorded using a Nicolet iS50 spectrometer with the assistance of attenuated total reflectance. Raman spectra were recorded from powder at room temperature via a confocal Raman microscope (Jasco, NRS- 3100) with a 514 nm line of water-cooled Ar⁺ laser, 4 mW at the sample. Photoluminescence spectra were obtained using a spectrophotometer LS55 (Perkin Elmer) after diluting the samples dispersions to a concentration of 150 $\mu\text{g}/\text{mL}$. The ultraviolet-visible (UV/Vis) spectra of the samples were measured using a Cary 5000 UV/Vis spectrophotometer. Absorbance spectra were acquired after diluting the GO samples prepared for fluorescence measurements by a factor of 10 in water.

2.4 Results

2.4.1 Synthesis

Mechanical milling treatment of pure graphite without chemical oxidants and acidic media leads to graphene oxide with low oxygen content. In our method, graphite flakes (G 8g) were mechanically milled in a planetary ball mill with zirconia grinding medias. After 24 h milling, a pressure drop inside the container was observed, which suggests that the oxidation reaction of the graphite, in the absence of other oxidants, occurred by the atmospheric oxygen inside the closed jar. The original shiny grey flakes appeared as a very fine black powder with few larger, translucent graphite-like fragments (Fig. 2.1). After additional 12 h of milling, the powder was recovered from the jar and weighed (10.89g). Although a quantitative determination of weight gain was prevented by the incomplete recovery of milled graphite, as some material was lost on the surface of the milling media, the starting material gained weight after the ball milling process, probably indicating oxygen incorporation. A suspension was obtained by adding 200 mg of carbon material to 10 mL of deionized water followed by ultrasonication for 30 min. The prepared dispersions were subjected to centrifugation at 4000 rpm for 1 h to remove unreacted graphite flakes and larger particles and the upper half of their volume was selected. GO concentration was calculated by taking a portion of the suspension, evaporating water to dryness under vacuum, and measuring the mass of the residue (GO ball milled (GO_{bm}) 0.5mg/mL). This solution was subjected to photo-Fenton reaction as described in the materials and methods section. In literature, it is reported that radiation power plays a fundamental role in reaction kinetics. In particular, graphene quantum dots with carboxylic groups on the edges were easily obtained in a UV power depending time by irradiating graphene oxide obtained with the modified Hummers method[44]. By using a photoreactor equipped with ten 15W lamps, we observed that in the first 16 h (GO Fenton 16h (GO_{F16h})) there were no changes in the solution aspect whereas, after 32 h (GO Fenton 32h (GO_{F32h})), the grey solution became clearer and assumed a yellow-brown color typical of graphene oxide. Further 16 h (GO Fenton 48



Figure 2.1: Graphite flakes (left), graphite ball milled (right) photographs

h GO_{F48h}), a dark precipitate was formed. So we recovered the material after 32 h of irradiation. The reaction product was recovered, purified by dialysis in ultrapure water (MWCO 100-500 Da), and lyophilized (GO_{F32h} 19.2mg, yield 30.7%).

2.4.2 Morphological Characterization and Size Evaluation

Scanning Electron Microscopy (SEM) images were acquired to investigate the morphology of the samples obtained, as shown in Fig 2.2 (a-f). The pristine graphite (G, Fig. 2.2 (a,b)) showed a flaky morphology with smooth surface and an average particle size around $450 \mu\text{m}$. SEM micrographs of the sample after mechanical grinding (GO_{bm} , Fig 2.2 (c,d)) showed an obvious change in morphology. The sample had completely lost the flake-like structure and instead showed a porous and irregular network with a wide particle size distribution. After the photo-Fenton reaction, the decrease in particle size was evident. The material obtained had a crumpled and thin sheet structure with different transparencies, tightly connected to each other to form darker aggre-

gation areas. The transparent regions confirmed the presence of single or few-layered exfoliated graphene oxide sheets. The decrease in lateral dimensions at the nanoscale creates a high surface energy which results in the formation of dense aggregates[45]. Energy dispersive X-ray spectroscopy (EDX) measure-

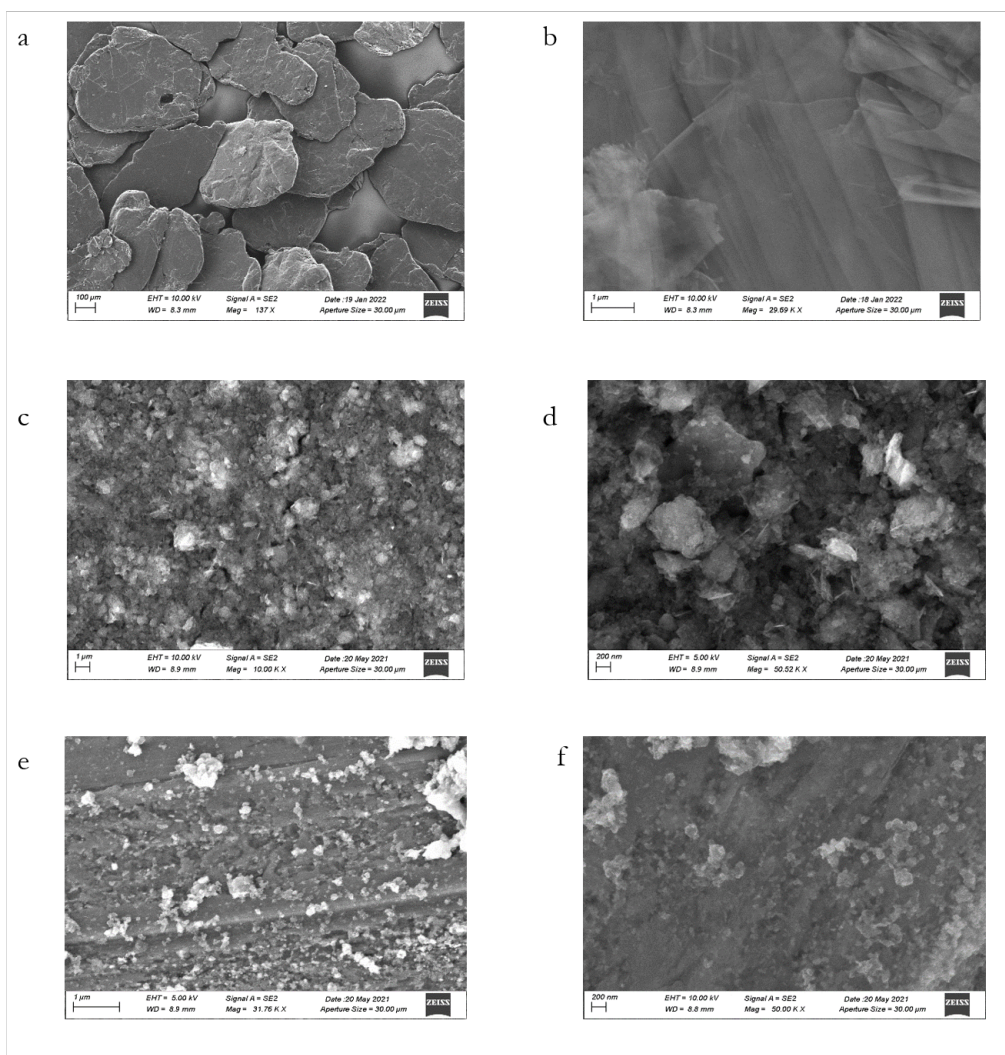


Figure 2.2: SEM micrographs at different magnifications of (a,b) pristine graphite G; (c,d) GO ball milled $GO_{bm.}$; (e,f) GO-Fenton GO_{F32h}

ments were performed to analyse the relative elemental composition on the surface and to verify the degree of purity of the samples obtained. As shown in Fig. 2.3 (a, b), mechanical milling in the zirconia jar did not introduce impurities on the sample surface which contains only oxygen in addition to carbon.

On the other hand, in the sample treated with the Fenton reaction, EDX analysis showed the presence of iron due to the ferric chloride catalyst. In principle the presence of iron does not represent an issue from an applicative point of view, conversely, several monohybrids based on graphene oxide and inorganic compounds have attracted potential attention in many applications ranging from electromagnetic devices to magnetically guided drug delivery systems [46-48]. Cryogenic Transmission Electron Microscopy (cryo-TEM) allowed the observa-

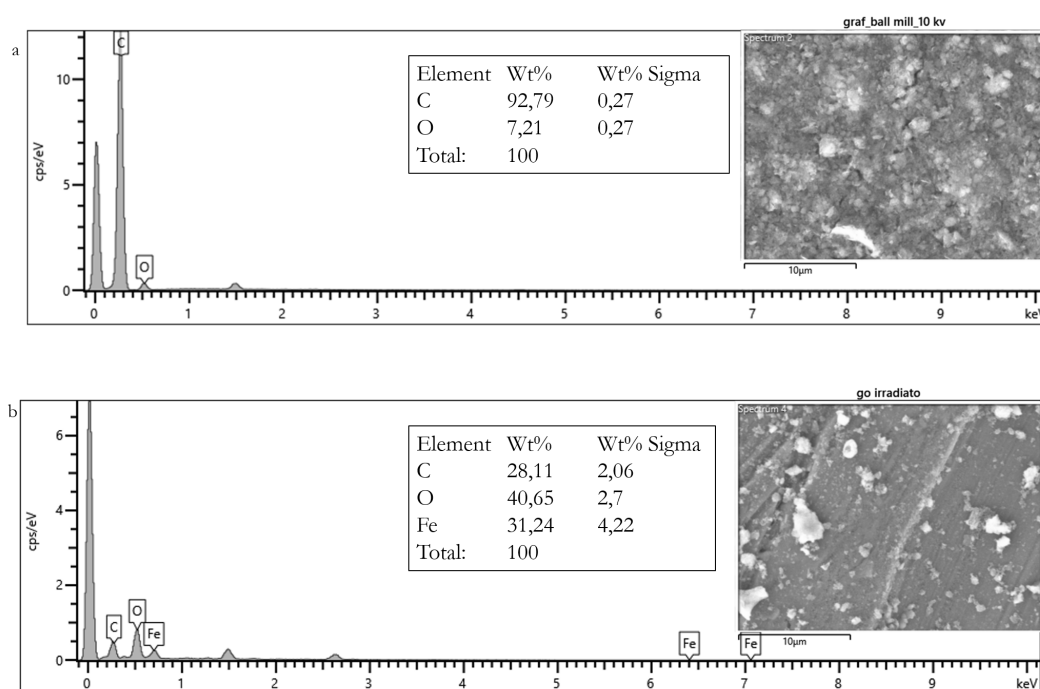


Figure 2.3: EDX spectra of a) GO ball milled GO_{bm} ; b) GO Fenton GO_{F32h}

tion of GO_{F32h} nano sheets in water avoiding the aggregation phenomena due to the drying of the sample and the structural deformations due to the vacuum of the microscope. Cryo-TEM images (Fig.2.4) showed individual sheets of circular-like morphology homogeneously dispersed with a size distribution centred at around 28 nm. The size distribution of the obtained samples was also determined by dynamic light scattering (DLS) analysis and the results are shown in Fig.2.11 in Supporting Information. For GO_{bm} a size distribution centered at 232.9 nm was found with a polydispersity index of 0.297 indicating polydisperse particle size distributions. For GO_{F32h} , on the other hand, a size

of 28.88 nm was obtained with a PDI of 0.188 which correlated well with the CryoTem measurements. Atomic force microscopy (AFM) imaging confirmed

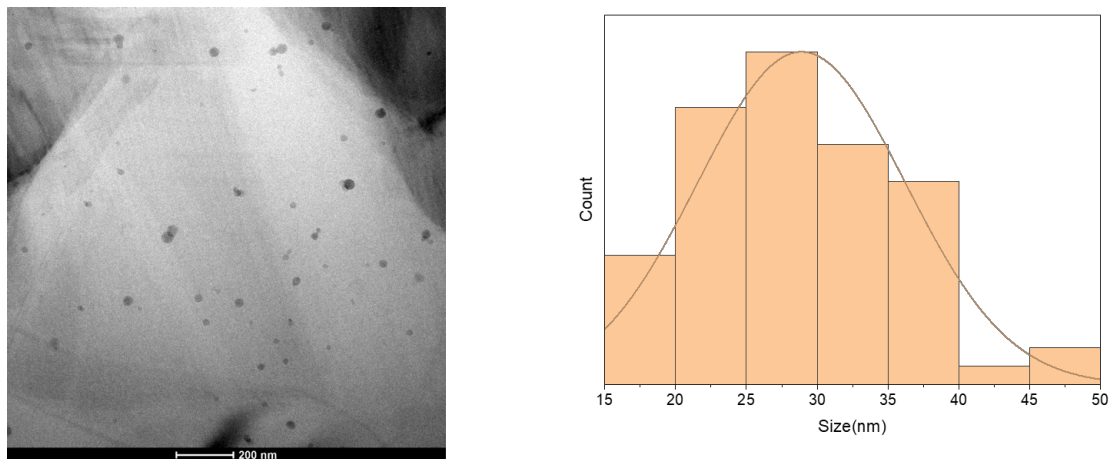


Figure 2.4: Cryo-Tem image and Size Distribution GO_{F32h}

the decrease in lateral dimensions (Fig. 2.5). After the photo-Fenton reaction, the sample was more exfoliated than the ball milled sample. The average thickness, measured from the height profile of the AFM images, was around 5 nm for GO_{bm} , and between 1-2 nm, typical of single and double layers of graphene oxide. Structural and chemical defects introduced into the carbonaceous lattice of graphite were also evaluated with Raman spectroscopy. The Raman spectra at low and high frequencies of the graphite and of the samples obtained were shown in Fig. 2.6. In the Raman spectrum of pristine graphite, the G band was present at 1583 cm^{-1} and the 2D band at 2728 cm^{-1} . The first band is due to the vibrations in the plane of the aromatic structure of Csp^2 , while the last is related to the stacking order of the graphite. When the graphite periodic lattice is perturbed by defects (functional groups, holes or vacancies), the shape of the bands changes and new forbidden Raman bands appear. After mechanical milling, a new band (D band) at 1346 cm^{-1} appeared in the Raman spectrum of the sample, associated with the presence of edge defects and distortions. In addition, the G band became wider and presented a small shoulder (D' band) indicative of the presence of a few layers of graphene, as evidenced by the AFM measurements. At high frequencies, the 2D band appeared much more symmetrical and a new band appeared at about 2930 cm^{-1} , known as the D + D'

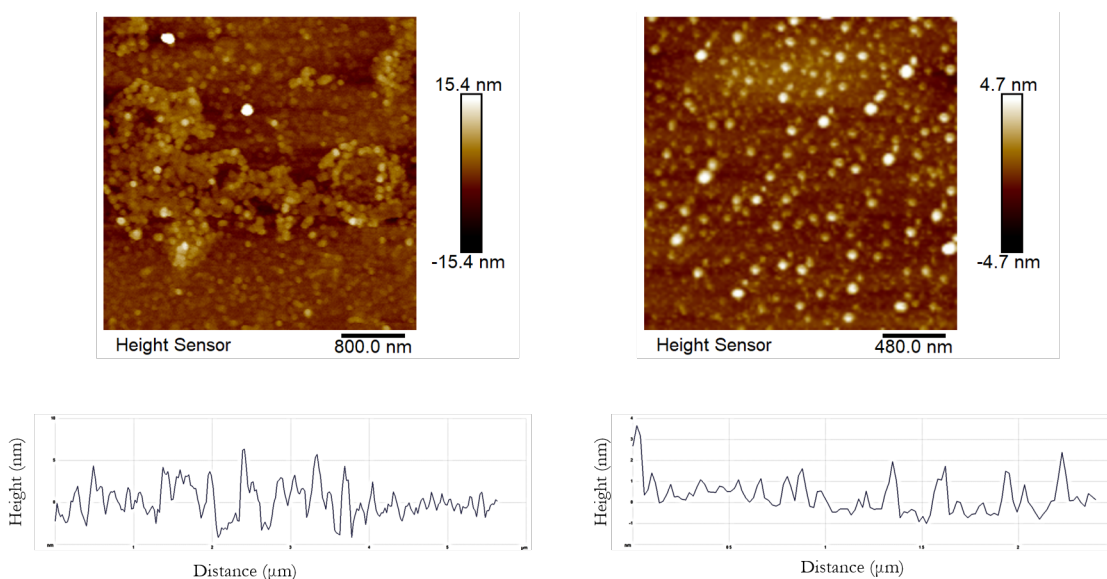


Figure 2.5: AFM Images (top) and height profile of the AFM images (bottom) of a) GO ball milled GO_{bm} ; b) GO Fenton GO_{F32h}

combination band activated by the presence of defects. The Raman spectrum of the sample after the photo-Fenton reaction had characteristics similar to that of the GO_{bm} , the shoulder on the G band was more pronounced sign of the greater exfoliation in single or few layers and the 2D band was less intense than the GO_{bm} , due to the breaking of the stacking order of the C-C bonds and the increase in the oxidation state. Table 2.1 reported the position, the total width at half height, the intensity and the relationships between the intensities of the main Raman bands. The ratio between the intensities of the D and G bands (I_D/I_G) provides indications on structural defects. This ratio was zero in graphite, for the absence of structural defects, increased in GO_{bm} due to reduction in size and increase in oxygenated functional groups and reached 1.08 in GO_{F32h} . This value is compatible with that reported in the literature (0.98) for a GO monolayer with a large amount of defects[49].

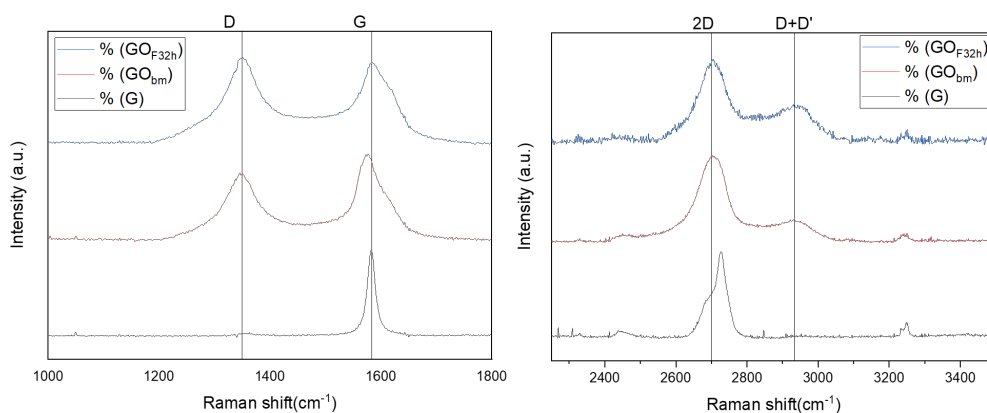


Figure 2.6: Low (left) and high (right) Frequency Raman spectra of G, GO_{bm} , and GO_{F32h}

	G	GO_{bm}	GO_{F32h}
G	1583.79	1577.64	1586.99
D		1346.94	1349.79
2D	2728.55	2703.42	2702.95
D+D'		2932.52	2933.85
I_G	742.69	781.42	407.61
I_D		595.37	441.58
$FWHM_G$	16.6397	53.0384	63.9322
$FWHM_D$		61.6359	62.2523
I_D/I_G	0	0.76582	1.08337

Table 2.1: Raman parameters for G, GO_{bm} and GO_{F32h}

2.4.3 Products Composition

X-ray photoelectron spectroscopy (XPS) was used to investigate the degree of oxidation of the products obtained, the composition and nature of the oxygenated functional groups present. XPS survey spectra for pristine graphite (G), GO ball milled (GO_{bm}); and GO-Fenton (GO_{F32h}) were reported in Fig. 2.7. For pristine graphite, the minor O1s peak was due to small amounts of physisorbed oxygen (Fig.2.7 a). In the sample after ball milling, (GO_{bm}) a slight increase in oxygen concentration, along with a reduction in the carbon content, was observed (Fig. 2.7 b). After the Fenton reaction, the oxygen content increased up to 48% indicating the effective oxidation of the sample. As

already noted by the EDX analyses, the presence of iron-related peaks was also observed in the GO_{F32h} survey spectrum (Fig. 2.7 c). Table 2.2 shows the atomic concentrations of C1s and O1s and their ratios for the three samples. In order to

Sample	C1s(%)	O1s(%)	O/C(%)
G	95.02	4.98	5.24
GO_{bm}	92.88	7.12	7.67
GO_{F32h}	34.9	48.0	137.5

Table 2.2: C1s and O1s Atomic Concentrations and their ratio from XPS Survey Spectra

identify the oxygen-containing functional groups that formed on the edges and basal planes of the carbonaceous lattice after the two processes, the high resolution C1s core level spectra of all the sample were deconvoluted into different binding energies (B.E.) (Fig.2.7). Four components have been fitted for each sample with Gaussian peaks centred at 284.0-284.5, 286.0-286.2, 286.5-286.6, 288.4-228.6 corresponding to C=C/C-C; C-OH; C-O-C; C=O/COOH, as summarized in Table 2.3. The peak at 284.12 eV in the C1s XPS spectrum of pristine graphite (Fig.2.8a) indicated the presence of sp^2 hybridized carbons. The spectrum of the sample after ball milling (Fig.2.8b) showed the characteristic peak of the carbonaceous skeleton at 284.56 eV and the characteristic peaks of the oxygenated functional groups such as hydroxyl (285.55 eV), ether and epoxy (286.33 eV), and carbonyl/carboxyl (288.26 eV) groups. In the sample treated

Sample	C1s area [%]			
	C-C	C-O	C-O-O	O-C=O
G	81.09	19.9		
GO_{bm}	71.81	12.40	14.14	1.64
GO_{F32h}	59.20	28.24		12.56

Table 2.3: Binding Energy Values in C1s level from XPS analysis

with the photo-Fenton reaction (Fig.2.8c), a drastic decrease in the intensity of the epoxy peak and an increase in the intensity of the carboxylic acid peak were observed from the deconvolution of the C1s spectrum. This result was consistent with previous studies and was attributed to the fact that during the Fenton

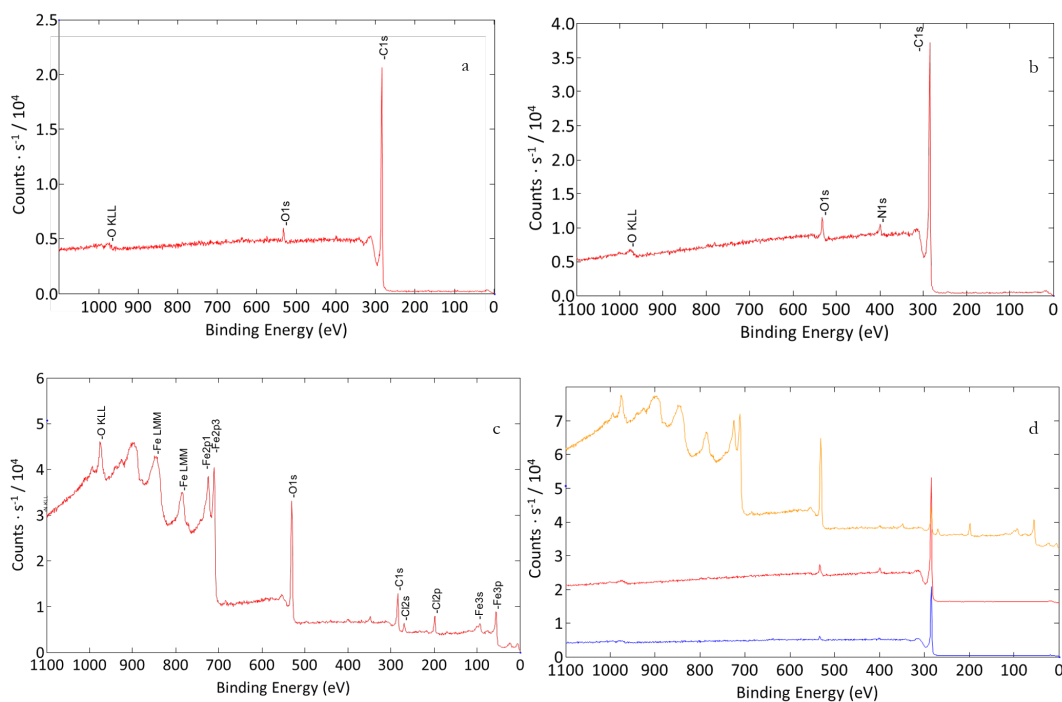


Figure 2.7: XPS Survey spectra of a) G; b) GO_{bm} , c) GO_{F32h} ; d) spectra overlap

reactions multiple C-C bonds are broken and the carbon atoms on the edges are contextually oxidized into COOH groups[44]. De-convoluted data for the O1s peaks are shown in the Supporting Information (Fig. 2.12, Table 2.5). The presence of oxygenated functional groups was further confirmed by Fourier-transform infrared spectroscopy (FTIR). As described in Fig. 2.9, the quantity and type of functional groups containing oxygen increases from graphite to GO_{bm} to GO_{F32h} . In the FTIR spectrum of ball milled GO, main absorption peaks were identified at 2980, 2887, 1381, 1157, 950 cm^{-1} attributable to stretching vibrations of the C-H sp^2 bonds, vibrations associated with defects in C-H sp^3 , symmetrical stretching vibrations of the oxidized graphite domains, C-O stretching vibrations (alkoxide and epoxide groups) respectively. The spectrum of the GO sample after the Fenton reaction instead showed the typical peaks of graphene oxide assigned, according to the literature, to the stretching vibrations of water molecules adsorbed on the surface of the material (3425 cm^{-1}), to C=O stretching vibrations of carbonyl and carboxylic compounds (1723 cm^{-1}), deformation vibrations of the -OH group (1381 cm^{-1}) and stretching vibrations

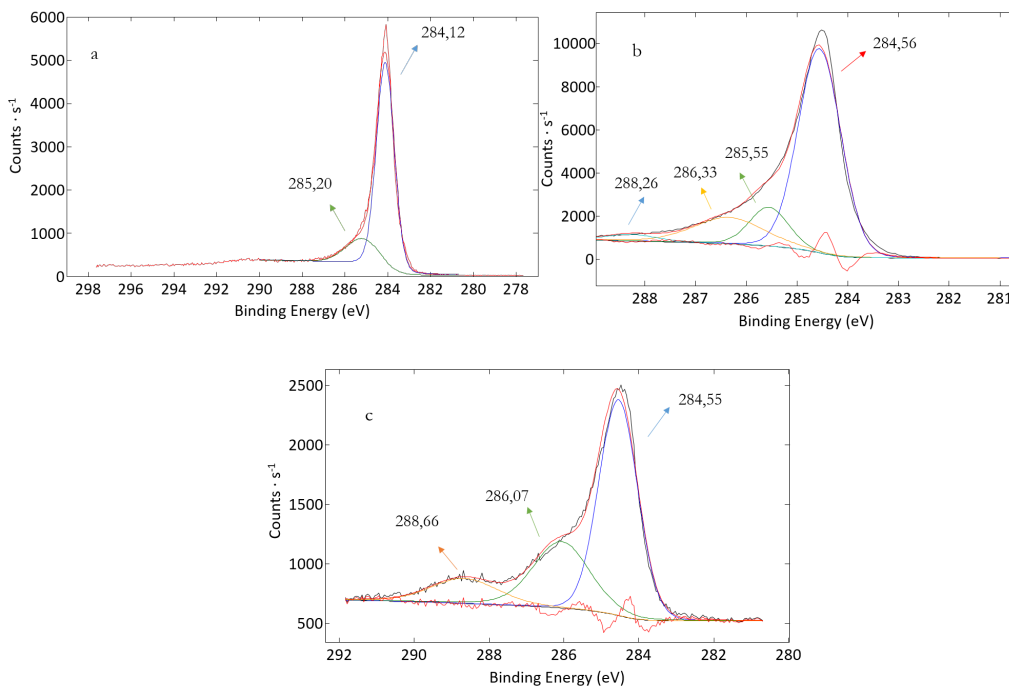


Figure 2.8: De-convoluted C1s core level XPS spectra for a) G; b) GO_{bm}, c) GO_{F32h}

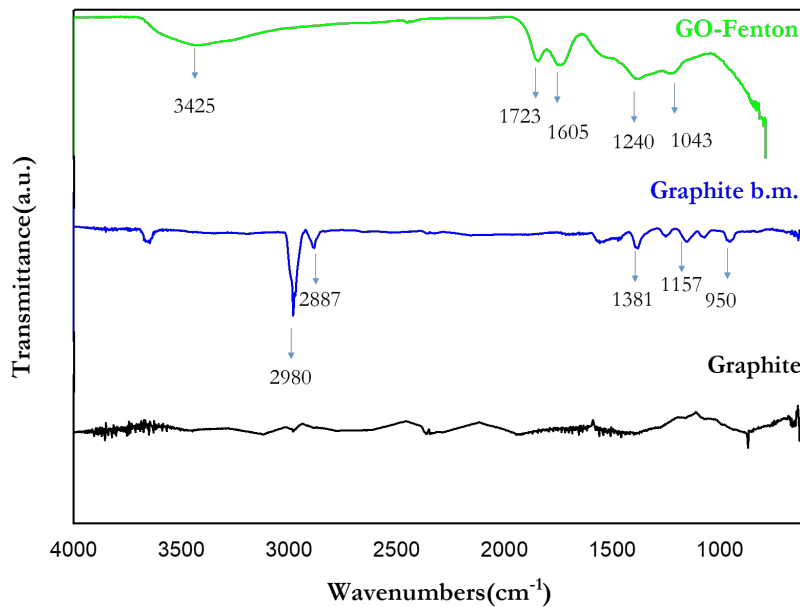


Figure 2.9: FTIR spectra of G; GO_{bm}, GO_{F32h}

of the CO groups alkoxide (950 cm^{-1}). The ζ potential measurements allowed to determine the stability of the samples in aqueous solution. The ζ potential values of GO_{bm} (-6.35 mV) and GO_{F32h} (-32.8 mV) were both negative (Fig. 2.10 (a,b)), due to the presence of the functional groups containing oxygen. The lower absolute value of the GO_{bm} ζ potential was due to the low degree of oxidation. The low degree of oxidation was also evidenced by the red shift of the UV-Vis absorption peak at 270 nm . Graphene oxide has a typical absorption peak at 230 nm due to electron $\pi-\pi^*$ transitions of the C-C and C = C bonds of the aromatic rings and a small shoulder at 300 nm relative to the $n-\pi^*$ transitions of the C = O bond [50]. The GO after the Fenton reaction showed the typical spectrum of graphene oxide (Fig.2.10c). The reduction of the lateral di-

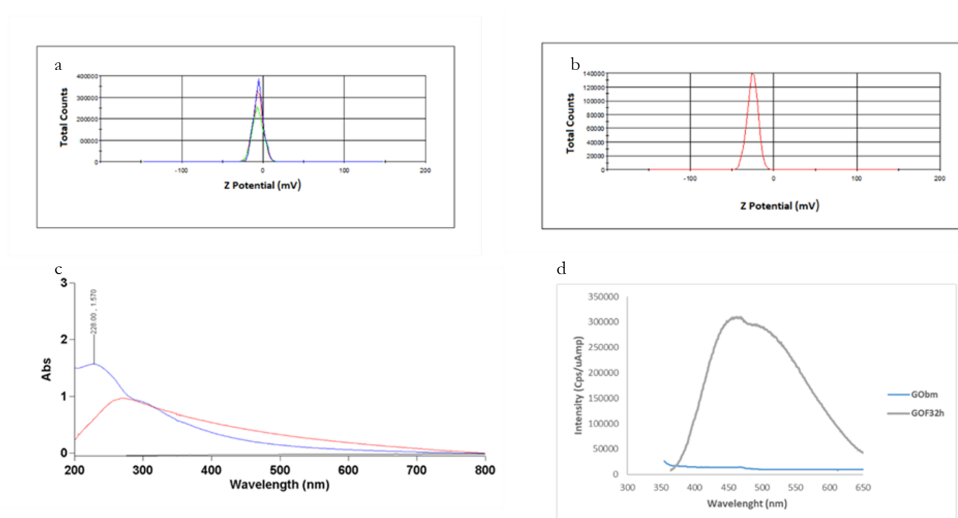


Figure 2.10: ζ potential values of GO_{bm} (a) and GO_{F32h} (b); UV-Vis absorption spectra GO_{bm} (red), GO_{F32h} (blue) (c); PL emission spectra λ_{EX} 335 nm (d)

mensions and the introduction of functional groups containing oxygen generate an energy bandgap which results in the emission of fluorescence from the material. Similarly to other carbon nanomaterials, the GO_{F32h} sample also exhibited a photoluminescent peak centered at 450 nm with excitation λ at 335 nm .

2.5 Conclusion

In this work we have found that the combination of ball milling and photo-Fenton reaction is an effective method to obtain graphene oxide without the use of acid media. Mechanical milling in dry conditions using only the oxygen contained in the jar as oxidizer allowed to obtain a material with good water solubility, as demonstrated by the negative value of the ζ potential, more exfoliated than graphite due to the shear forces produced by collisions between the balls and the material, and with smaller lateral dimensions, as demonstrated by the SEM and AFM images. From the XPS and FTIR analyses it was possible to observe that the sample, after ball milling, presented sp^2 hybridized carbon domains and sp^3 carbons linked to oxygenated functional groups, such as alcohols, epoxides, carboxylic acids and ketones. This material can be considered an ideal substrate for the photo-Fenton reaction. During the reaction, in fact, the $\cdot OH$ radicals generated by the dissociation of hydrogen peroxide photo-assisted by Fe^{3+} / Fe^{2+} act simultaneously by further oxidizing the oxygenated groups already present and adding to the unsaturated C-C bonds with the formation of -OH groups which can then be converted again to an higher oxidation state, as shown by the XPS analyses. The outcome of these processes is a material with nanometric dimensions around 30 nm, with a high degree of oxidation, excellent stability in water and optical properties similar to the nanometric carbon materials obtained from conventional graphene oxide. Although other studies are needed to increase yields and reduce reaction times by playing with the irradiation power during the Photo-Fenton reaction, we believe that this method can be considered as an eco-friendly alternative for the production of graphene oxide at the nanoscale.

2.6 Supporting Information

General Method	Specific Strategy	C/O ratio	Ref..
Wet Oxidation	Graphite was subjected to mechanical milling in presence of KMnO_4 and a lower quantity of sulfuric acid than the classical method (12 mL H_2SO_4 per gram of graphite). Dry ice was added to the jar to keep the T below 5°C .	1.73 determined from XPS analysis	[30]
Wet Oxidation	Milling was performed by mixing graphite flakes, with KMnO_4 in 5 mL of 87% H_2SO_4 per gram of graphite. The T was checked by opening the jar every 10min.	1.23 determined from Elemental analysis	[38]
Dry Oxidation	Ball milling was carried out in a planetary ball-mill machine in the presence of graphite, dry ice (2 eq.) and stainless steel balls	3.63 determined from Elemental analysis	[51]
Dry Oxidation	Graphite was mechanochemically treated in a planetary ball mill with KMnO_4	5.48 determined from Elemental analysis	[52]
Dry Oxidation	Milling was performed in a one-step without oxidants with different milling materials (steel and zirconia)	6.25 determined from XPS analysis	[37]

Table 2.4: Production methods of graphene oxide by ball milling

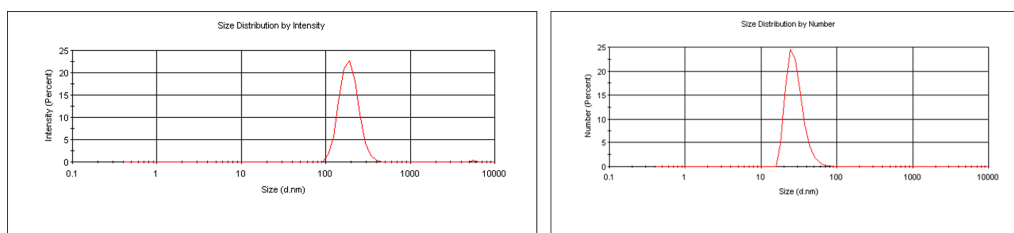


Figure 2.11: DLS Size distribution GO_{bm} (left) and GO_{F32h} (right)

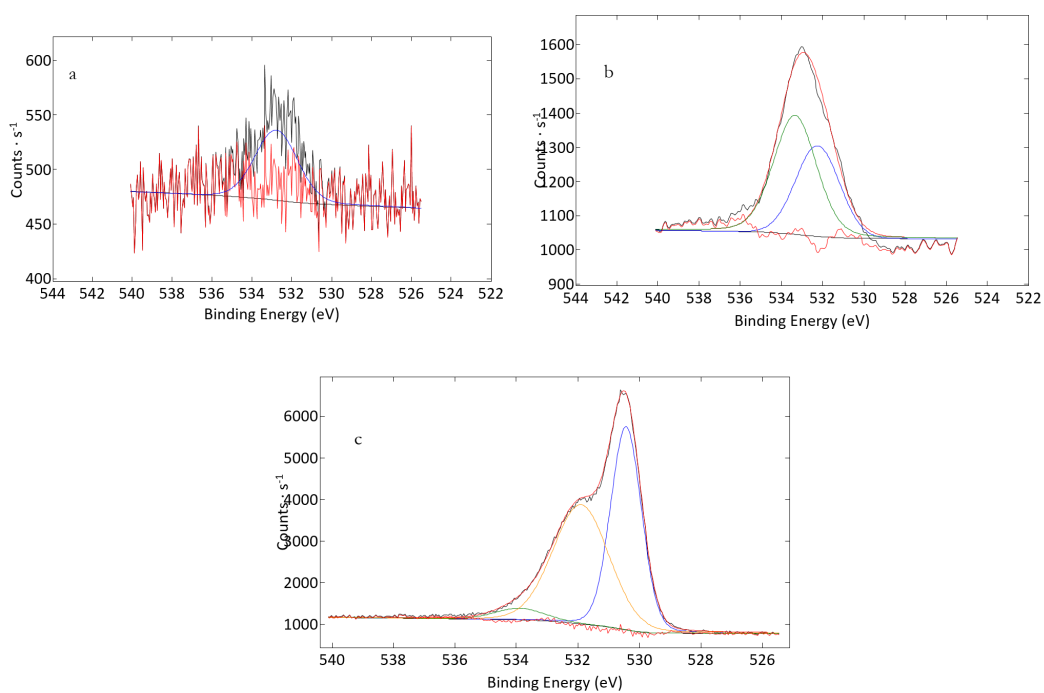


Figure 2.12: De-convoluted O1s core level XPS spectra for a) G, b) GO_{bm} , c) GO_{F32h}

Sample	C-O	C-OH
G		100
GO_{bm}	41.37	58.63
GO_{F32h}	46.02	49.50

Table 2.5: Binding Energy Values in O1s level from XPS analysis

References

- [1] Srinivasan M, Rajabi M, Mousa SA. Nanobiomaterials in cancer therapy; in *Nanobiomaterials in Cancer Therapy*. Elsevier 2016; p.57–89.
- [2] Ubbelohde AR, Lewis FA, Rice SA. Graphite and its crystal compounds; *Phys Today* 1961;14(3):66.
- [3] Franklin RE. ROLE OF WATER IN THE STRUCTURE OF GRAPHITIC ACID; *J Chim Phys Merged with Rev Gen Colloides* 1953;50.
- [4] Hofmann U, Holst R. Über die Säurenatur und die Methylierung von Graphitoxyd. *Berichte der Dtsch Chem Gesellschaft; A B Ser* 1939;72(4):754-71.
- [5] Ruess G. Über das graphitoxhydroxyd (graphitoxyd). *Monatshefte für Chemie und verwandte Teile anderer Wissenschaften*; 1947;76(3):381-417.
- [6] Sydlik SA, Swager TM. Functional graphenic materials via a Johnson-Claisen rearrangement; *Adv Funct Mater* 2013;23(15):1873-82.
- [7] Nakajima T, Matsuo Y. Formation process and structure of graphite oxide; *Carbon* 1994;32(3):469-75.
- [8] Lerf A, He H, Forster M, Klinowski J. Structure of graphite oxide revisited; *J Phys Chem B* 1998;102(23):4477-82.
- [9] Szabó T, Berkesi O, Forgó P, Josepovits K, Sanakis Y, Petridis D, et al. Evolution of surface functional groups in a series of progressively oxidized graphite oxides; *Chem Mater* 2006;18(11):2740-9.

- [10] Lerf A, He H, Riedl T, Forster M, Klinowski J. ^{13}C and ^1H MAS NMR studies of graphite oxide and its chemically modified derivatives; *Solid State Ionics* 1997;101:857-68.
- [11] Singh DP, Herrera CE, Singh B, Singh S, Singh RK, Kumar R. Graphene oxide: An efficient material and recent approach for biotechnological and biomedical applications; *Materials Science and Engineering C* 2018;86:173-97.
- [12] Bullo S, Buskaran K, Baby R, Dorniani D, Fakurazi S, Hussein MZ. Dual Drugs Anticancer Nanoformulation using Graphene Oxide-PEG as Nanocarrier for Protocatechuic Acid and Chlorogenic Acid; *Pharm Res* 2019;36(6):1-11.
- [13] Jume BH, Gabris MA, Nodeh HR, Rezanian S, Cho J. Biodiesel production from waste cooking oil using a novel heterogeneous catalyst based on graphene oxide doped metal oxide nanoparticles; *Renew Energy* 2020;162:2182-9.
- [14] Chen L, Moon J-H, Ma X, Zhang L, Chen Q, Chen L, et al. High performance graphene oxide nanofiltration membrane prepared by electro-spraying for wastewater purification; *Carbon* 2018;130:487-94.
- [15] Zhao J, Pei S, Ren W, Gao L, Cheng H-M. Efficient preparation of large-area graphene oxide sheets for transparent conductive films; *ACS Nano* 2010;4(9):5245-52.
- [16] Krishnamoorthy K, Veerapandian M, Yun K, Kim S-J. The chemical and structural analysis of graphene oxide with different degrees of oxidation; *Carbon* 2013;53:38-49.
- [17] Brodie BC. on the atomic weight of graphite; *Royal Society of London* 1858.
- [18] Pendolino F, Armata N, Masullo T, Cuttitta A. Temperature influence on the synthesis of pristine graphene oxide and graphite oxide; *Mater Chem Phys* 2015;164:71-7.

- [19] Huh S, Park J, Kim YS, Kim KS, Hong BH, Nam J-M. UV/ozone-oxidized large-scale graphene platform with large chemical enhancement in surface-enhanced Raman scattering; *ACS Nano* 2011;5(12):9799-806.
- [20] Cao J, He P, Mohammed MA, Zhao X, Young RJ, Derby B, et al. Two-step electrochemical intercalation and oxidation of graphite for the mass production of graphene oxide; *J Am Chem Soc* 2017;139(48):17446-56.
- [21] Hummers WS, Offeman RE. Preparation of Graphitic Oxide; in *J Am Chem Soc* 1958;80(6):1339.
- [22] Smith AT, LaChance AM, Zeng S, Liu B, Sun L. Synthesis, properties, and applications of graphene oxide/reduced graphene oxide and their nanocomposites; *Nano Mater Sci* 2019;1(1):31-47.
- [23] Marcano DC, Kosynkin D V., Berlin JM, Sinitskii A, Sun Z, Slesarev A, et al. Improved synthesis of graphene oxide; *ACS Nano* 2010;4(8):4806-14.
- [24] Kovtyukhova NI, Ollivier PJ, Martin BR, Mallouk TE, Chizhik SA, Buzaneva E V, et al. Layer-by-layer assembly of ultrathin composite films from micron-sized graphite oxide sheets and polycations; *Chem Mater* 1999;11(3):771-8.
- [25] Chen J, Chi F, Huang L, Zhang M, Yao B, Li Y, et al. Synthesis of graphene oxide sheets with controlled sizes from sieved graphite flakes; *Carbon* 2016;110:34-40.
- [26] Tufano I, Vecchione R, Netti PA. Methods to Scale Down Graphene Oxide Size and Size Implication in Anti-cancer Applications; *Front Bioeng Biotechnol* 2020;8:613280.
- [27] Ceriotti G, Romanchuk AY, Slesarev AS, Kalmykov SN. Rapid method for the purification of graphene oxide; *RSC Adv* 2015;5(62):50365-71.
- [28] Tiliakos A, Cucu A, Ceaus C, Trefilov AMI, Serban EC, Stamatini I. Graphite Oxide Post-Synthesis Processing Protocols; in *2nd CommScie International Conference Challenges for Sciences and Society in the Digital Era. International Journal of Science Communication* 2015; p.33–7.

- [29] Sun L. Structure and synthesis of graphene oxide; *Chinese J Chem Eng* 2019;27810):2251-60.
- [30] Luo D, Zhang F, Ren Z, Ren W, Yu L, Jiang L, et al. An improved method to synthesize nanoscale graphene oxide using much less acid; *Mater Today Phys* 2019;9:100097.
- [31] Xu Y-T, Guo Y, Li C, Zhou X-Y, Tucker MC, Fu X-Z, et al. Graphene oxide nano-sheets wrapped Cu₂O microspheres as improved performance anode materials for lithium ion batteries; *Nano Energy* 2015;11:38-47.
- [32] Gahlot S, Sharma PP, Gupta H, Kulshrestha V, Jha PK. Preparation of graphene oxide nano-composite ion-exchange membranes for desalination application; *RSC Adv* 2014;4(47):24662-70.
- [33] Sun X, Liu Z, Welsher K, Robinson JT, Goodwin A, Zaric S, et al. Nano-graphene oxide for cellular imaging and drug delivery; *Nano Res* 2008;1(3):203-12.
- [34] Benjamin JS. Dispersion strengthened superalloys by mechanical alloying; *Metall Trans* 1970;1(10):2943-51.
- [35] Piras CC, Fernández-Prieto S, De Borggraeve WM. Ball milling: A green technology for the preparation and functionalisation of nanocellulose derivatives; *Nanoscale Advances* 2019;1(3):937-47.
- [36] Zhu H, Cao Y, Zhang J, Zhang W, Xu Y, Guo J, et al. One-step preparation of graphene nanosheets via ball milling of graphite and the application in lithium-ion batteries; *J Mater Sci* 2016; 51(8):3675-83.
- [37] Mahmoud AED, Stolle A, Stelter M. Sustainable Synthesis of High-Surface-Area Graphite Oxide via Dry Ball Milling; *ACS Sustain Chem Eng* 2018;6(5):638-69.
- [38] Kralj M, Supina A, Čapeta D, Sović I, Halasz I. Mechanochemical oxidation of graphite for graphene-hydrogel applications: Pitfalls and benefits; *Materialia* 2020;14:100908.

- [39] Fenton HJH. LXXIII. Oxidation of tartaric acid in presence of iron; *J Chem Soc Trans* 1894;65:899-910.
- [40] Liu X, Sang Y, Yin H, Lin A, Guo Z, Liu Z. Progress in the mechanism and kinetics of Fenton reaction; *MOJ Ecol Environ Sci* 2018;3(1):10-5.
- [41] Bauer R, Fallmann H. The photo-Fenton oxidation-a cheap and efficient wastewater treatment method; *Res Chem Intermed* 1997;23(4):341-54.
- [42] Tahir MB, Farman S, Sagir M. Advances in Photocatalytic Materials for Waste Water Treatment Applications; 2022; p.759–67.
- [43] Bai H, Jiang W, Kotchey GP, Saidi WA, Bythell BJ, Jarvis JM, et al. Insight into the mechanism of graphene oxide degradation via the photo-Fenton reaction; *J Phys Chem C* 2014;118(19):10519-29.
- [44] Zhou X, Zhang Y, Wang C, Wu X, Yang Y, Zheng B, et al. Photo-Fenton reaction of graphene oxide: A new strategy to prepare graphene quantum dots for DNA cleavage; *ACS Nano* 2012;6(89):6592-99.
- [45] Dash P, Dash T, Rout TK, Sahu AK, Biswal SK, Mishra BK. Preparation of graphene oxide by dry planetary ball milling process from natural graphite; *RSC Adv* 2016;6(15):12657-68.
- [46] Pramanik N, Ranganathan S, Rao S, Suneet K, Jain S, Rangarajan A, et al. A Composite of Hyaluronic Acid-Modified Graphene Oxide and Iron Oxide Nanoparticles for Targeted Drug Delivery and Magnetothermal Therapy; *ACS Omega* 2019;4(5):9284-93.
- [47] Shen J, Hu Y, Shi M, Li N, Ma H, Ye M. One step synthesis of graphene oxide- magnetic nanoparticle composite; *J Phys Chem C* 2010;114(3):1498-503.
- [48] Jaleh B, Khalilipour A, Habibi S, Niyafar M, Nasrollahzadeh M. Synthesis, characterization, magnetic and catalytic properties of graphene oxide/Fe₃O₄.; *J Mater Sci Mater Electron* 2017;28(6):4974-83.

- [49] Johra FT, Lee J-W, Jung W-G. Facile and safe graphene preparation on solution based platform; *J Ind Eng Chem* 2014; 20(5:2883-7).
- [50] Lai Q, Zhu S, Luo X, Zou M, Huang S. Ultraviolet-visible spectroscopy of graphene oxides; *Aip Adv* 2012;2(3):32146.
- [51] Jeon I-Y, Shin Y-R, Sohn G-J, Choi H-J, Bae S-Y, Mahmood J, et al. Edge-carboxylated graphene nanosheets via ball milling; *Proc Natl Acad Sci* 2012;109(15):5588-93.
- [52] Posudievsky OY, Kozarenko OA, Khazieieva OA, Koshechko VG, Pokhodenko VD. Ultrasound-free preparation of graphene oxide from mechanochemically oxidized graphite; *J Mater Chem A* 2013;1(22:6658-63).

Chapter 3

Optimize nano-Graphene Oxide for biological applications

3.1 Abstract

Amino-functionalized nano-graphene oxide (GOQDs-NH₂) is prepared through a simple and eco-friendly oxidative cutting promoted by hydrogen peroxide and ammonia. Hyaluronic acid (HA) is covalently conjugated to GOQDS-NH₂ by the formation of amide bonds. The resulting HA-coated GO (GOQDs-HA) exhibits very low cytotoxicity to human dermal fibroblasts, HDFs and to non-transformed epithelial breast cells, MCF10A, and invasive breast adenocarcinoma cells MDA-MB-231 and thanks to the cell adhesion ability of HA it can be more effectively taken up by cells as compared to simple GO.

3.2 Introduction

In recent years, the biomedical applications of carbon-based materials have grown exponentially. Among these, Graphene Oxide (GO) has been extensively studied as a promising biomaterial in the field of biomedicine due to its unique properties such as scalable preparation, hydrophilicity, biocompatibility and biodegradability, high surface area, and large possibility of surface modification[1]. Generally, for biomedical applications such as drug delivery or cellular imaging, materials with uniform dimensions and in the nanometer range (below 100 nm) are highly desired. As is known, when the size of a material is reduced at the nanoscale, completely new properties can appear and / or the properties already known in the bulk can further enhance[2]. In the case of GO, when the two-dimensional structure of carbon atoms is reduced to nanometer size and atomic thickness (nano-GO or GOQDs), the specific surface area and chemical reactivity significantly increases. These properties are highly exploited to functionalize the surface of carbonaceous nanostructures through covalent and non-covalent bonds in order to improve their biocompatibility and regulate their functions in biological systems. Several pharmacologically active aromatic molecules were conjugated on the nano-GO surface resulting in drug delivery systems with high loading and controlled release capacity[3,4]. Similarly, the surface of nano-GO was functionalized through different types of surface coatings with targeting biopolymers, heteroatoms and targeting ligand

molecules to increase the biocompatibility and the ability to selectively recognize the target site[5-7]. It has also been verified that when reaching dimensions below 50 nm, the quantum confinement effects generate an energy band gap not present in graphene and large graphene oxide[8]. Consequently, nano-GO can show permanent photoluminescence, a particularly attractive property when considering applications in theranostics, which combines imaging and therapy[9]. Furthermore, the aromatic structure and the small size confer to the nano-GO the ability to absorb light in the near infrared range (700-900 nm). This property is particularly interesting for photo thermal therapy, a minimally invasive treatment based on the induction of cellular hyperthermia[10]. Nano-GO sheets, also called graphene oxide quantum dots (GOQDs) are obtained through two strategies, the bottom-up approaches involve the synthesis of GOQDs starting from molecular precursors[11], while the top-down methods involve obtaining GOQDs from the graphene oxide prepared with the classic, scalable wet oxidation of graphite, which, as it is known, consists of a mixture of sheets with different dimensions and thickness. The latter can be further divided into direct controllable synthesis methods, based on the cutting of GO through repeated oxidation steps or by varying the oxidation parameters or with physical promoters and post synthesis separation which consist in selectively separating the GO nanosheets from bulk through ultracentrifugation, separation gradient centrifuge, solvent flocculation[12]. Although the bottom-up methods allow precise control of the size of the final product, they are very complex and involve different chemical reactions. On the other hands, top-down approaches require long times, large amounts of oxidants and often result in low yields and poor dimensional control. In 2013, Jiang et al. report an environmentally friendly method for the preparation of amine-functionalized graphene quantum dots with diameters of 7.5 nm originating from graphene oxide sheets, hydrogen peroxide (H_2O_2) and ammonia (NH_3)[13]. In their method, the decomposition of hydrogen peroxide at 80 °C generates hydroxyl radicals ($\cdot OH$) that degrade and cut graphene oxide into small GOQDs, while ammonia passivates the active surface to give modified amino GOQDs. Compared to repeated oxidation cycles, the synergistic action of hydrogen peroxide and ammonia produces ecological by-products which is very promising, especially for

biomedical applications. The functionalization of GOQDs with amino groups is much explored both in the direction of improving the optical and electronic properties of nanomaterials, due to the strong interactions between the nitrogen atoms and the graphene network (orbital interactions between the lone pair of electrons of N with the HOMO and LUMO orbitals at GQDs allowing for a narrowing of the bandgap)[14], and in biological applications. An example of the utility of functionalized amino GOQDs (GO-NH₂) for biological applications is provided by the work of Sing and collaborators who have synthesized GO-NH₂ by activating the carboxylic acid groups of GO with thionyl chloride in dimethylformamide and subsequent reaction with sodium azide and have shown that it is a safer alternative for biomedical applications than oxygenated derivatives[15]. It is in fact known that GO, when administered intravenously in mice, can arouse a strong aggregation response in platelets on a scale comparable to that caused by thrombin, one of the most powerful physiological agonists of platelets, and triggers extensive pulmonary thromboembolism, consistent with the prothrombotic nature of this material[16]. Instead, *in vivo* and *in vitro* tests have shown, that the modified amino graphene oxide, is more biocompatible than GO, does not show a stimulating action towards platelets and does not induce pulmonary thromboembolism in mice. Furthermore, the NH₂ groups present on the surface and on the edges of GOQDs provide additional sites of surface functionalization. One of the most used functionalization to avoid cytotoxicity phenomena caused by inorganic nanomaterials is the surface coating with polymers such as polyethylene glycol[17], chitosan[18] and hyaluronic acid[19]. The solubility of GO in water and physiological media is improved by these surface-modified nanoparticles, which have improved stability and biocompatibility. The covering of the polymeric matrix protects cell membranes from harm caused by the sharp edges of GO when nanoparticles are introduced into the cells[20]. Hyaluronic acid (HA) is a naturally occurring, biocompatible, non-immunogenic, and biodegradable polysaccharide, consisting of alternating units of D-glucuronic acid and N-acetyl-D-glucosamine[21] with exceptional physicochemical properties, such as biodegradability, biocompatibility and no immunogenicity[22]. HA is found in abundance in the extracellular matrix, connective tissues, and body fluids, and it is involved in a vari-

ety of pathological processes[23]. Furthermore, HA is able to selectively recognize transmembrane glycoprotein CD44 receptors which are enormously expressed on the surface of tumor cells[24-25], so it has been widely used for active targeting in drug delivery systems. Herein, we used the oxidative cutting promoted by hydrogen peroxide and ammonia proposed by Jiang[13] et al, to obtain amino functionalized GO-QDs (GOQDs-NH₂) from graphene oxide obtained by wet chemical oxidation of graphite flakes. In order to verify their potential as theranostic systems able to combine targeted drug delivery with bioimaging, we have functionalized GOQDs-NH₂ with hyaluronic acid, a natural ligand of CD44 receptors. HA was covalently grafted on GO-QDs-NH₂ by carbodiimide coupling of the carboxylic acids on the HA chain and the amine groups on GOQDs. The photoluminescence of the obtained systems was used to investigate cell penetration in three types of cell lines, such human dermal fibroblasts, HDFs, non-transformed epithelial breast cells, MCF10A, and invasive breast adenocarcinoma cells MDA-MB-231 . Preliminary results on tissue penetration are also shown. In-vitro cellular cytotoxicity on HDF cells demonstrated the nontoxicity of the both GQDs-NH₂ and GQDs-HA nanocarriers. Curcumin a naturally occurring multifunctional polyphenolic phytoconstituent, was selected as a model hydrophobic drug to analyse the loading and release capacity of pharmacologically active molecules from the two systems. Curcumin was loaded on the surface of the QDs by exploiting the hydrophobic π/π interactions between the aromatic structure of Curcumin and the aromatic network of the QDs. The release of Curcumin was investigated from the surface of the QDs in acidic conditions and at high temperatures in order to simulate the acidic pH of tumor microenvironment and the cellular hyperthermia.

3.3 Methods

3.3.1 Materials

Graphite (flakes, +100 mesh), 30% sulphuric acid (H₂SO₄ 95-98% wt), potassium permanganate (KMnO₄) hydrogen peroxide (H₂O₂ 30% w/v), ammonium solution (28-30% w/v NH₃), N-hydroxysuccinimide (NHS), 1-(3-Dimethylaminopropyl)-

3-ethyl carbodiimide hydrochloride (EDC), Curcumin (from *Curcuma longa* Turmeric, powder), Rhodamine B isothiocyanate, minimum essential medium (MEM), fetal bovine serum (FBS), Eagle's minimal essential medium (EMEM), and 1% of penicillin/streptomycin were purchased from Sigma-Aldrich (Milano, Italy). Hyaluronic Acid 50 kDa was purchased from HAWORKS (Bedminster, NJ 07921 USA). 1% of L-glutamine was obtained from Lonza 17-605E, (Basel, Switzerland). 0.25% trypsin, 1 mM EDTA was purchased from Microtech, (Napoli, Italy). Dialysis membranes were purchased from Spectrum Laboratories Inc (New Brunswick, NJ). Amicon Ultra centrifugal filter units (3 kDa) were purchased from Merck Millipore (Milano, Italy). Polystyrene tissue culture flasks 150 cm² was obtained from Corning Inc., (Corning, NY). All of the reagents were used as received.

3.3.2 Instrumentation

Cryo-TEM analysis was performed using a Tecnai G2 F20 transmission electron microscope (FEI company, the Netherland) equipped with a Shotky field emission gun operating at an acceleration voltage of 200 kV and recorded at low dose with a 2k x 2k Ultrascan (Gatan, USA) CCD camera. Frozen hydrated samples were prepared by applying a 3 μ l aliquot to a previously glow discharged 200 mesh holey carbon grid (Ted Pella, USA). Before plunging into nitrogen cooled liquid ethane, the grid was blotted for 1.5 s in a chamber at 4 °C and 90% humidity using a FEI Vitrobot Mark IV (FEI Company, the Netherlands). Purity and surface chemical composition were determined by energy dispersive X-ray spectroscopy (EDX). 20 μ l of GOQDs-NH₂ or GOQDs-HA (1mg/mL) were deposited on a standard SEM pin stub and analysed by FESEM ULTRA-PLUS (Zeiss) (Milan, Italy) with the SE2 detector. Powder X-ray diffraction (XRD) patterns were collected on GO-QDs samples using a Philips PW1710 apparatus with CuK α 1 radiation. The scanning step size was 0.010° in 2 θ , and the time for each step was 1 s. Field emission scanning electron microscopy (SEM) micrographs were collected with a Zeiss Ultra Plus system. The thickness of the samples was measured on a mica surface by using a Multimode Nanoscope V scanning probe microscopy system (Bruker, USA) with AFM cantilever tips

with a force constant of ~ 50 N/m and resonance vibration frequency of ~ 350 kHz (Bruker, USA). The samples were prepared by solution casting of the aqueous suspensions of GO on a freshly cleaved mica surface and drying in air. The chemical information was revealed by X ray photoelectron spectroscopy (XPS) using a PHI5000VersaProbeII XPS spectrometer with a monochromatic Al-K- α source of 1486.68 eV. The high resolution C1s spectra were acquired at high power (100 W) with a Pass Energy of 23.5 eV, 0.1 eV step size, and averaged over 20 scans. Spectra from insulating samples were charged corrected by shifting all peaks to the adventitious carbon C1s spectral component binding energy set at 284.8 eV. Multipack software was used to process all the spectra. The Fourier transform infrared spectroscopy (FTIR) spectrum was recorded using a Nicolet iS50 spectrometer with the assistance of attenuated total reflectance. Raman spectra were recorded from powder at room temperature via a confocal Raman microscope (Jasco, NRS- 3100) with a 514 nm line of water-cooled Ar⁺ laser, 4mW at the sample. The ultraviolet-visible (UV/Vis) spectrum of the sample was measured using a Cary 5000 UV/Vis spectrophotometer. Photoluminescence spectra were obtained using a spectrophotometer LS55 (Perkin Elmer). The ζ potential in solution was detected using dynamic light scattering (DLS) instrument (Zetasizer zs nano series ZEN 3600, Malvern Instruments Ltd., Malvern, U.K., λ 632.8 nm). All the samples were diluted up to a droplet concentration of approximately 0.025 wt% by using milli-Q water. ζ -potential analysis was carried out by setting 50 runs for each measurement. Confocal fluorescence microscopy images were captured with a Leica TCS SP5. Images were acquired with a field of view $77.5 \times 77.5 \mu\text{m}$ for a pixel size of 76×76 nm and visualized by LAS-AF software (Leica-Microsystems, Mannheim, Germany). Fluorescence lifetimes (FLIM) were measured using a time-correlated single-photon-counting (TCSPC) technique, with a pulsed excitation source, NanoLed, at 559 nm (Horiba) and at an impulse repetition rate of 1 MHz at 90° to the R928 detector. DAS6 decay analysis software was used for raw data fitting and lifetime calculations.

3.3.3 Graphene Oxide Preparation

GO was prepared by the oxidation of natural graphite powder (325 mesh) according to the Hummers method with a modification of removing NaNO_3 from the reaction[26]. Typically, graphite powder (3.0 g) was added to concentrated H_2SO_4 (70 mL) under stirring in an ice bath. Under vigorous agitation, KMnO_4 (9.0 g) was added slowly to keep the temperature of the suspension lower than 20°C . Successively, the reaction system was transferred to an oil bath at 40°C and vigorously stirred for about 0.5 h. Then, 150 mL water was added, and the solution was stirred for 15 min at 95°C . Additional 500 mL water was added and followed by slow addition of 15 mL H_2O_2 (30%), turning the colour of the solution from dark brown to yellow. The mixture was filtered and washed with 1:10 v/v solution (250 mL) of concentrated HCl (37%wt) and water to remove metal ions. The resulting solid was dried in air and diluted to 600 mL, making a graphite oxide aqueous dispersion. Finally, it was purified by dialysis for one week using a dialysis membrane with a molecular weight cut off of 8000-14000 Da to remove the remaining metal species. The resultant graphite oxide aqueous dispersion was then diluted to 1.2 L, stirred overnight and sonicated (ultrasonic bath Falc Instruments) with a power of 20 W for 30 min to exfoliate it. The GO dispersion was then centrifuged at 8000 rpm for 40 min to remove the unexfoliated graphite and the wider GO sheets. The supernatant was kept and lyophilized for two days to give graphene oxide ($\text{GO}_{\text{Hummer}}$).

3.3.4 Amino-modified GOQDs Preparation

Amino-modified GOQDs (GOQDs-NH_2) were obtained through the oxidative cutting procedure promoted by hydrogen peroxide and ammonia reported in the literature with slight modifications. Briefly, in a 250 mL bottom flask, H_2O_2 (40 ml, 30%) was added to $\text{GO}_{\text{Hummer}}$ solution (3 ml, 8 mg/ml in H_2O) and the temperature was brought to 80°C under stirring in an oil bath. Afterward, ammonia (7 ml, 25-28%) was added dropwise to the mixture, over five hours which was accompanied by vigorous bubbling and heating up. After stirring for 8 h, under reflux, a clear homogenous yellowish-brown mixture was finally obtained with no detectable or precipitated GO remaining. After filtering the

as-prepared mixture through a 0.22 μm cellulose acetate membrane, the volume was reduced by evaporation under vacuum. The obtained solution was dialyzed for 2 days against deionized water (MWCO 100-500 Da), freeze-dried and stored at 4°C in the dark.

3.3.5 Conjugation of GOQDs-NH₂ with HA

An aqueous HA (1 w/v %) solution was prepared by dissolving the powder form of HA (0.10 g, 0.24 meq of COOH) in 10 mL DI water. The pH of the HA solution was adjusted to 4.5. EDC (0.45 g, 2.4 mmol) and NHS (0.14 g, 1.2 mmol) were added to the HA solution at 22°C. After stirring for 1 h, the GOQDs-NH₂ solution (0.10 g, 5 mL) was added to the HA solution, and the reaction mixture was continuously stirred overnight. The pH was adjusted to 8.9 to terminate the reaction. The unreacted species, and unconjugated GOQDs were removed from the reaction mixture through dialysis (MWCO 12,000-14,000) against DI water (three times), and the GOQDs-HA conjugated were finally recovered by lyophilisation as a brownish solid.

3.3.6 Curcumin Loading and Release

Curcumin (Cur) loaded GOQDs was prepared by a simple, noncovalent interaction method. Cur was dissolved in ethanol 66%v/v (4mg/mL) and was added drop by drop to the GOQDs-NH₂ and GOQDs-HA solutions (4mg/mL) in 1 h under stirring in the dark. After 1h, the products were transferred to a 2 mL Eppendorf and centrifuged at 1000 rpm for 10 min. The supernatants were kept and the precipitates were washed 3 times with phosphate buffer saline (PBS, pH 7.4) to remove free Cur molecules. The supernatants were combined and the amount of Cur present was calculated from a Cur calibration curve by measuring the absorbance at 425 nm. Then, the amount of loaded Cur (%l) was calculated based on the equation:

$$\%l = \frac{m_c - m_s}{m_{go}} * 100 \quad (3.1)$$

where m_c was the Cur initial mass, m_s was the Cur mass in the supernatants and m_{go} was the mass of GOQDs. The release of Cur from the two systems was

evaluated at pH 7.4 and pH 5.5 for 72 h; a release experiment was also performed at 60 °C for 5 min. Briefly, the precipitates containing Cur/GOQDs-NH₂ and Cur/GOQDs-HA were diluted with PBS buffer (pH 7.4 and 5.5) and incubated in the dark (at 37 °C or 60 °C) under continuous moderate shaking (140 rpm). At predetermined time intervals, the samples were collected and centrifuged at 4000 rpm for 15 min. The precipitates were dispersed in 1 mL of EtOH 66% v / v and the Absorbance was measured at 425 nm. The quantity of Cur present in the precipitates was obtained from the UV / Vis calibration curve of Cur. The percentage of Cur released (R%) was calculated from the equation:

$$R\% = \frac{m_2}{m_1} * 100 \quad (3.2)$$

where m_1 was the initial content of Cur and m_2 the amount of Cur released. All measurements were performed in triplicate, and the percentage of cumulative release (R%) was plotted as a function of time.

3.3.7 Cell culture

Experiments were performed on human dermal fibroblasts, HDFs and on non-transformed epithelial breast cells, MCF10A, and invasive breast adenocarcinoma cells MDA-MB-231. HDFs were extracted from healthy breast biopsies. MCF10A were grown in DMEM/F12 (Gibco) with 5% horse serum, 1% L-glutamine and 1% of penicillin/streptomycin, freshly supplemented with insulin (Sigma-Aldrich), EGF (Peprotech) and hydrocortisone (Sigma-Aldrich). MDA-MB-231 were grown in DMEM/F12 (Gibco) with 10% fetal bovine serum (FBS), 1% L-glutamine and 1% of penicillin/streptomycin. HDFs line was grown in enriched minimum essential medium (MEM) Eagle composed of MEM, 10% and 20% of fetal bovine serum (FBS) respectively, 1% of L-glutamine, and 1% of penicillin/streptomycin. The medium was changed every 2 days until reaching 90% confluence. Cells were washed three times with PBS and incubated with trypsin-ethylenediaminetetraacetic acid (EDTA) (0.25% trypsin, 1 mM EDTA) for 5 min at 37 °C to detach the cells.

Calibration Curve for GOQDs-NH₂, GOQDs-HA and cells

The standard calibration curves for the two systems (GOQDs-NH₂ and GOQDs-HA) were obtained by measuring their fluorescence intensity at different and known concentration by a LS55 spectrofluorimeter (Perkin Elmer) at 370 nm excitation and 500 nm emission wavelengths. The standard calibration curves for MCF10A, MDA-MB-231 and HDFs cells were obtained by culturing varying and known cell numbers of cells in a 24 well plate. Cells were allowed to adhere for 6 h at 37 °C and then incubated with 1 ml of 1 µg/ml nuclear dye Hoechst 33342 (Invitrogen) for 20 minutes. After incubation, cells were rinsed once to remove non-internalized Hoechst and incubated with 0.5 ml of ddH₂O at 37 °C for 1 h. The samples were then transferred to a -80 °C condition for 30 min and again to 37°C for 30 min. At this point, cells inflated by water were lysed with 0.5 ml of solution including 2x TNE buffer (10x TNE buffer: 100 mM Tris, 10 mM EDTA, 1.0 M NaCl, pH 7.4). Then, the samples were measured at 350 nm excitation and 500 nm emission wavelengths.

Quantification of GOQDs-NH₂, GOQDs-HA internalization

To quantify the number of internalized nanoparticles (NPs), MCF10A, MDA-MB-231 and HDFs cells were cultured at a density of 40000 cells/well in 24 well plates. 24 h after cell seeding, cells were incubated for 24 h at 37 °C with GOQDs-NH₂ and GOQDs-HA dispersed in cell culture medium at a final concentration of 0.01 mg/ml. For each NPs system cells were cultured in 6 different wells, three of which were used for the quantification of NPs internalization and three for cell counting. After incubation, cells were rinsed five times with PBS to remove non-internalized NPs and three wells were incubated with 1 ml of 1 µg/ml nuclear dye Hoechst 33342 (Invitrogen) for 20 min. Then, the lysis protocol described in the previous subparagraph was applied and cell lysates not stained with Hoechst dye were analyzed at the wavelengths of the corresponding NPs systems, the cell lysates stained with Hoechst at 350 nm excitation and 500 nm emission wavelengths. Fluorescence intensity values were interpolated with the NP and cell calibration curves and normalized to the recovered cell number to obtain the number of internalized NPs per cell.

Co-localization with lysosomes

After 24 h incubation with GOQDs-HA-Rhod, HDFs were rinsed twice with PBS to remove non-internalized NPs and fixed with 4% paraformaldehyde at RT. Then, cells were permeabilized and blocked with 0.1% saponin-5% bovine serum albumin (BSA)-PBS for 1h at RT. Mouse anti-LAMP 2 polyclonal primary antibodies and, with AlexaFluor 488, goat anti-mouse secondary antibodies (Molecular Probes, Invitrogen) were used to localize the lysosomes. All samples were finally observed at a confocal microscope (SP5 Leica) with a 63x oil immersion objective. The co-localization analysis was performed by JACoP plugin[27] to have an estimate of the overlap coefficient among the pixels in the dual-channel images.

3.3.8 GOQDs-NH₂ and GOQDs-HA 3D Dermis Microtissue (HDF μ TPs) internalization

GOQDs-Rhodamine B labelling

To understand the uptake of GOQDs-NH₂ and GOQDs-HA by HDF μ TPs, Rhodamine B (Rhod B) was used to label GOQDs by physical adsorption. An absorption peak appears at ~575nm, characteristic of Rhod.B, in the UV/Vis spectra, which suggests binding of Rho B to GOQDs-NH₂ and GOQDs-HA. 158.8 μ L of Rho B solution, (1mg/mL in H₂O) was added to 3.58 mL of GOQDs (0.85 mg/mL in H₂O). After stirring for 24 h at T room in the dark, the excess of RhoB was washed by dialysis against water for 2 days in the dark. The amount of physio absorbed RhoB was determined from a UV-Vis calibration curve of Rhod.B at 557 nm.

3D Dermis Microtissue (HDF μ TPs) production

Normal mammary Fibroblasts (NF) extracted by biopsies of healthy patients, were sub-cultured onto 150 mm Petri dishes in Eagle's minimal essential medium (EMEM) with high glucose, containing 10% fetal bovine serum, 100 mg/ml L-glutamine, 100 U/ml penicillin / streptomycin. Microscaffolds composed by porous gelatine microspheres (diameter 75-150 μ m) were produced at 5% w/w

of crosslinkage[28]. Before using, dry microcaffolds were sterilized in absolute ethanol for 24 h on a rotating plate. Then, microcaffolds were washed twice in sterile phosphate-buffered saline (PBS) without calcium and magnesium solution. Finally, before cell seeding, PBS was replaced with fresh culture medium. Spinner flask bioreactors were used to fabricate three dimensional Micro Tissue Precursors (3D- μ TP). For 3D- μ TP production three dynamic spinner cultures were performed by seeding NF on gelatine porous microcarriers (GPMs). For each spinner culture, 50 mg of microcaffolds were loaded together with 7.5×10^5 cells corresponding to an initial ratio of 20 cells/microcaffold NF cell line. To help cell seeding on microcaffolds an intermittent stirring regime (30 min at 0 rpm, 5 min at 30 rpm) for 6 h was performed. Then, dynamic cultures were kept under continuous stirring at 30 rpm for up to 12 days. Medium was changed on the first day and every 3 days until the end of the experiments. From day 2, ascorbic acid at a final concentration of 50 mg/ml was added to each spinner culture, containing NF cells, in order to enhance the synthesis and secretion of collagen by fibroblasts. At day 7 of culture, the microtissue were distributed in two 96-well round bottom clear Ultra-Low Attachment Multiple Well Plates (Corning Costar) and placed on the Orbital Shaker (ITATM) at 37°C in a humidified 5% CO_2 with GOQDs-HA dispersed in cell culture medium at a final concentration of 0.1 mg/ml and 0.001 mg/ml. At three different time points: 24h, 48h and 72h, the microtissues were washed with PBS and fixed with Paraformaldehyde 4% (PAF 4%).

3.4 Results and Discussion

3.4.1 Amino-modified GOQDs Preparation

Amino functionalized GOQDs (GOQDs- NH_2) were obtained starting from graphene oxide ($\text{GO}_{\text{Hummer}}$) prepared with Hummer's methods, following a procedure reported in the literature[13] with slight modifications. This method involves the synergistic effect of hydrogen peroxide (H_2O_2) in oxidizing and cutting the GO into small pieces and ammonia (NH_3) in functionalizing the as formed GO nanosheets. In contrast with conventional solvents and oxidants which are not

environmentally friendly, H_2O_2 produces green by-products of O_2 and H_2O , and, if the pristine GO has been sufficiently purified from the metallic impurities coming from the oxidation process, this procedure is highly promising for biomedical applications[29]. In a typical procedure, 40 ml of H_2O_2 was added to a homogenous aqueous dispersion of GO (3 ml, 8 mg/ml). When the T reached 80°C , 7 mL of an ammonia solution was added dropwise to the solution over 5 h. Vigorous bubbling and an increase in T up to 105°C were observed upon addition of ammonia. Before the next addition, the reaction T was expected to stabilize again at 80°C . During the reactions the colour of the solution gradually changed from dark brown to yellow, frames of the reaction progress are shown in Fig.3.16 in Supporting Information. In literature it is reported that the formation of GOQDs- NH_2 under these conditions from the GO obtained with the Hummer method occurs in 24 h at 80°C . We decided to monitor the progress of the reaction by fluorescence measurements. As already described, in fact, the reduction of carbonaceous materials to the nanometric scale results in the origination of photoluminescence. We observed that the fluorescence intensity upon excitation at 350 nm gradually increased over time until it reached a maximum after 8 h and then rapidly decreased until it was no detectable after 18 h. So we completed the experiment after 8 h. The product was brought to room T, filtered through a $0.22\ \mu\text{m}$ cellulose acetate membrane, dialyzed for 2 days against deionized water and freeze-dried to get GOQDs- NH_2 (41.8% yield). After redispersion in H_2O , the GOQDs- NH_2 formed a very stable clear solution with no visible precipitation or aggregation phenomena (Fig.3.16 Supporting Information).

3.4.2 Conjugation of GOQDs- NH_2 with HA

The GOQDs- NH_2 obtained were conjugated with HA to increase their biocompatibility and to provide them the ability to selectively recognize cells with CD44 receptors. To create amide bonds between the carboxylic groups of HA and the amine groups of GOQDs- NH_2 , an EDC/NHS coupling technique was used. EDC activates the carboxyl groups of HA, allowing them to form amide bonds with the primary amines of GOQDs- NH_2 . The carboxylic acid attacks EDC un-

der acidic conditions, forming an O-acylisourea intermediate that is extremely reactive and short-lived in an aqueous environment. NHS improve the stability of the activated ester and thus increase product yield while reducing side effects. Due to the presence of both amino and carboxyl groups in GOQDs-NH₂, amide bonds can be formed between two GOQDs-NH₂[29] To reduce GOQDs-NH₂ cross-linking, the carboxylic activators EDC and NHS were first reacted with HA for 1 h before adding GOQDs-NH₂. The unreacted species and unconjugated GOQDs were removed from the reaction mixture through dialysis (MWCO 12,000-14,000) against DI water (three times), and the GOQDs-HA conjugated were finally recovered by lyophilisation as a brownish solid (78% yield).

3.4.3 Morphological Characterization and Size Evaluation

Fig. 3.1a,b,c show TEM and Cryo-TEM images of the GO_{Hummer}, GOQDs-NH₂ and GOQDs-HA respectively (Fig. 3.1a,b,c). GO_{Hummer} sheets had a quasi-hexagonal shape with dark regions due to the presence of multiple layers of graphene stacked on top of each other (Fig.3.1a). The centrifugation step at 8000 rpm effectively allowed to separate the smaller size GO sheets from the bulk containing larger particles. In fact, the sample showed a size distribution between 10 and 80 nm with average lateral dimensions around 35-40 nm. After oxidative cutting, the reduction of the lateral dimensions was evident, the GOQDs-NH₂ nanosheets assumed an almost circular shape with lateral size around 12 nm (Fig.3.1b). The transparent regions indicated the exfoliation of the nanoparticles in single or few layers of graphene. After conjugation with HA, the nanosheets retained more or less the lateral dimensions and transparencies, but became more irregular in shape and showed a tendency to give phenomena of aggregation (Fig.3.1c) due to the wrapping and folding of GOQDs by HA[30]. Energy dispersive X-ray spectroscopy (EDX) measurements were performed to analyse the relative elemental composition on the surface and to verify the degree of purity of the samples obtained. As shown in Fig. 3.2a, GO_{Hummer} was free of impurities from potassium permanganate and sulfuric acid used for oxidation. The degree of oxidation of the prepared GO_{Hummer} can be estimated from C/O ratio. Optimally oxidized graphene oxide C/O weight

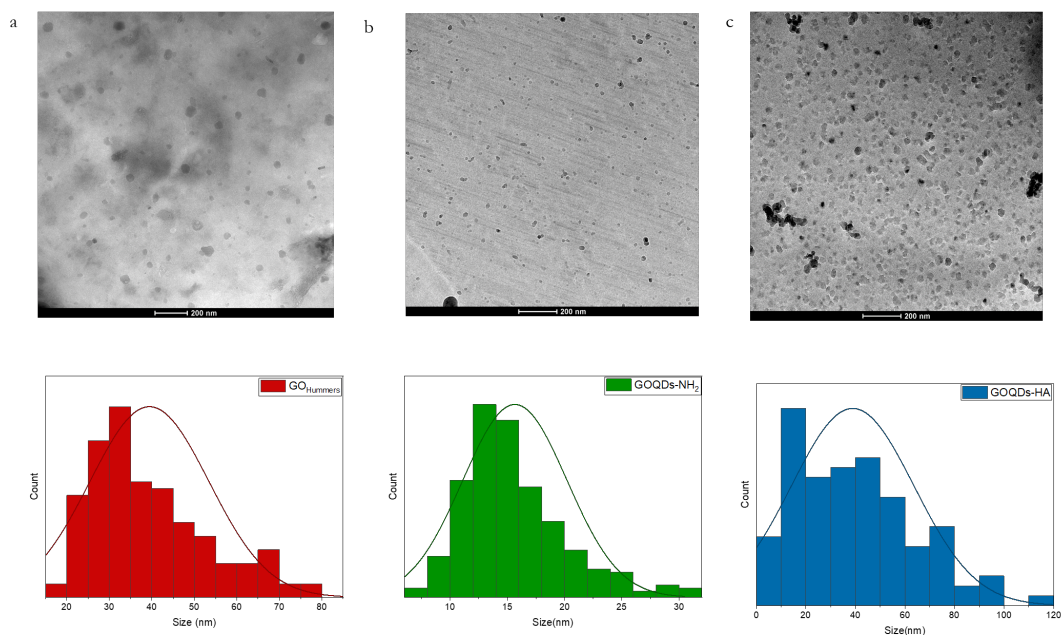


Figure 3.1: TEM image and Size Distribution GO_{Hummer} (a), Cryo-TEM image and Size Distribution $GOQDs-NH_2$ (b) and $GOQDs-HA$ (c)

ratio lies between 2.1 to 2.9[31]. The samples of GO prepared in this work exhibited a C/O weight ratio of 2.15, consistent with the range reported for well-oxidized graphene. After the oxidative cutting (Fig. 3.2b,c), the degree of oxidation of the sample increased and in the elemental analysis the nitrogen due to the amine functionalization appeared. The peak at 1.5 keV was due to the gold sputter coating of the samples. Atomic force microscopy (AFM) imaging confirmed the decrease in lateral dimensions (Fig. 3.3). As expected from the Cryo-Tem images, the average thickness of the GO_{Hummer} nanosheets was around 5 nm corresponding to different layers of graphene (Fig. 3.3a), while in the samples subjected to oxidative cutting and functionalized with HA, the thickness was around 1 nm corresponding to the thickness of a monolayer of graphene (Fig. 3.3b,c). The structural properties of samples can be elucidated via Raman spectroscopy. The Raman spectra at low and high frequencies of the graphite and of the samples obtained were shown in Fig. 3.4a. In the Raman spectrum of pristine graphite, the G band was present at 1583 cm^{-1} and the 2D band at 2728 cm^{-1} . The first band is due to the vibrations in the plane of the aromatic

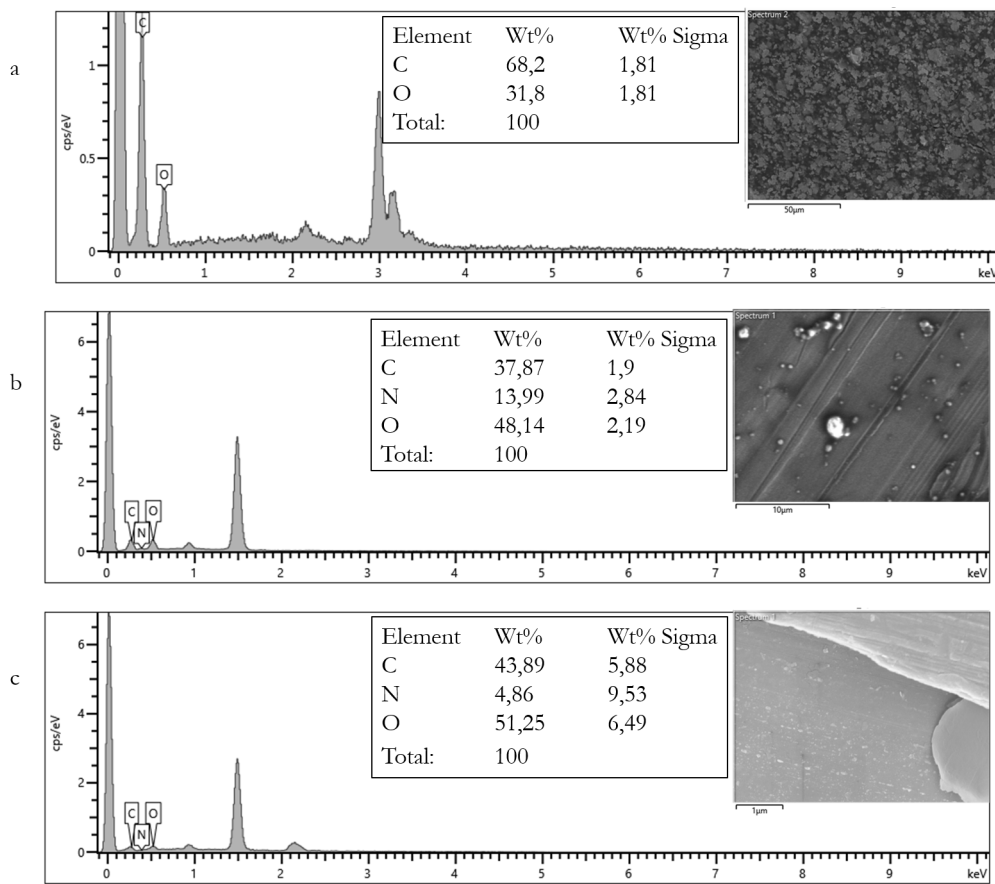


Figure 3.2: EDX spectra of a) GO_{Hummer} ; b) $GOQDs-NH_2$; c) $GOQDs-HA$

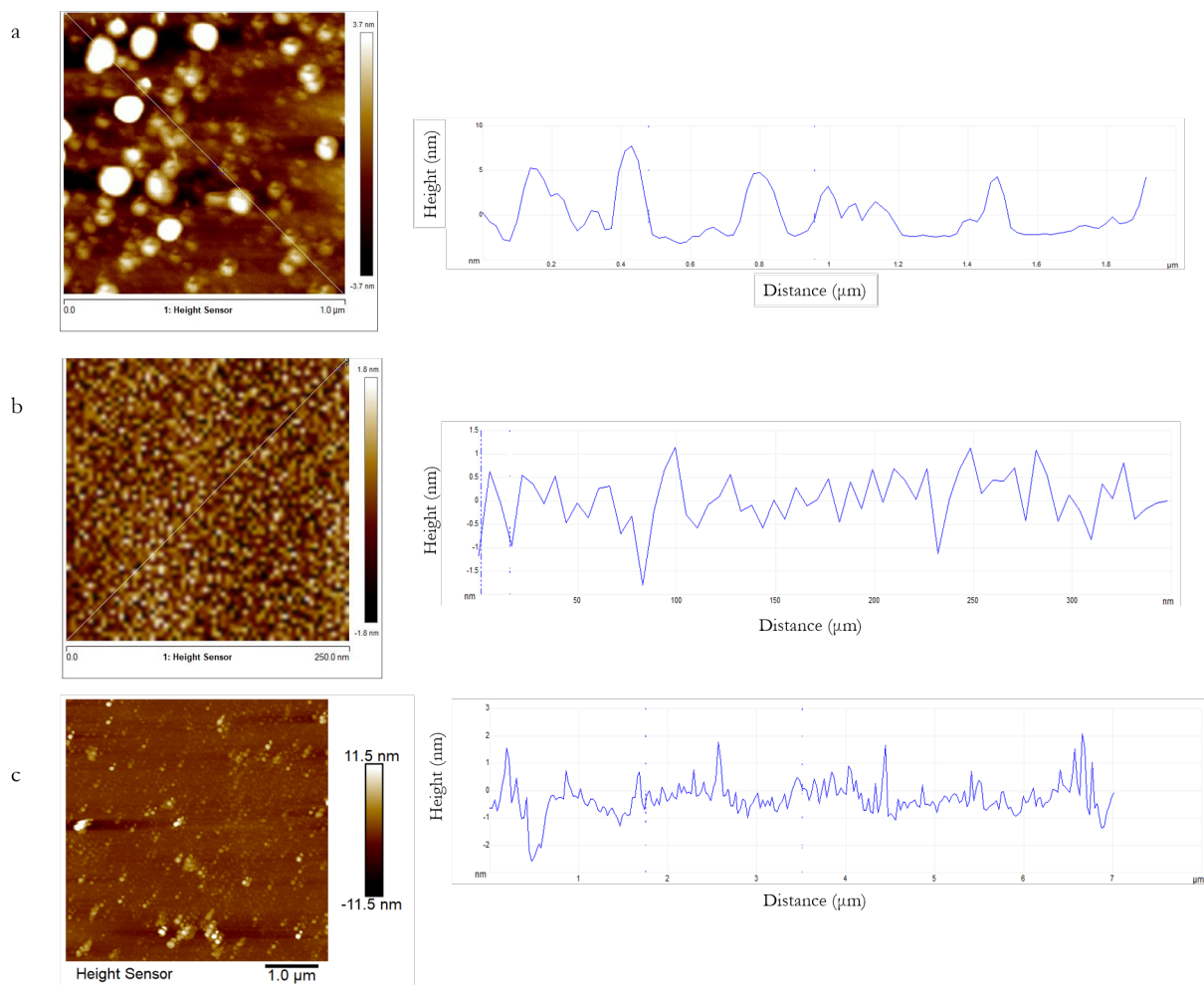


Figure 3.3: AFM Images (left) and height profile of the AFM images (right) of a) GO_{Hummer} ; b) $GOQDs-NH_2$; c) $GOQDs-HA$

structure of Csp^2 , while the last is related to the stacking order of the graphite. When the graphite periodic lattice is perturbed by defects (functional groups, holes or vacancies), the shape of the bands changes and new forbidden Raman bands appear. In the low-frequency Raman spectrum of the GO obtained by the Hummer method, the G band broadens significantly and displays a shift to higher frequencies (1600.49 cm^{-1}), and a new band at 1350.89 cm^{-1} (D band) appeared. The blue shift of G band was associated with the formation of new sp^3 hybridized C atoms and therefore with the increase in the degree of oxidation. At high frequencies, the 2D (2728 cm^{-1}) band decreased in intensity and two new bands appeared at 2703.42 cm^{-1} (2D band), the D band overtone and at 2932.52 cm^{-1} , known as the D+G combination band activated by the presence of defects. The Raman spectrum of GOQDs-NH₂ has very similar charac-

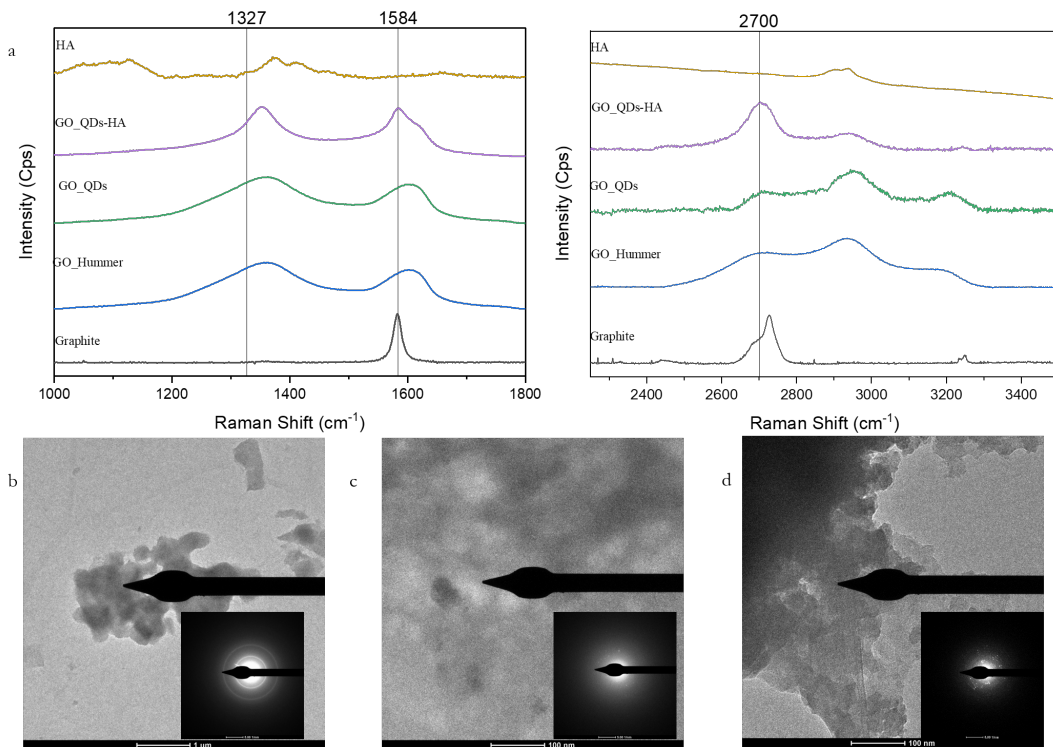


Figure 3.4: a) Low (left) and high (right) Frequency Raman spectra of GO_{Hummer} ; $GOQDs-NH_2$; $GOQDs-HA$; b,c,d) SAED pattern of GO_{Hummer} ; $GOQDs-NH_2$; $GOQDs-HA$

teristics to GO_{Hummer} . Table 3.1 reported the position, the total width at half

height, the intensity and the relationships between the intensities of the main Raman bands. The ratio between the intensities of the D and G bands (I_D/I_G) provides indications on structural defects. This ratio was zero in graphite, for the absence of structural defects, increased in GO_{Hummer} due to reduction in size and increase in oxygenated functional groups and reached 1.14 in GOQDs-NH₂. Curiously, in the Raman spectrum of GOQDs-HA, the G band (1586,99 cm⁻¹) returned to the position of the G band in graphite and presented a small shoulder (D' band) indicative of the presence of a few layers of graphene. Furthermore, the D+G band (2927,85 cm⁻¹) becomes less pronounced, indicating a lower amorphization of the material. This type of behaviour had already been observed for single graphene sheets obtained by thermal expansion of graphite oxide and was defined graphitic self-healing and was attribute to recombination of mobile carbon atoms with vacancies[32]. As previously described, high T is reached during oxidative cutting, so a similar defect repair phenomenon is likely to occur. However, it remains to be clarified why this mechanism is not visible in GOQDs-NH₂ and becomes relevant after HA coating. Fig. 3.4b,c and d showed the selected area electron diffraction (SAED) patterns for GO-Hummers GOQDs-NH₂ and GOQDs-HA. The obtained SAED data showed both GOQDs-NH₂ and GOQDs-HA possessed clear diffraction spots with sixth-order symmetry and tiny brighter spots due to GO crumpled regions[33]. These observations may be in agreement with the previously hypothesized mechanism, but further studies are needed to verify the role of HA in this process.

	G	GO_{Hummer}	GOQDs-NH₂	GOQDs-HA
G	1583.79	1600.49	1604.04	1586.99
D		1350.89	1364.14	1352.99
FWHM_G	16.6397	76.2965	77.1671	62.0691
FWHM_D		94.8292	88.3177	59.9558
I_D/I_G		0.91236	1.14664	0.99916
2D	2728.55	2703.42	2715.82	2702.05
D+G		2932.52	2934.12	2927.85
2G			3170.12	3202.45

Table 3.1: Raman parameters for G, GO_{Hummer} , GOQDs-NH₂ and GOQDs-HA

3.4.4 Product Composition

X-ray photoelectron spectroscopy (XPS) was used to investigate the degree of oxidation of the products obtained, the composition and nature of the oxygenated functional groups present. XPS survey spectra for pristine graphite (G), GO_{Hummer} , $GOQDs-NH_2$; $GOQDs-HA$ are reported in Fig. 3.5. For pristine graphite, the minor O1s peak was due to small amounts of physisorbed oxygen (Fig.3.5a). In the GO_{Hummer} an increase in oxygen concentration, along with a reduction in the carbon content, was observed (Fig. 3.5 b). After the oxidative cutting, the oxygen content increased up to 45% indicating the effective oxidation of the sample and the presence of N-related peaks was observed (Fig 3.5c). In the case of $GO-HA$ (Fig. 3.5d), the pristine spectrum showed similar peaks to $GOQDs-NH_2$. Table 3.2 shows the atomic concentrations of C1s and O1s and N1s and their ratios for the four samples. In or-

Sample	C1s(%)	O1s(%)	N1s(%)	O/C
G	95.02	4.98		5.24
GO_{Hummer}	79.3	17.0		21.4
$GOQDs-NH_2$	43.4	45.1	5.2	103.9
$GOQDs-HA$	51.0	23.7	13.9	46.5

Table 3.2: Binding Energy Values in C1s level from XPS analysis

der to identify the oxygen-containing functional groups that form on the edges and basal planes of the carbonaceous lattice after the two processes, the high resolution C1s core level spectra of all the sample were deconvoluted into different binding energies (B.E.) (Fig.3.6) as summarized in Table 3.3. The C1s spectrum of GO_{Hummer} (Fig.3.6a) showed the characteristic peak of the carbonaceous skeleton at 284.57 eV and the characteristic peaks of the oxygenated functional groups such as ether and epoxy (286.43 eV) and carbonyl/carboxyl (288.44 eV) groups. In the sample treated with the oxidative cutting (Fig. 3.6b) four types of carbon atoms could be detected in the C1s high resolution spectrum: graphitic C-C and C=C (284,55 eV) C-O functions (286,11 eV) and C=O and COOH groups (288,55 eV and 289.98 eV). However, the latter two functions may be present in $GOQDs-NH_2$ due to the weak energy difference be-

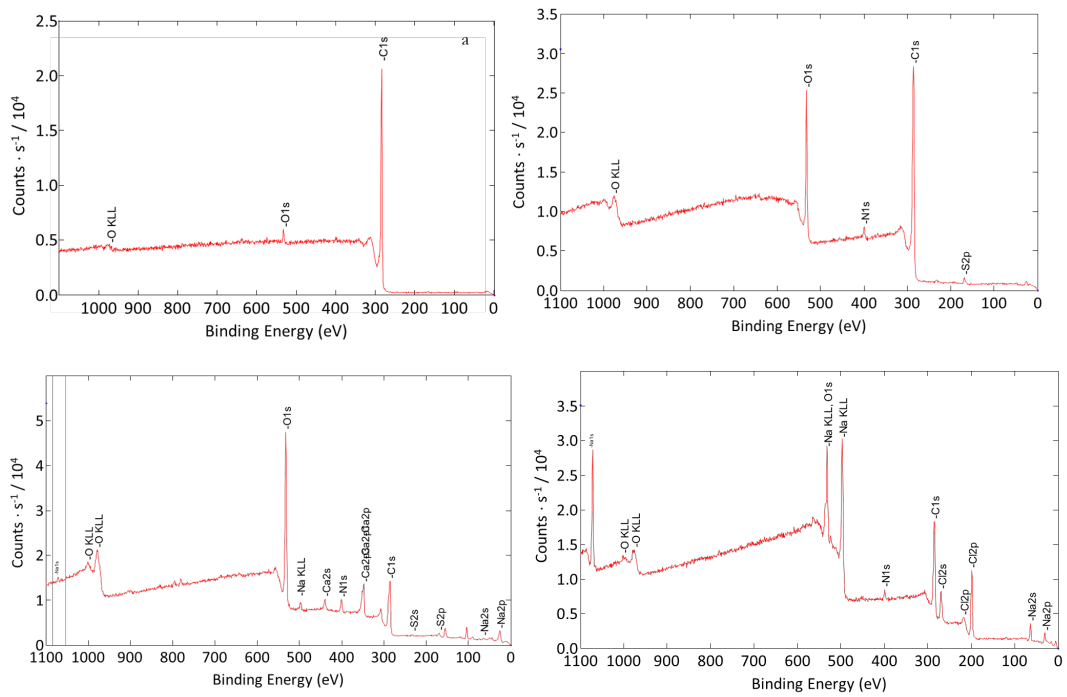


Figure 3.5: XPS survey spectra of a) graphite; b) GO_{Hummer}; c) GOQDs-NH₂; d) GOQDs-HA

tween C-C or C=C and C-N or C=N functions. Similar peaks were observed in GOQDs-HA (Fig.3.6c). De-convoluted data for the O1s peaks are shown in

Sample	C1s area [%]			
	C-C	C-O	C-O-O	O-C=O
GO_{Hummer}	49.92		43.45	6.63
GOQDs-NH₂	44.20	21.86	27.77	6.18
GOQDs-HA	37.67	45.32	12.95	4.06

Table 3.3: Binding Energy Values in C1s level from XPS analysis

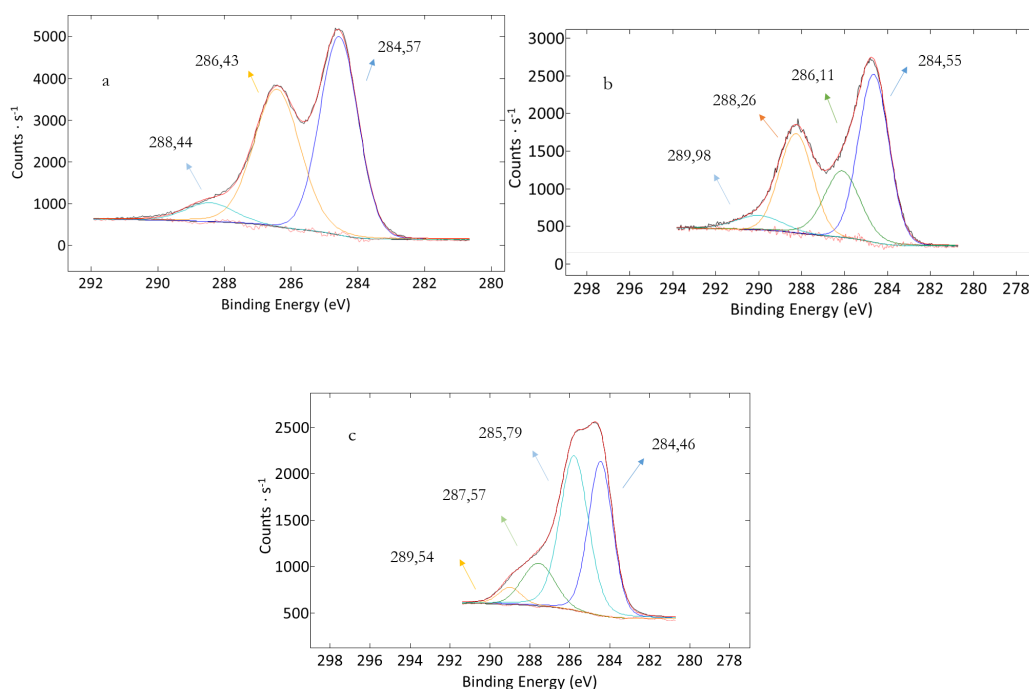


Figure 3.6: De-convoluted C1s core level XPS spectra for a) GO_{Hummer}; b) GOQDs-NH₂; c) GOQDs-HA

the SI (Fig.3.17, 3.18 Table 3.4, 3.5). Two N1s signals located at 398,99 eV (C-N and C=N) bonds and at 400,50 eV (protonated NH₃⁺ functions linked to carbon atoms), in N1s spectrum of GOQDs-NH₂ further confirmed the covalent anchorage of NH₃ at the surface of GOQDs. The presence of oxygenated functional groups was also evidenced by ζ potential measurements, GO_{Hummer} (-36.5 mV), GOQDs-NH₂ (-32.4 mV) and GOQDs-HA (-29.6 mV) showed negative

values of ζ potentials in their aqueous dispersions. The presence of primary amines was also qualitatively verified with the Kaiser test[34], the GOQDs-NH₂ solution showed an intense blue color after the Kaiser test procedure. The successful conjugation of HA on GOQDs-NH₂ was further confirmed by Fourier transformed infrared (FTIR) Spectroscopy. As illustrated in Fig. 3.7 several new absorbance characteristics of HA appear at 1655 cm⁻¹ (amide I stretching vibration band), 1422 cm⁻¹ (carboxylate symmetric stretching), 1260 cm⁻¹ (skeletal acetal valence band) and 1023 cm⁻¹ (C-O stretching).

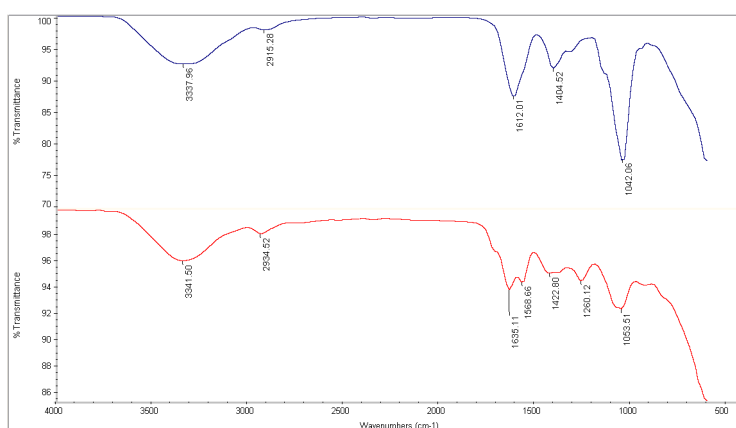


Figure 3.7: FTIR spectra of GOQDs-NH₂ (blue) and GOQDs-HA (red)

3.4.5 Optical Properties

The fluorescence intensity measurements (PL intensity) were used to monitor the progress of the GOQDs-NH₂ formation reaction. As shown in Fig. 3.8a PL appears ca. after 1 h of reaction and it reaches its maximum value after 8 h of heating at 80°C, after which the PL intensity decreases. Fig. 3.8 b,c and d show the PL emission (λ_{EX} 350 nm (3.8b); λ_{EM} 400 nm (3.8c)) and the UV-visible absorption of GOQDs-NH₂ after purification. The PL emission spectra of GQDs exhibit the characteristic feature of luminescent graphene-based nanomaterials, in which the PL emission maximum is shifted to lower energy when the excitation wavelength increases. This shift originates from the optical selection of different surface defect states near the Fermi level[35]. UV-Vis spectrum showed a characteristic peak at around 232 nm, which is attributed

to π - π^* transition of aromatic sp^2 domains.

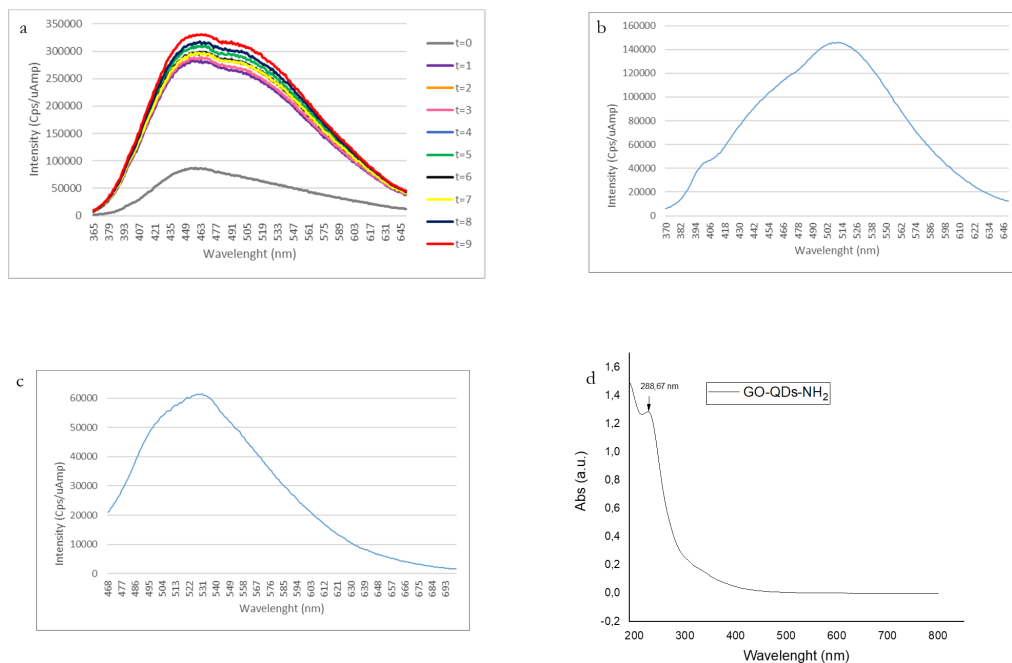


Figure 3.8: a) Temporal evolution of PL emission during preparation of GOQDs-NH₂; b) PL emission spectrum of GOQDs-NH₂, λ_{EX} 350 nm, λ_{EM} 370-650 nm; c) PL emission spectrum of GOQDs-NH₂, λ_{EX} 405nm, λ_{EM} 648-700 nm; d) UV-VIS

3.4.6 Curcumin loading and release

With the large specific surface area, GOQDs are supposed to have excellent loading behaviour. Curcumin (Cur) was selected as a model hydrophobic drug to analyse the loading and release capacity of pharmacologically active molecules from GOQDs-NH₂ and GOQDs-HA. Curcumin was loaded on the surface of the QDs by exploiting the hydrophobic π - π interactions between the aromatic structure of Cur and the aromatic network of the QDs. The Cur loading yield (%) was calculated from a Cur calibration curve by measuring the absorbance at 425 nm. It was found that both systems had a high loading efficiency, the drug loading ratio for GOQDs-NH₂ was higher than that of GOQDs-HA (225% for GOQDs-NH₂ and 177% for GOQDs-HA) probably due to the coating with

hyaluronic acid which hides the aromatic surface of the QDs. Because the tumor microenvironment is acidic compared to normal tissues, which are neutral, using a pH-sensitive drug delivery device for regulated drug release can be useful. The Cur release patterns from GOQDs-NH₂ and GQDs-HA nanocarriers were evaluated at 37°C for 72 h at two pH values of 7.4 and 5.5 as a representation of physiological pH of whole-body fluid and intracellular lysosomes and endosomes, respectively, to explore pH sensitivity and sustained drug release. As highlighted in Fig.3.9a at pH 7.4, GOQDs-HA release only 20% of Cur in the first 10 h, then the release remains almost constant until it drastically increases after 70 h. This increase can be related to crowded hydrogen bonds between the curcumin molecules and the polymeric matrix[36]. The release of Cur from GOQDs-NH₂ instead reaches 50% already in the first 5 h of the experiment and then follows a trend similar to that of GOQDs-HA. The Cur release from the GOQDs-HA demonstrated a slower release rate in comparison to that from GOQDs-NH₂, indicating that HA could cap the GQDs to slow down Cur release. This is particularly relevant if we consider the intravenous administration of nanocarriers, the surface coating in fact could slow down the early release of the drug during the blood circulation. In acidic conditions (Fig. 3.9b), the Cur release trend did not change significantly. It seems that pH variation does not significantly affect the Cur release. This has also been demonstrated in other works and was attributed to the fact that nanocarriers can prevent the curcumin decomposition under the neutral-basic pH conditions[29]. As previously described, nano-sized carbon materials, have a high photothermal effect under low-power near-infrared (NIR) irradiation due to their effective light-to-heat conversion compared to other carbon allotropes[19] hence they are promising candidates for photothermal therapy, a non-invasive treatment based on the photo-absorbers to generate heat from light absorption to burn cancer cells. If the light absorber is also a drug delivery system, it is possible to combine chemotherapy with phototherapy. The local temperature increase generated by irradiation in fact promotes drug release and cell death by cavitation. To simulate the photothermal effect, we investigated the release of Cur from GOQDs-NH₂ and GOQDs-HA at 60 °C in an interval of 5 min (Fig. 3.9c). Again, GOQDs-HA showed less release at the beginning of the experi-

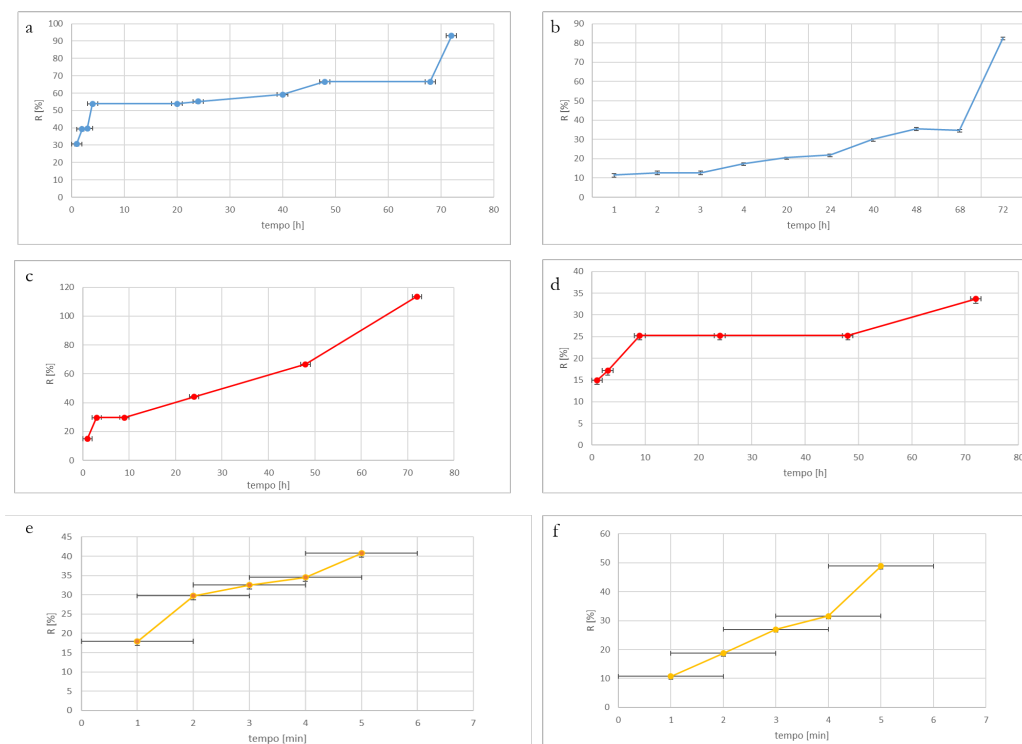


Figure 3.9: Cur release from a) GOQDs-NH₂, b) GOQDs-HA a pH 7.4 (blue), 5.5 (red) and a 60°C (orange)

ment and then the amount of Cur released increased exponentially over the next 5 min. The significantly enhanced release of Cur from nanocomposites could be ascribed to the accelerated thermal motion of molecules at higher temperature. Thus, drug release could be enhanced by the photothermal effect at tumor sites.

3.4.7 Cellular Internalization and Cell viability

Cell internalization on human dermal fibroblasts, HDFs and on non-transformed epithelial breast cells, MCF10A, and invasive breast adenocarcinoma cells MDA-MB-231 was investigated by exploiting the fluorescence of GOQDs. The fluorescence intensity for GOQDs-NH₂, GOQDs-HA (λ_{ex} 350 nm and λ_{em} 500 nm) was quantified for 9 different concentrations and for the blank 1x TNE buffer. Then, the best fitting linear regression models (i.e. calibration curves) for the three systems were evaluated in Excel 2021 (Fig. 3.10a). Uptake experiments were performed by incubating MCF10A, MDA-MB-231 and HDF cells with GOQDs-NH₂ and GOQDs-HA for 24 h at 37 °C. The data clearly show that (Fig. 3.10b,c) the internalization of GOQDs-HA is higher than the simple GOQDs both in MDA-MB-231 and in MCF10A indicating an active role of HA in mediating the recognition with the plasma membrane through the surface receptor CD44, as previously reported for both cell lines[37]. The high internalization of GOQDs-NH₂ without surface coating could be explained by the formation of the protein corona around the NP surface in the serum-rich medium[38]. The internalization ability of both systems resulted to be higher in HDFs than in MCF10A and MDA-MB-231 cells. These findings could be explained by considering the different sizes of the two cell lines. In fact, HDFs exhibit greater spreading area in comparison with MCF10A and MDA-MB-231 cells (data not shown), that could be associated to different cell volume. Further experiments should be performed in order to quantify the quantity of internalized NPs per cell volume and to substantiate the differences observed between the two cell lines. Cell viability was assessed 24 h after incubation with different NPs systems. As reported in Fig.3.11, at the concentration of 0.01 mg/ml, both NP systems here investigated possess no significant toxic effects on viability of

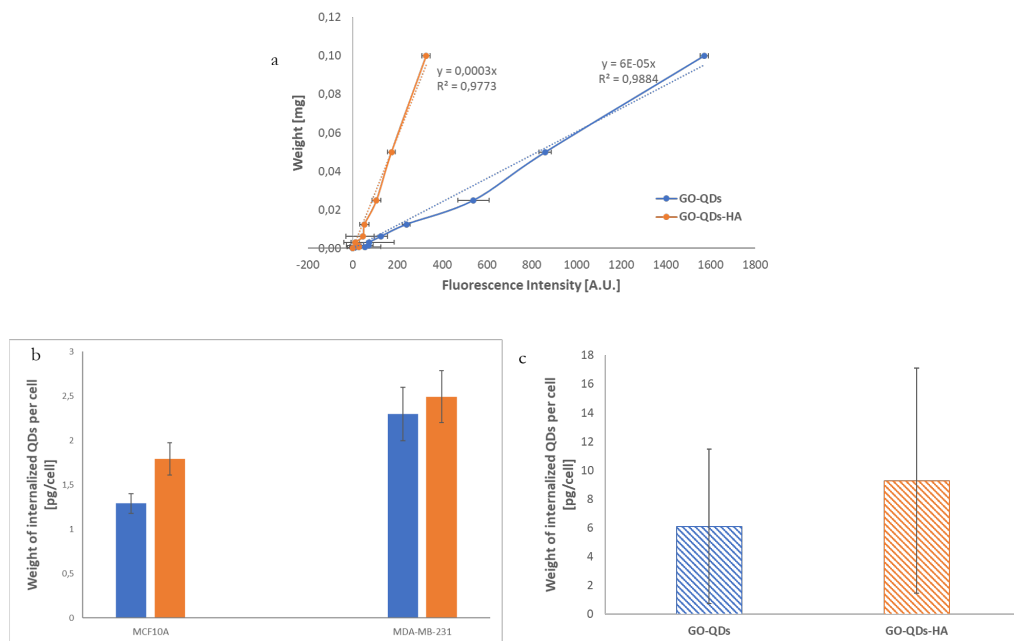


Figure 3.10: a) Calibration curves from GOQDs-NH₂ and GOQDs-HA; b) Internalization of GOQDs-NH₂ (blue) and GOQDs-HA (orange) in MCF10A and MDA-MB231 cells; c) Internalization of GOQDs-NH₂ (blue) and GOQDs-HA (orange) in HDFs cells

HDFs cell. The same cell viability was also observed in the MCF10A and MDA-MB-231 cells treated with GOQDs-NH₂ and GOQDs-HA (data not shown). In

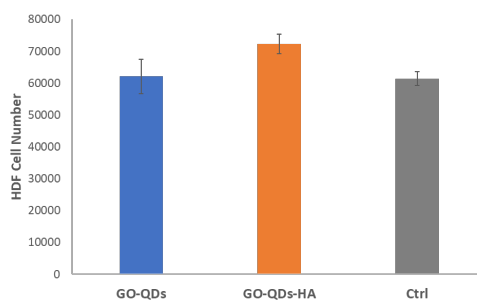


Figure 3.11: Cell viability of HDFs cell treated with 0.01mg/ml of GOQDs-NH₂ and GOQDs-HA

order to investigate the mechanisms of cellular internalization, HDFs cells were incubated with GO-QDs-HA-Rhod. After 24h incubation, lysosomes were localized by treatment with Mouse anti-LAMP 2 polyclonal primary antibodies and, with AlexaFluor 488 goat anti-mouse secondary antibodies. HDFs cells were observed at a confocal microscope. Representative confocal images of HDFs incubated with GO-QDs-HA-Rhod are reported in Fig.3.12a. The overlap coefficient between the NP system and lysosomes was calculated and resulted to be almost 0.9. The accumulation of GO-QDs-HA-Rhod in lysosomes indicates that GOQDs-HA are mainly delivered by classical endocytosis. Furthermore, the internalization capability was evaluated by fluorescence microscopy in terms of integrated fluorescence per unit area and, as expected, we found that the amount of internalized GOQDs-HA-Rhod significantly increased by a factor 1.3 when the incubation time was enhanced from 6 to 24 h (Fig.3.12b).

3.4.8 GOQDs-NH₂ and GOQDs-HA 3D Dermis Microtissue (HDF μ TPs) internalization

Three-dimensional microtissues (μ TPs) are biohybrid tissues obtained by a bottom-up tissue engineering approach based on dynamic cell seeding of bovine fibroblasts on porous gelatine microcarriers using a spinner flask bioreactor[28]. This biohybrids are 3D functional dermal tissues equivalent because they present

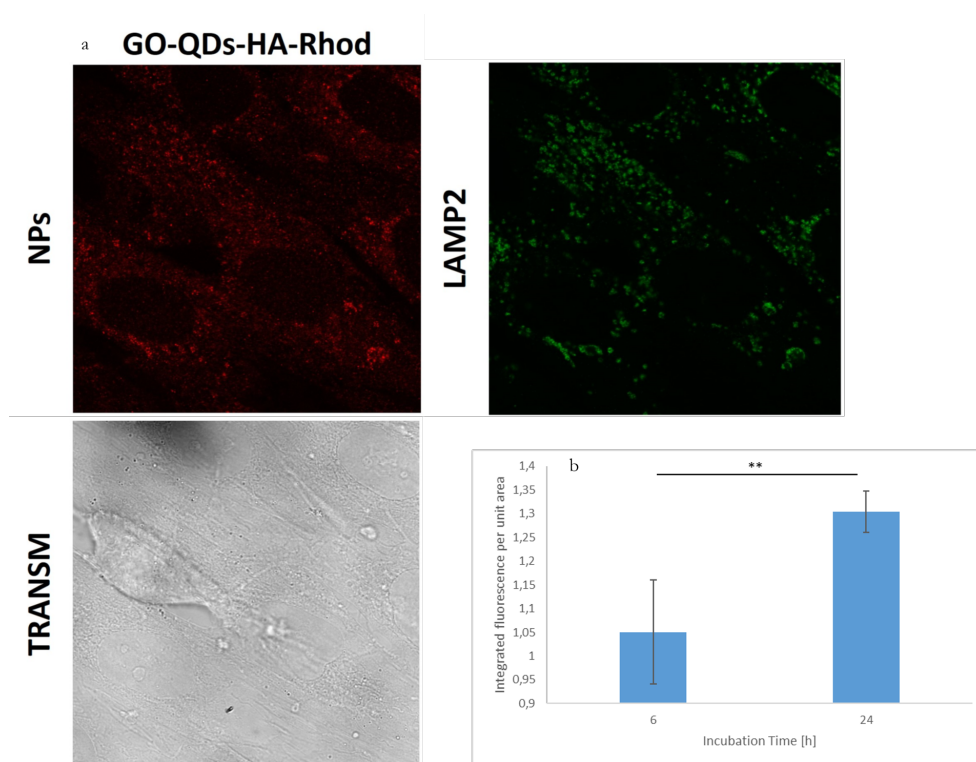


Figure 3.12: a) Representative confocal images of HDFs cells incubated with GOQDs-HA-Rhod. b) Integrated fluorescence per unit area (Statistical comparisons were performed with a student's unpaired test. **, $P < 0.01$)

both a homogeneous and compact aspect and an abundant extracellular matrix (ECM), rich in type I collagen, interconnecting the μ TPs. Therefore, they represent ideal models for studying tissue penetration of engineered drug delivery systems. After contacting the micro-tissues obtained with GOQDs-HA at a concentration of 0.1 and 0.001 mg/ml, the tissues were washed and confocal microscopy was used to assess tissue penetration after 24, 48 and 72 h. Unfortunately, the confocal images did not allow to recognize any signal related to GOQDs, due to the high auto fluorescence of the cells and collagen constituting the tissues (data not shown). So we labeled GOQDs-HA with a fluorophore, the Rhodamine B isothiocyanate (Rhod. B). As in the case of Cur, Rhod.B was conjugated to GOQDs by exploiting the electrostatic interactions of the sp^2 carbon network with the aromatic structure of the fluorophore. Successful dye loading was verified by the fluorescence spectrum of GOQDs-HA-Rhod.B, as shown in Fig.3.19 in Supporting Information, while % fluorophore loading was measured by UV-Vis absorption measurement at 557 nm, through a Rhod.B calibration curve (Fig. S4b). However, the selection of Rhodamine as a fluorophore was not successful as the excitation at 488 nm did not allow to exclude the autofluorescence of the cells (Fig. 3.13). After careful removal of the background, from the fluorescence intensities it could be determined that GOQDs-HA-Rhod.B at the concentration of 0.1 mg/ml showed greater penetration than the concentration of 0.001 mg/ml, the signal related to the Rhodaminated GOQDs at the concentration of 0.1 mg/ml in tissue was maximum after 24 h from incubation and decreased after 48 and 72 h. In order to further investigate the presence of GOQDs-HA-Rhod.B in the treated micro-tissues, we carried out Fluorescence-lifetime imaging microscopy (FLIM) measurement. FLIM is a fluorescence imaging technique where the contrast is based on the lifetime of individual fluorophores rather than their emission spectra. The fluorescence lifetime is defined as the average time that a molecule remains in an excited state prior to returning to the ground state by emitting a photon. Fluorescence lifetime is more robust than intensity-based approaches since it is independent of concentration, sample absorption, sample thickness, photo-bleaching, and/or excitation intensity. With this technique the aim was to be independent from the autofluorescence of micro-tissues. As shown in Fig. 3.14, the lifetime

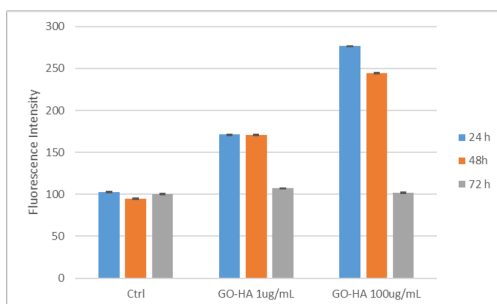
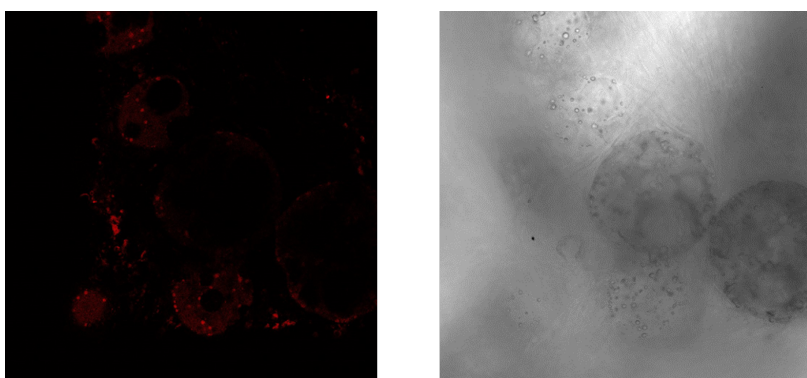


Figure 3.13: Confocal analysis GOQDs-HA-Rhod.B in 3D μ TPs after 24 h incubation at 0.1 mg/ml (top). Fluorescence Intensity Quantification

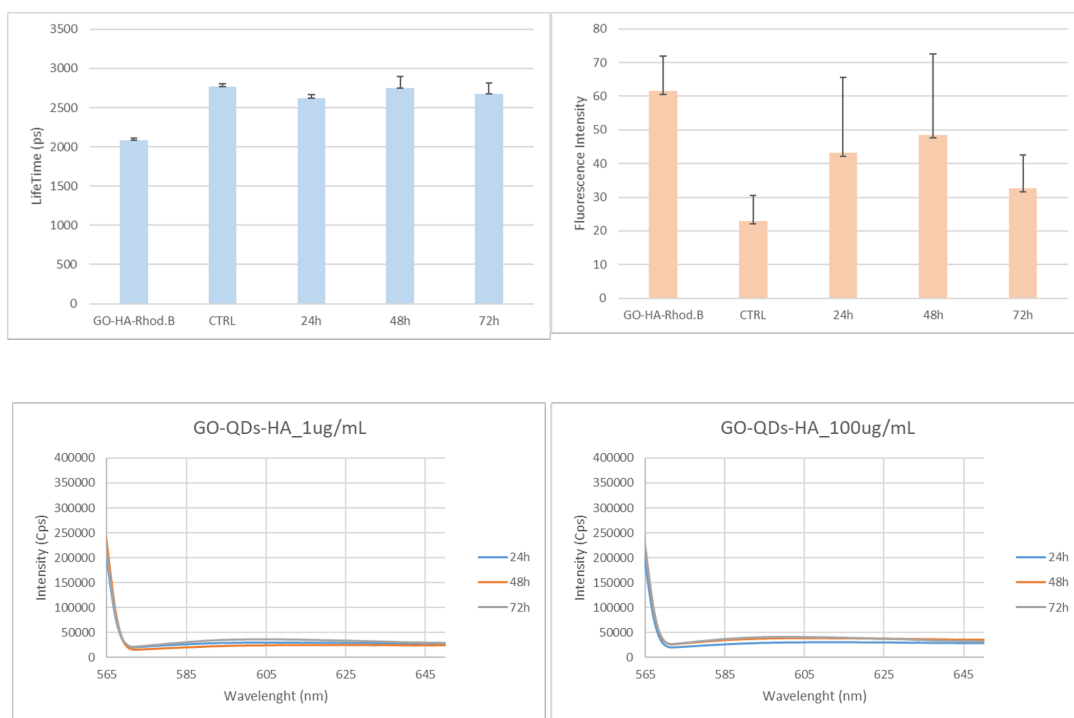


Figure 3.14: Confocal analysis GOQDs-HA-Rhod.B in 3D μ TPs after 24 h incubation at 0.1 mg/ml (top). Fluorescence Intensity Quantification

of GOQDs-HA-Rhod.B was around 2ns, a value compatible with the lifetime of Rhod.B reported in the literature[39], while the untreated microtissues had a longer lifetime. Therefore, we expected that the micro-tissues treated with GOQDs-HA-Rhod.B at a concentration of 0.1 mg/ml would show a decrease in lifetime as the nanoparticles penetrated them. Unfortunately, this type of trend was not observed in the micro-tissues treated with GOQDs-HA-Rhod.B. The FLIM microscopy allows to obtain also the fluorescence intensities. In-

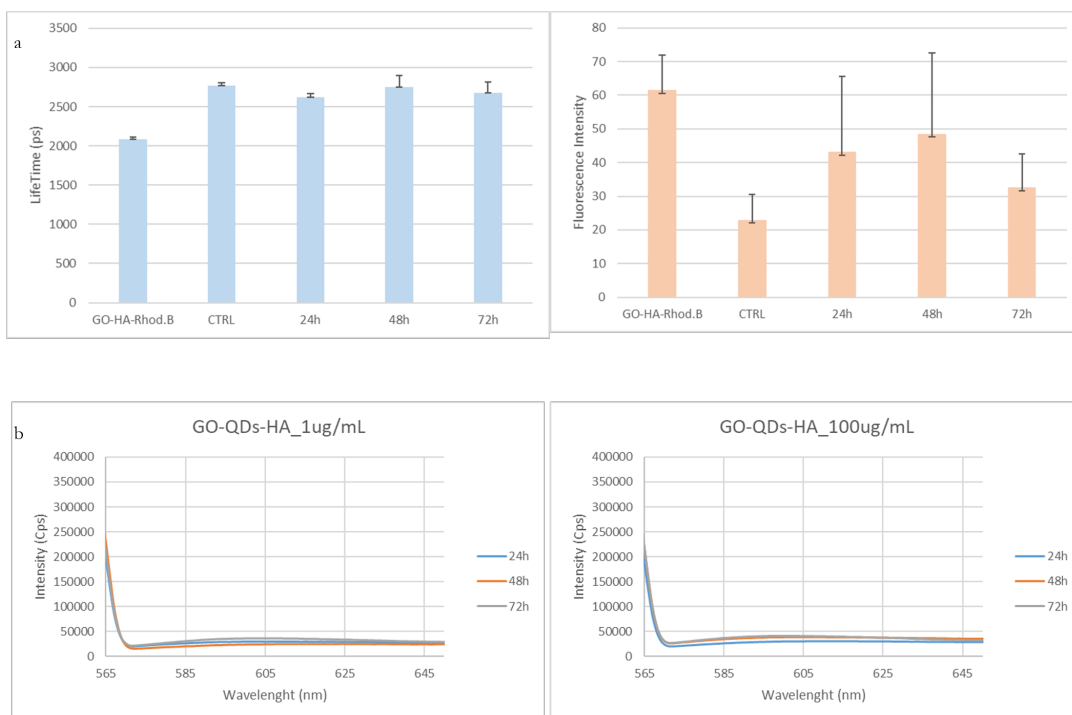


Figure 3.15: a) Life-Time (left) and Fluorescence Intensity (right) of μ TPs treated with GOQDs-HA-Rhod.B 0.1mg/ml from FRET analysis. b) Fluorescence spectra of supernatants obtained after GOQDs-HA-Rhod.B μ TPs incubation

terestingly, as shown in Fig. 3.15a, the fluorescence intensity of the micro-tissues treated with the NP increased compared to the untreated micro-tissues. Another proof even though indirect of uptake of GOQDs-HA-Rhod.B into the micro-tissues was based on the analysis of the supernatants after GOQDs-HA-Rhod.B μ TPs incubation and recording of the fluorescence emission spectra (λ_{ex} 550 nm λ_{em} 570-700 nm). No rhodamine-related signals were present

in the supernatants analysed (Fig.3.15b) indicating a complete uptake by the μ TPs. Further investigation is needed to understand the level of penetration over time within μ TPs.

3.5 Conclusion

In the present study, amino functionalized GOQDs were synthesized starting from the graphene oxide obtained with the Hummer method through an oxidative cutting that involves the combined action of hydrogen peroxide and ammonia. The eco-friendly oxidative cutting ensures a high purity of the material, starting from a carefully purified precursor, and the amino functionalization increases the biocompatibility, making the obtained GO-QDs-NH₂ promising candidates for biomedical applications. The prepared GOQDs-NH₂ have been studied by transmission electron microscopy (TEM) with selected area electron diffraction (SAED), transmission electron cryomicroscopy (CryoTEM), X-ray photoelectron spectroscopy (XPS), Raman spectroscopy. Hyaluronic acid, a natural ligand of CD44 receptors, was covalently bonded to GO-QDs-NH₂ to enable targeted uptake by cancer cells. The amine moieties on GO-QDs-NH₂ and the carboxylic acids on HA chains were coupled to form the GO-QDs-HA conjugate. The GOQDs-HA obtained showed high stability in aqueous solution, as expected by the negative values of their ζ potentials. In order to investigate the possible applications of GOQDs-HA as drug delivery systems, curcumin was incorporated into nanoparticles by non-covalent interactions as a model drug and the release was studied at 37 $\hat{c} \longrightarrow ircC$ in neutral and acidic conditions (to mimic the conditions of the tumor microenvironment) and at 60 $\hat{c} \longrightarrow ircC$ to mimic the photothermal effect typical of carbon nanomaterials when irradiated with near infrared radiation. GOQDs-HA showed lower Cur loading efficiency than nanosystems without HA coating, but exhibited a slower release rate in comparison to that from GOQDs-NH₂, indicating that HA could cap the GQDs to slow down Cur release. This is particularly relevant if we consider the intravenous administration of nanocarriers, the surface coating in fact could slow down the early release of the drug during the blood circulation. The in vitro tests on cellular internalization showed that coating with HA

is effective in increasing cellular internalization. Given their stability and non-cytotoxicity, GOQDs-HA could be explored as the ideal nanocarriers for drug delivery and intracellular fluorescent nanoprobe. However, further studies are needed to understand internalization in cells and tissues.

3.6 Supporting Information

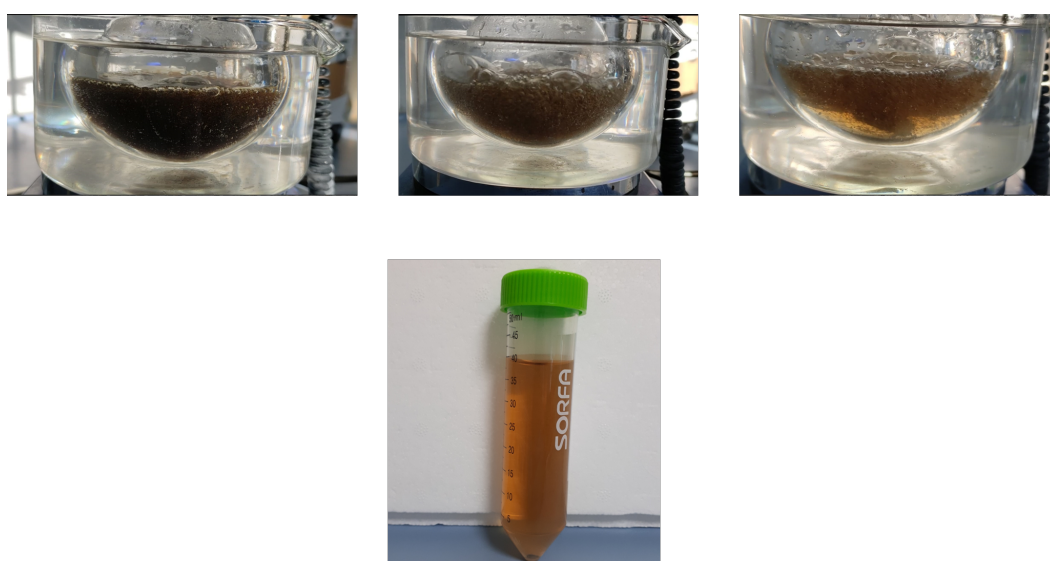


Figure 3.16: Frame of the proceeding of the formation reaction of GOQDs-NH₂ (top), GOQDs-NH₂ obtained after purification (down)

Sample	O1s area [%]		
	C-O	O-C=O	O=C
GO_{Hummer}	71.96	13.76	14.28
GOQDs-NH₂	48.18	13.73	38.09
GOQDs-HA	73.98		26.02

Table 3.4: Binding Energy Values in O1s level from XPS analysis

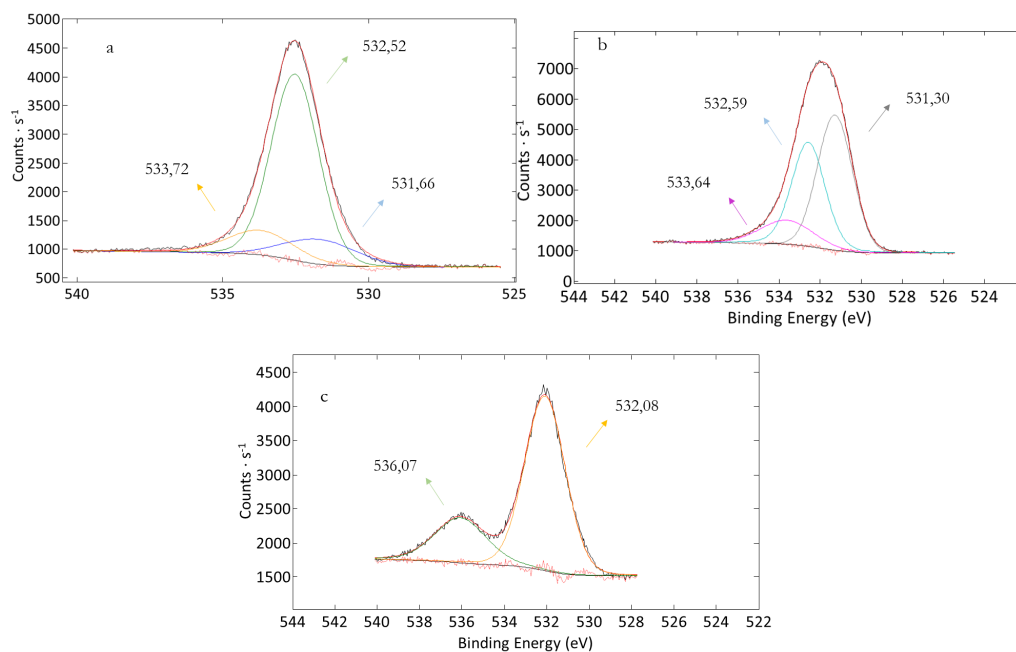


Figure 3.17: De-convoluted O1s core level XPS spectra for a) GO_{Hummer}, b) GOQDs-NH₂, c) GOQDs-HA

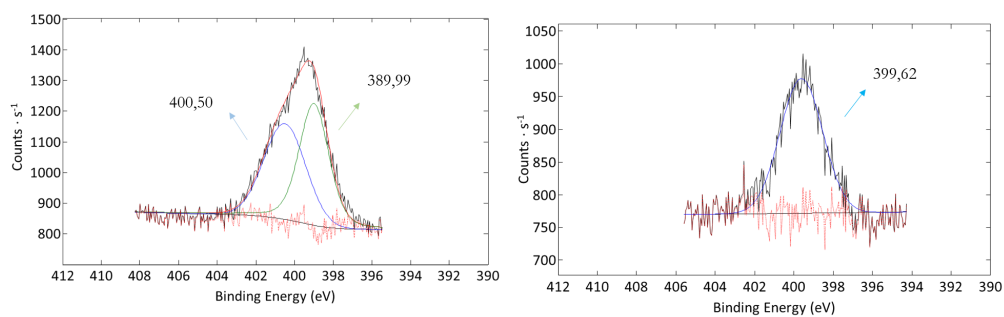


Figure 3.18: De-convoluted N1s core level XPS spectra for a) GOQDs-NH₂, b) GOQDs-HA

N1s area [%]		
Sample	C-N/C=N	NH ₃ ⁺
GOQDs-NH ₂	51.05	48.95
GOQDs-HA	100	

Table 3.5: Binding Energy Values in N1s level from XPS analysis

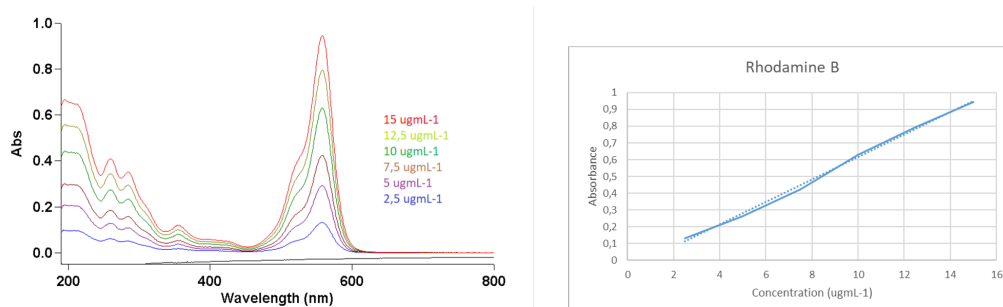


Figure 3.19: Calibration Curve of RhodamineB

References

- [1] Muazim K, Hussain Z. Graphene oxide-A platform towards theranostics; in *Mater Sci Eng C* 2017;76:1274-88.
- [2] Gonçalves G, Vila M, Bdikin I, De Andrés A, Emami N, Ferreira RAS, et al. Breakdown into nanoscale of graphene oxide: Confined hot spot atomic reduction and fragmentation; *Sci Rep* 2014;41(1):1-8.
- [3] Zhang C, Lu T, Tao J, Wan G, Zhao H. Co-delivery of paclitaxel and indocyanine green by PEGylated graphene oxide: A potential integrated nanoplat-form for tumor theranostics; *RSC Adv* 2016;6(19):15460-68.
- [4] Tiwari H, Karki N, Pal M, Basak S, Verma RK, Bal R, et al. Functionalized graphene oxide as a nanocarrier for dual drug delivery applications: The synergistic effect of quercetin and gefitinib against ovarian cancer cells; *Colloids Surfaces B Biointerfaces* 2019;178:452-59.
- [5] Iannazzo D, Pistone A, Salamó M, Galvagno S, Romeo R, Giofré S V, et al. Graphene quantum dots for cancer targeted drug delivery; *Int J Pharm* 2017;518(1-2):185-92.
- [6] Khodadadei F, Safarian S, Ghanbari N. Methotrexate-loaded nitrogen-doped graphene quantum dots nanocarriers as an efficient anticancer drug delivery system; *Mater Sci Eng C* 2017;79:280-85.
- [7] Ko NR, Nafiujjaman M, Lee JS, Lim H-N, Lee Y, Kwon IK. Graphene quantum dot-based theranostic agents for active targeting of breast cancer; *Rsc Adv* 2017;7(19):11420-27.

- [8] Jin SH, Kim DH, Jun GH, Hong SH, Jeon S. Tuning the photoluminescence of graphene quantum dots through the charge transfer effect of functional groups; *ACS Nano* 2013;7(2):1239-45.
- [9] Jin SH, Kim DH, Jun GH, Hong SH, Jeon S. Tuning the photoluminescence of graphene quantum dots through the charge transfer effect of functional groups; *ACS Nano* 2013;7(2):1239-45.
- [10] Fan Z, Li S, Yuan F, Fan L. Fluorescent graphene quantum dots for biosensing and bioimaging; *RSC Adv* 2015;5(25):19773-89.
- [11] Thakur M, Kumawat MK, Srivastava R. Multifunctional graphene quantum dots for combined photothermal and photodynamic therapy coupled with cancer cell tracking applications; *RSC Adv* 2017;7(9):5251-61.
- [12] Gayen B, Palchoudhury S, Chowdhury J. Carbon dots: A mystic star in the world of nanoscience; *Journal of Nanomaterials* 2019.
- [13] Tufano I, Vecchione R, Netti PA. Methods to Scale Down Graphene Oxide Size and Size Implication in Anti-cancer Applications; *Front Bioeng Biotechnol* 2020;7(8):1381-45.
- [14] Jiang F, Chen D, Li R, Wang Y, Zhang G, Li S, et al. Eco-friendly synthesis of size-controllable amine-functionalized graphene quantum dots with antimycoplasma properties; *Nanoscale* 2013;5(3):1137-42.
- [15] Liu Y, Wu P. Graphene quantum dot hybrids as efficient metal-free electrocatalyst for the oxygen reduction reaction; *ACS Appl Mater Interfaces* 2013;5(8):3362-69.
- [16] Singh SK, Singh MK, Kulkarni PP, Sonkar VK, Grácio JJA, Dash D. Amine-modified graphene: Thrombo-protective safer alternative to graphene oxide for biomedical applications; *ACS Nano* 2012;6(3):2731-40.
- [17] Singh SK, Singh MK, Nayak MK, Kumari S, Shrivastava S, Grácio JJA, et al. Thrombus inducing property of atomically thin graphene oxide sheets; *ACS Nano* 2011;5(6):4687-96.

- [18] Liu Z, Robinson JT, Sun X, Dai H. PEGylated nanographene oxide for delivery of water-insoluble cancer drugs; *J Am Chem Soc* 2008;130(33):10876-77.
- [19] Pan Q, Lv Y, Williams GR, Tao L, Yang H, Li H, et al. Lactobionic acid and carboxymethyl chitosan functionalized graphene oxide nanocomposites as targeted anticancer drug delivery systems; *Carbohydr Polym* 2016;151:812-820.
- [20] Jung HS, Kong WH, Sung DK, Lee MY, Beack SE, Keum DH, et al. Nanographene oxide-hyaluronic acid conjugate for photothermal ablation therapy of skin cancer; *ACS Nano* 2014;8(1):260-68.
- [21] Sharma H, Mondal S. Functionalized graphene oxide for chemotherapeutic drug delivery and cancer treatment: A promising material in nanomedicine; *Int J Mol Sci* 2020;21(17):6280.
- [22] Lee SY, Kang MS, Jeong WY, Han D-W, Kim KS. Hyaluronic acid-based theranostic nanomedicines for targeted cancer therapy; *Cancers (Basel)* 2020;12(4):940.
- [23] Necas J, Bartosikova L, Brauner P, Kolar J. Hyaluronic acid (hyaluronan): a review; *Vet Med (Praha)* 2008;53(8):397-411.
- [24] Knudson CB, Knudson W. Hyaluronan-binding proteins in development, tissue homeostasis, and disease; *FASEB J* 1993;7(13):1233-41.
- [25] Banerji S, Wright AJ, Noble M, Mahoney DJ, Campbell ID, Day AJ, et al. Structures of the Cd44-hyaluronan complex provide insight into a fundamental carbohydrate-protein interaction; *Nat Struct Mol Biol* 2007;14(3):234-39.
- [26] Chen J, Yao B, Li C, Shi G. An improved Hummers method for eco-friendly synthesis of graphene oxide; *Carbon N Y* 2013;64:225-29.
- [27] Bolte S, Cordelières FP. A guided tour into subcellular colocalization analysis in light microscopy; *J Microsc* 2006;224(3):213-32.

- [28] Palmiero C, Imperato G, Urciuolo F, Netti P. Engineered dermal equivalent tissue in vitro by assembly of microtissue precursors; *Acta Biomater* 2010;6(7):2548-53.
- [29] Ghanbari N, Salehi Z, Khodadadi AA, Shokrgozar MA, Saboury AA, Farzaneh F. Tryptophan-functionalized graphene quantum dots with enhanced curcumin loading capacity and pH-sensitive release; *J Drug Deliv Sci Technol* 2021;61:102137.
- [30] Karakoçak BB, Laradji A, Primeau T, Berezin MY, Li S, Ravi N. Hyaluronan-conjugated carbon quantum dots for bioimaging use; *ACS Appl Mater Interfaces* 2020;13(1):277-86.
- [31] Kalil H, Maher S, Bose T, Bayachou M. Manganese oxide/hemin-functionalized graphene as a platform for peroxynitrite sensing; *J Electrochem Soc* 2018;165(12):G3133.
- [32] Chen J, Shi T, Cai T, Xu T, Sun L, Wu X, et al. Self healing of defected graphene; *Appl Phys Lett* 2013;102(10):103107.
- [33] Lee H-J, Kim JS, Lee KY, Park KH, Bae J-S, Mubarak M, et al. Elucidation of an intrinsic parameter for evaluating the electrical quality of graphene flakes; *Sci Rep* 2019;9(1):1-8.
- [34] Kaiser E, Colescott RL, Bossinger CD, Cook PI. Color test for detection of free terminal amino groups in the solid-phase synthesis of peptides; *Anal Biochem* 1970;34(2):595-98.
- [35] El-Hnayn R, Canabady-Rochelle L, Desmarests C, Balan L, Rinnert H, Joubert O, et al. One-step synthesis of diamine-functionalized graphene quantum dots from graphene oxide and their chelating and antioxidant activities; *Nanomaterials* 2020;10(1):104.
- [36] Mirzaie Z, Reisi-Vanani A, Barati M. Polyvinyl alcohol-sodium alginate blend, composited with 3D-graphene oxide as a controlled release system for curcumin; *J Drug Deliv Sci Technol* 2019;50:380-87.

- [37] Paliwal SR, Paliwal R, Agrawal GP, Vyas SP. Hyaluronic acid modified pH-sensitive liposomes for targeted intracellular delivery of doxorubicin; *J Liposome Res* 2016;26(4):276-87.
- [38] Guarnieri D, et al. Effect of serum proteins on polystyrene nanoparticle uptake and intracellular trafficking in endothelial cells; *Journal of Nanoparticle Research* 2011;13(9):4295-4309.
- [39] Diac A, Focsan M, Socaci C, Gabudean A-M, Farcau C, Maniu D, et al. Covalent conjugation of carbon dots with Rhodamine B and assessment of their photophysical properties; *RSC Adv* 2015;5(95):77662-69.

Chapter 4

Oil core- functionalized graphene oxide shell

4.1 Abstract

This study aims to develop a theranostic multistage platform for cancer therapy. For these purposes graphene oxide nanosheets coated with hyaluronic acid (GOQDs-HA) are deposited through a Layer by Layer technique on an Oil/Water emulsion (O/W NE) coated with a layer of a biodegradable polymer, chitosan. In this complex system, NE O/W has the potential to remain stable during blood circulation and accumulate preferentially in tumor tissues due to enhanced permeability and retention. After extravasation in the tumor tissue, the degradation of the polymeric matrix should allow the release of GOQDs-HA which, having dimensions around 12 nm and an active targeting system given by hyaluronic acid on their surface, can easily diffuse in the tissue and selectively recognize and penetrate cancer cells.

4.2 Introduction

Nanotheranostic systems represent one of the most active research fields in cancer therapy as they allow to combine, in a single system of nanometric dimensions, therapy drugs and contrast agents in the same doses, avoiding differ-

ences in their biodistribution and increasing both the efficacy of therapeutics and sensitivity of diagnostic techniques[1]. Many research groups are working on biocompatible nanoparticles able to target specific cancer markers and deliver imaging and therapeutic substances for cancer detection and treatment. Over the years, various nanoscale materials such as mesoporous silica nanoparticles[2], liposomes[3], lipoproteins[4], magnetic nanoparticles[5], and Au nanoshells[6] have been used as theranostic platform. The unique properties of NPs (molecular platforms, surface to volume ratio, shape/size control and inherent optical response) make the field of nanomedicine very promising[7]. Nanoparticles around 100-200 nanometers in size can accumulate preferentially in solid tumors by exploiting the altered vascularization and reduced lymphatic drainage typical of a growing tumor mass (EPR effect) thus reducing normal tissue toxicity. Despite being widely exploited, the passive accumulation of nanocarriers by the EPR effect has some limitations. An ideal nanocarrier should simultaneously show a high accumulation in the tumor and cellular internalization after reaching the tumor tissue. Large 100-nm nanoparticles are suitable for the EPR effect, but their diffusion in the dense collagen matrix of the interstitial space is weak, resulting in nanoparticle aggregation around tumor blood vessel and limited penetration into the tumor parenchyma[8]. On the other hands, 10-30 nm nanoparticles show high cellular uptake, but can be easily sequestered by the mononuclear phagocytic system and eliminated. In a recent interview, Gao Xiahou, who recently reported using multimodal magnetic nanoparticles coated with an Au shell[9], has been quoted as saying, «In nanoparticles, one plus one is often less than two» to indicate that a potential problem could be solved by adding on new functionalities to the current structure with an additive approach. In this scenario, Wong et al. developed a multi-stage strategy in which nanoparticles change to enhance transport by adapting to each physiological barrier [8]. This approach was based on Gelatin nanoparticles (Gelatin NPs) of 100 nm containing 10 nm quantum dots in their core. Gelatin NPs have the potential to selectively accumulate in tumor tissue by exploiting the EPR effect. After the accumulation, Gelatin NPs did undergo a size shrinking driven by proteases (MMP-2) that are extensively expressed in the tumor microenvironment, releasing the 10 nm QDs into the tumor inter-

stitial space. The release of QDs with small size (less than 10 nm) increased their diffusion in dense collagen matrix of the interstitial space. Among the diverse nanocarriers for cancer drug delivery studied in the last decades, a particular interest is recognized to Layer-by-Layer (LbL) polymeric nanocapsules, based mainly on electrostatic interaction between the polymers. The LbL assembly technique is simple, low cost, allows precise control of the final particle and is applicable to a variety of polymeric materials[10-12]. From 2014, our team developed biodegradable O/W nanoemulsions (size < 200 nm), specific for hydrophobic drugs, coated with biodegradable polyelectrolytes via LbL technique, with high monodispersity and stability over time[13]. These secondary nanoemulsions offer a number of pharmaceutical and therapeutic benefits, including ease of synthesis, scalable production, good biocompatibility, biodegradability, reasonable stability, and the ability to incorporate hydrophobic drugs and inorganic nanoparticles. Indeed, they've been used to load and release hydrophobic and nutritional chemotherapeutic drugs[14] as well as inorganic contrast agents[15], demonstrating that they are promising drug delivery and diagnostic systems. LbL technology constructs a multi-layered nanoarchitecture held together by electrostatic forces via the charge-charge interaction between the substrate and polyelectrolyte monolayers. Electrostatic interactions, hydrogen bonding, hydrophobic interactions, and van der Waals forces are all thought to play a role in the creation of LbL systems. Nano-Graphene Oxide (nGO or GOQDs), a two-dimensional material featured by a variety of reactive oxygen functional groups such as epoxy and hydroxyl groups on the basal plane and carboxylic acid groups at the sheet edges[16,17], is generally obtained from Graphene Oxide (GO) by converting the micrometric lateral dimensions of the GO sheets to nanometric size (below 50 nm) by applying several methods which can be broadly characterized as direct controllable synthesis and post synthesis separation[18]. For their unique properties, GOQDs are one of the most promising nanoparticles for nanomedicine applications[19]. First of all, GOQDs possess a large number of reactive functional groups allowing for modification to improve the stability, solubility, and biocompatibility[20]. Furthermore, the large surface area containing aromatic crystalline regions and amorphous sp^3 hybridized domains allows for high loading of hy-

drophobic molecules via van der Waals or π - π interactions, making GO a good candidate for the delivery of water insoluble aromatic anticancer drugs[21]). The GOQDs aromatic structure also allows strong light absorption ability in the near-infrared (NIR) range (700-900 nm), which is referred to as the "therapeutic window" because it is a non-invasive, safe, and skin penetrating radiation[22]. This property is especially appealing for inducing cellular hyperthermia in tumor treatments as a less invasive alternative to surgery (Photothermal therapy)[23]. Interestingly, when GO is reduced to dimensions around tens of nm it exhibits photoluminescence that allow its use as an imaging agent. The photoluminescence of GO is due to the oxygen functionalization of the carbon lattice, which induces the opening of the energy gap[24]. In Chapter 3, we prepared amino-functionalized nano-graphene oxide (GOQDs-NH₂) through a simple and eco-friendly oxidative cutting promoted by hydrogen peroxide and ammonia. Hyaluronic acid (HA) was covalently conjugated to GO by the formation of amide bonds. The obtained HA-coated GO (GOQDs-HA) exhibited very low cytotoxicity towards H1299, MCF10A and MDA-MB-231 cells and it was effectively taken up by cells through CD44 receptor. Here, we present a theranostic system based on the deposition of GOQDs-HA on O/W nanoemulsions in order to create a multistage system able to remain stable during blood circulation, selectively accumulate in tumor tissues both for EPR effect and for active targeting of hyaluronic acid and release, following degradation, the graphene oxide nanosheets. The released GOQDs-HA, having dimensions around 12 nm, can diffuse into the interstitial space of the tumors in order to reach and penetrate into the cells. The multistage theranostic system was prepared through a layer by layer approach exploiting the electrostatic interactions between the layers of opposite charge. O / w nanoemulsion was coated with a layer of chitosan, a biodegradable polymer, to form an ultrastable and surface-negatively charged secondary emulsion, on which GOQDs-HA were deposited. The complete system exhibited high stability up to 90 days from its preparation and high biocompatibility.

4.3 Methods

4.3.1 Materials

O/W NEs were prepared using Soybean oil (density of 0.922 g/ml at 20 °C) and surfactant Lipoid E80 (egg lecithin powder 80-85% enriched with Phosphatidyl choline (PC) and 7-9.5% content in phosphatidyl ethanolamine (PE)) purchased from Lipoid and used without further purification. Millipore Milli-Q water was used for the preparation of all NEs and solutions. Graphite (flakes, +100 mesh), 30% sulphuric acid (H₂SO₄ 95-98% wt), potassium permanganate (KMnO₄) hydrogen peroxide (H₂O₂ 30% w/v), ammonium solution (28-30% w/v NH₃), N-hydroxysuccinimide (NHS), 1-(3-Dimethylaminopropyl)-3-ethyl carbodiimide hydrochloride (EDC), Chitosan (LMW 90-50 kDa), Rhodamine B isothiocyanate, Fluorescein isothiocyanate (FITC) minimum essential medium (MEM), fetal bovine serum (FBS), Eagle's minimal essential medium (EMEM), and 1% of penicillin/streptomycin were purchased from Sigma-Aldrich (Milano, Italy). Hyaluronic Acid 50 kDa was purchased from HAWORKS (Bedminster, NJ 07921 USA). 1% of L-glutamine was obtained from Lonza 17-605E, (Basel, Switzerland). 0.25% trypsin, 1 mM EDTA was purchased from Microtech, (Napoli, Italy) Dialysis membranes were purchased from Spectrum Laboratories Inc (New Brunswick, NJ). Amicon Ultra centrifugal filter units (3 kDa) were purchased from Merck Millipore (Milano, Italy). Polystyrene tissue culture flasks 150 cm² were obtained from Corning Inc., (Corning, NY). All of the reagents were used as received.

4.3.2 Instrumentation

Cryo-TEM analysis was performed using a Tecnai G2 F20 transmission electron microscope (FEI company, the Netherland) equipped with a Shotky field emission gun operating at an acceleration voltage of 200 kV and recorded at low dose with a 2k x 2k Ultrascan (Gatan, USA) CCD camera. Frozen hydrated samples were prepared by applying a 3 µl aliquot to a previously glow discharged 200 mesh holey carbon grid (Ted Pella, USA). Before plunging into nitrogen cooled liquid ethane, the grid was blotted for 1.5s in a chamber at 4 °C and

90% humidity using a FEI Vitrobot Mark IV (FEI Company, the Netherlands). The thickness of the samples were measured on a mica surface by using a Multimode Nanoscope V scanning probe microscopy system (Bruker, USA) with a AFM cantilever tips with a force constant of ~ 50 N/m and resonance vibration frequency of ~ 350 kHz (Bruker, USA) were used. The samples were prepared by solution casting the aqueous suspensions of bilayer on a freshly cleaved mica surface and drying in air. Nanoparticle Tracking Analysis (NTA) measurements were performed in a NanoSight NS300 (Malvern Panalytical Ltd., Malvern, UK), equipped with a sample chamber and a 488 nm laser. For the NTA measurements, bilayer solution was diluted in deionized water (1:4000). Before the analysis, the solution was homogenized for 3 min in an ultrasonic bath. The samples were injected into the chamber with sterile syringes. The size distribution and ζ potential in solution was detected using dynamic light scattering (DLS) instrument (Zetasizer zs nano series ZEN 3600, Malvern Instruments Ltd., Malvern, U.K., λ 632.8 nm). All the samples were diluted up to a droplet concentration of approximately 0.025 wt% by using milli-Q water. ζ -potential analysis was carried out by setting 50 runs for each measurement. The ultraviolet-visible (UV/Vis) spectrum of the sample was measured using a Cary 5000 UV/Vis spectrophotometer. Photoluminescence spectra were obtained using a spectrophotometer LS55 (Perkin Elmer). Confocal fluorescence microscopy images were captured with a Leica TCS SP5 Images were acquired with a field of view $77.5 \times 77.5 \mu\text{m}$ for a pixel size of 76×76 nm. Images were visualized by LAS-AF software (Leica-Microsystems, Mannheim, Germany). A laser scanning confocal microscope TCS SP5 SMD (Leica Microsystems, Germany) equipped with a Chameleon Ultra II 80MHz pulsed NIR laser (Coherent Inc., US) was used for performed co-localization experiments. An HCX IRAPO L 25x/0.95 water immersion objective was used for all the experiments exciting FITC at 740 nm and detecting emission at 500-530 nm, whereas RhodB was excited at 840 nm and its emission was detected at 560-610 nm. LAS-AF software was used for exporting data.

4.3.3 Oil/Water Nanoemulsion (O/W NE) preparation

O/W NE was prepared according to a two-step procedure previously developed[13]. Briefly, first the oil phase was prepared by adding the surfactant Lipoid E80 (5.8 mg) to the soybean oil (20 ml) and mixed at 60 °C under gentle stirring. Then, the oil phase was added drop wise to the water phase (Milli-Q water) and mixed using the immersion sonicator (Ultrasonic Processor VCX500 Sonic and Materials) until there was a suitable dissolution. The pre-emulsions were finally passed at 2000 bar through the high-pressure valve homogenizer (Microfluidics M110PS) for the first three individual cycles to greatly reduce the initial size, then the reservoir was continuously refilled for 200 steps. This method was used for the preparation of an oil-in-water nanoemulsions at 20 wt% of oil concentration. The narrowly distributed O/W NE is coated with a positively charged chitosan layer, which contributes to significantly extend the stability of the system over time. This chitosan-coated NE is named secondary NE. A 0.1 M acetic acid solution of chitosan (CT) or fluorescein isothiocyanate labelled chitosan (CT-FITC) (0.125 wt%) was prepared. O/W NE phase (2.5 ml O/W NE 20 wt% oil in 7.5 ml H₂O) was added to the chitosan solution quickly under vigorous stirring and kept under stirring for 15 min to allow uniform chitosan deposition. Final concentrations of oil and chitosan were 1 wt% and 0.01 wt%, respectively. These nanoemulsions were re-dispersed using the method previously reported and stored at room temperature.

4.3.4 Modification of Chitosan with Fluorescein Isothiocyanate

Chitosan (CT) was labelled with fluorescein isothiocyanate (FITC) fluorophore based on a previously reported procedure[25]. CT (100mg, 0.5 mmol) was dissolved in 10 mL of a 0.1M acetic acid solution. After complete dissolution, a solution of FITC (5.0 mg in 500 μ L of DMSO) was added dropwise. The reaction proceeded overnight at room temperature, protected by light. Sample was then dialyzed (dialysis tubing of 3.5 kDa) against water more times for a couple of days to remove no reacted dye. Finally, the purified product was freeze-dried for 24 h. The degree of functionalization was determined with ¹NMR spectra and it resulted less than 1%.

4.3.5 Amino-modified GOQDs Preparation

Amino-modified GOQDs (GOQDs-NH₂) were obtained through the oxidative cutting procedure promoted by hydrogen peroxide and ammonia reported in the literature with slight modifications. Briefly, in a 250 mL bottom flask, H₂O₂ (40 ml, 30%) was added to GO_{Hummer} solution (3 ml, 8 mg/ml in H₂O) and the temperature was brought to 80 °C under stirring in an oil bath. Afterward, ammonia (7 ml, 25-28% NH₃) was added dropwise to the mixture, over five hours which was accompanied by vigorous bubbling and heating up. After stirring for 8 h, under reflux, a clear homogenous yellowish-brown mixture was finally obtained with no detectable or precipitated GO remaining. After filtering the as-prepared mixture through a 0.22 μm cellulose acetate membrane, the volume was reduced by evaporation under vacuum. The obtained solution was dialyzed for 2 days against deionized water (MWCO 100-500 Da). freeze-dried and stored at 4 °C in the dark.

4.3.6 GOQDs-Rhodamine B labelling

Rhodamine B (Rho B) was used to label GOQDs by physical adsorption. 158.8 μL of Rho B solution, (1mg/mL in H₂O) was added to 3.58 mL of GOQDs (0.85 mg/mL in H₂O). After stirring for 24h at T room in the dark, the excess of RhoB was washed by dialysis against water for 2 days in the dark. The amount of physio absorbed RhoB in GOQDs-NH₂-Rhod.B was determined from a UV-Vis calibration curve of Rho B at 557 nm.

4.3.7 Conjugation of GOQDs-NH₂ with HA

An aqueous HA (1 w/v%) solution was prepared by dissolving the powder form of HA (0.10 g, 0.24 meq of COOH) in 10 mL DI water overnight. The pH of the HA solution was adjusted to 4.5. EDC (0.45 g, 2.4 mmol) and NHS (0.14 g, 1.2 mmol) were added to the HA solution at 22 °C. After stirring for 1 h, the GOQDs-NH₂ or GOQDs-NH₂-Rhod.B solution (0.10 g, 5 mL) was added to the HA solution, and the reaction mixture was continuously stirred overnight. The pH was adjusted to 8.9 to terminate the reaction. The unreacted species, and

unconjugated GOQDs were removed from the reaction mixture through dialysis (MWCO 12,000-14,000) against DI water (three times), and the GOQDs-HA and GOQDs-HA-Rhod.B conjugated were finally recovered by lyophilisation as a brownish solid.

4.3.8 Layer by Layer GOQDs-HA Deposition on Secondary nanoEmulsion

Starting from the chitosan coated NE or FITC labelled chitosan coated NE (1 wt% oil and 0.01 wt% chitosan), a negatively charged GOQDs-HA or GOQDs-HA-Rhod.B second layer was deposited by mixing 1:1 (v/v) of a 0.24 wt% aqueous solution of GOQDs-HA with the NE suspension. The optimal GOQDs-HA concentration was determined via a saturation curve starting from concentrations of 0.05% w/v of GOQDs up to a concentration of 0.30% w/v. The deposition was obtained through a procedure developed previously in our team that allows for a higher control over the deposition process. Experimentally, the two liquid phases were injected by aid of two syringe pumps (HARVARD APPARATUS 11 PLUS) at the same flow rate (0.4 ml min^{-1}) through two micrometric capillaries interfaced at their extremities. Each drop was then collected inside a glass tube immersed in the ultrasonic bath (FALC INSTRUMENTS), at 10°C , 40 kHz and 100% power to obtain bilayer CT-GOQDs-HA and CT-GOQDs-HA-Rhod.B. For control, a bilayer without GOQDs-HA was prepared with the same LbL procedure (CT-FITC-HA).

4.3.9 Cell culture

Experiments were performed on human dermal fibroblasts, HDFs on non-transformed epithelial breast cells, MCF10A, and on invasive breast adenocarcinoma cells MDA-MB-231. HDFs were extracted from healthy breast biopsies. MCF10A were grown in DMEM/F12 (Gibco) with 5% horse serum, 1% L-glutamine and 1% of penicillin/streptomycin, freshly supplemented with insulin (Sigma-Aldrich), EGF (Peprotech) and hydrocortisone (Sigma-Aldrich). MDA-MB-231 were grown in DMEM/F12 (Gibco) with 10% fetal bovine serum (FBS), 1% L-glutamine and

1% of penicillin/streptomycin. HDFs line was grown in enriched minimum essential medium (MEM) Eagle composed of MEM, 10% and 20% of fetal bovine serum (FBS) respectively, 1% of L-glutamine, and 1% of penicillin/streptomycin. The medium was changed every 2 days until reaching 90% confluence. Cells were washed three times with PBS and incubated with trypsin-ethylenediaminetetraacetic acid (EDTA) (0.25% trypsin, 1 mM EDTA) for 5 min at 37 °C to detach the cells.

Calibration Curve for GOQDs-NH₂, GOQDs-HA and cells

The standard calibration curves for the three systems (GOQDs-HA-Rhod, CT-FITC-HA and CT-GOQDs-HA-Rhod) were obtained by measuring their fluorescence intensity at different and known concentration by a LS55 spectrofluorimeter (Perkin Elmer). In particular, fluorescence spectra were recorded at 349 nm excitation and 577 nm emission wavelengths for GOQDs-HA-Rhod and CT-GOQDs-HA-Rhod and at 488 nm excitation and 515 nm emission wavelengths for CT-FITC-HA. The standard calibration curves for MCF10A, MDA-MB-231 and HDFs cells were obtained by culturing different and known cell numbers in a 24 well plate. Cells were allowed to adhere for 6 h at 37 °C and then incubated with 1 ml of 1 µg/ml nuclear dye Hoechst 33342 (Invitrogen) for 20 min. After incubation, cells were rinsed once to remove non-internalized Hoechst and incubated with 0.5 ml of ddH₂O at 37 °C for 1 h. The samples were then transferred to a -80 °C condition for 30 min and again to 37 °C for 30 min. At this point, cells inflated by water were lysed with 0.5 ml of solution including 2x TNE buffer (10x TNE buffer: 100 mM Tris, 10 mM EDTA, 1.0 M NaCl, pH 7.4). Then, the samples were measured at 350 nm excitation and 500 nm emission wavelengths.

Quantification of GOQDs-NH₂, GOQDs-HA internalization

To quantify the number of internalized nanoparticles (NPs), MCF10A, MDA-MB-231 and HDFs cells were cultured at a density of 40000 cells/well in 24 well plates. 24 h after cell seeding, cells were incubated for 24 h at 37 °C with GOQDs-HA-Rhod, CT-FITC-HA and CT-GOQDs-HA-Rhod dispersed in cell culture medium at a final concentration of 0.01 mg/ml. For each NPs system cells

were cultured in 6 different wells, three of which were used for the quantification of NPs internalization and three for cell counting. After incubation, cells were rinsed five times with PBS to remove non-internalized NPs and three wells were incubated with 1 ml of 1 $\mu\text{g}/\text{ml}$ nuclear dye Hoechst 33342 (Invitrogen) for 20 min. Then, the lysis protocol described in the previous subparagraph was applied and cell lysates not stained with Hoechst dye were analyzed at the wavelengths of the corresponding NPs systems, the cell lysates stained with Hoechst at 350 nm excitation and 500 nm emission wavelengths. Fluorescence intensity values were interpolated with the NP and cell calibration curves and normalized to the recovered cell number to obtain the number of internalized NPs per cell.

Co-localization with lysosomes

After 24 h incubation with GOQDs-HA-Rhod, HDFs were rinsed twice with PBS to remove non-internalized NPs and fixed with 4% paraformaldehyde at RT. Then, cells were permeabilized and blocked with 0.1% saponin-5% bovine serum albumin (BSA)-PBS for 1h at RT. Mouse anti-LAMP 2 polyclonal primary antibodies and, with AlexaFluor 488 (for QDs-GO-HA-Rhod and CT-GO-HA-Rhod) or AlexaFluor 546 (for CT-FITC-HA), goat anti-mouse secondary antibodies (Molecular Probes, Invitrogen) were used to localize the lysosomes. All samples were finally observed at a confocal microscope (SP5 Leica) with a 63x oil immersion objective. The co-localization analysis was performed by JACoP plugin[26] to have an estimate of the overlap coefficient among the pixels in the dual-channel images.

4.4 Result and Discussion

4.4.1 GOQDs-HA coating Oil/Water secondary Emulsion

The first step in the preparation of the theranostic system consisting of GO nanosheets coated with hyaluronic acid deposited on an oil/water (O/W NE) emulsion coated with a layer of chitosan was the preparation of the O/W NE.

The oil phase was prepared by adding the surfactant Lipoid E80 to the soybean oil and mixed at 60°C. Then, the oil phase was added drop wise to the water phase (Milli-Q water) and mixed using the immersion sonicator dissolution. The pre-emulsions were finally passed at 2000 bar through the high-pressure valve homogenizer for the first three individual cycles to greatly reduce the initial size, then the reservoir was continuously refilled for 200 steps. By this method an O/W NE at 20 wt% of oil concentration was obtained. Dynamic light scattering (DLS) analyzes were used to verify size distribution and polydispersity index (PDI). As shown in Fig. 4.1a, the O/W NE showed a very narrow dimensional distribution centered at 98 nm with a PDI value of 0.087. In order to stabilize the O/W NE, we covered the primary nanoemulsion with a layer of chitosan (CT), a biodegradable polysaccharide[27]. To prevent aggregation, the secondary NEs were properly re-dispersed according to the procedure previously reported[13]. The success of the CT coating was confirmed by the switching of the ζ Potential which changed from -25.6 mV in the O/W NE to 28.1 mV in the secondary NE. The secondary NE (Monolayer 1% Oil-0.01% CT) showed lateral dimensions similar to the primary O/W NE (Fig. 4.2b) and higher monodispersity as demonstrated by the lower PDI value (0.061 vs 0.087). Amino-functionalized GOQDs coated with hyaluronic acid were prepared and characterized as described in Chapter 3 and was assembled around Monolayer 1%Oil-0.01%CT by a LbL procedure allowing for a high control over the deposition process, as already described elsewhere. In order to determine the right concentration of GOQDs-HA that would ensure a complete switch of the surface charge and therefore a complete coating of the monolayer and also a stability over time, we constructed a calibration curve starting from a GOQDs-HA concentration of 0.05% (w/V) up to a concentration of 0.30% (w/V). By monitoring size (Fig.4.2a), PDI (Fig.4.2b) and ζ potential (Fig.4.2c) parameters over 1 week we established that the GOQDs-HA concentration able to completely cover the monolayer and ensure high stability over time was 0.12% (w/V). The obtained system, Bilayer 0.5%Oil-0.05%CT-0.12%GO-HA showed a high stability in aqueous solution when stored at 4 °C, as evidenced by the values of the DLS parameters recorded up to 180 days from its preparation (Fig. 4.3a). The size of the Bilayer was also analyzed with nanoparticle tracking analysis (NTA)

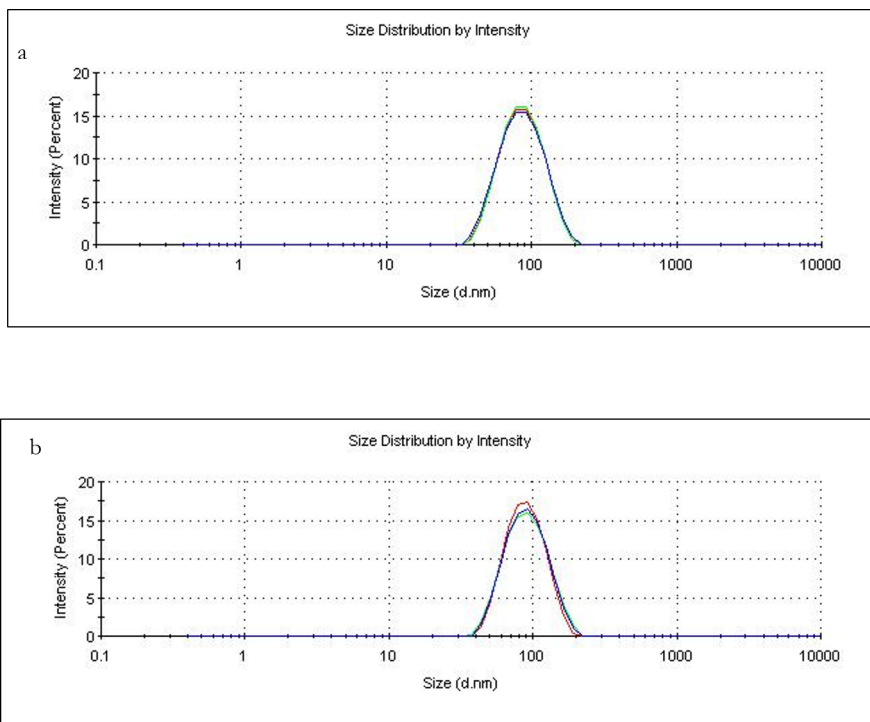


Figure 4.1: DLS Size Distribution of a) O/W NE 20% Oil; b) Monolayer 1%Oil_{0.01%CT}



Figure 4.2: Saturation Curve Bilayer 0.5%Oil-0.05%CT-X%GOQDs-HA

one of the few methods able to visualize and measure nanoparticles in suspension in the range from 10-1000 nm based on the analysis of Brownian motion (Fig.4.3b). The suspensions were diluted with ultrapure water to achieve an optimum concentration range of 10^7 - 10^9 particles per ml (approximately 20-100 particles in the field of view of the NanoSight video window)[28]. Bilayer nanoparticles were dispersed by sonication for 10 min in an ultrasonic bath before introducing them into the NanoSight flow cell. The average size of three measurements gave a value of 112.09 ± 0.7 nm. A comparison between DLS and NTA results demonstrates that DLS may overstate the sample particle sizes. Both approaches yield a hydrodynamic radius (R_h) value, but larger particles scatter more intensely and are better detected by DLS than smaller particles because the scattering intensity effect is proportional to particle size rather than the number of particles of equivalent diameter[29]. Although DLS is a quick, easy, and non-destructive approach, it has this drawback when analysing samples with polydispersity[29]. The distributions have shifted to the greatest particle sizes in these circumstances. Because it is based on the tracking of individual particles, NTA identifies the distribution of sizes (10-2000 nm) with greater precision. The formation of the GOQDs-HA coating around the monolayer was quite evident by comparing the AFM images of the bilayer formed with the GOQDs-HA and of a bilayer obtained by depositing only the hyaluronic acid on the monolayer. The drying process of the nanoemulsion on the mica surface allows to measure the thickness of the remaining graphene oxide layer. As highlighted in Fig. 4.4a, the AFM images of the bilayer indicated a more compact morphology with a thickness of just over 2 nm. In the absence of GOQDs (Fig. 4.4b), however, the sample was less homogeneous and with a thickness greater than 5 nm. AFM images confirmed the high monodispersity and the size distribution verified with NTA measurements. In order to visualize the two system co-localization with confocal microscopy analyses, we labelled the chitosan layer with FITC and we exploited the photoluminescence of the GOQDs to confirm the presence of both layers on the system. Unfortunately, after deposition on the monolayer, the fluorescence intensity of the QDs decreased dramatically (Fig. 4.5 a,b). Fluorescence quenching of GOQDs when bound by electrostatic interactions to positively charged systems can happen as reported in the litera-

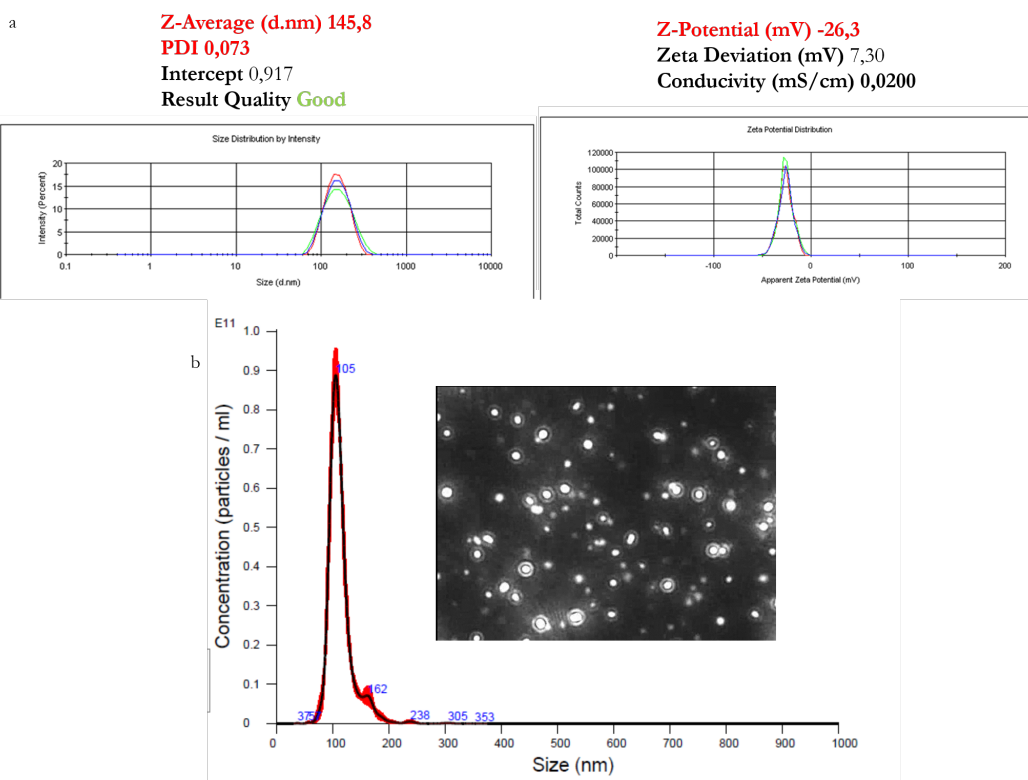


Figure 4.3: a) DLS Size Distribution and ζ Potential Bilayer 0.5%Oil-0.05%CT-0.12%GOQDs-HA after 180 day; b) NTA Size Distribution and frame of nanoparticles detected by NTA camera (insert).

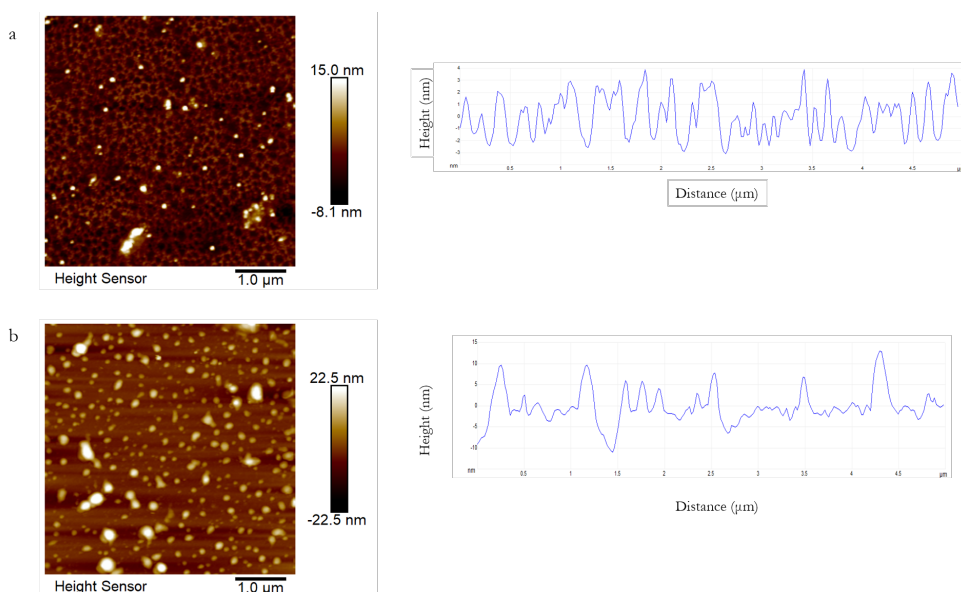


Figure 4.4: AFM images (left) and height profile (right) of a) Bilayer 0.5%Oil-0.05%CT-0.12%GOQDs-HA, b) Bilayer 0.5%Oil-0.05%CT-0.12%HA

ture with water-soluble guanidine-terminated dendrimer[30-31]. We therefore decided to use the Rhodamine-labeled GOQDs-HA used in the tissue penetration experiments in Chapter 3. Rhod.B was conjugated to GOQDs- by exploiting the electrostatic interactions of the sp^2 carbon network with the aromatic structure of the fluorophore. Successful dye loading was verified by the fluorescence spectrum of GOQDs-HA-Rhod.B, as shown in Fig.3.9 (Chapter 3), while % fluorophore loading was measured by UV-Vis absorption measurement at 557 nm through a Rhod.B calibration curve. The fluorescence spectra obtained by exciting at the λ of the two fluorophores confirmed the co-presence of FITC and Rhod.B. (Fig. 4.5 c,d). Multifoton Confocal analysis also proved the narrow distribution feature of the obtained Bilayer 0.5%Oil-0.05%CT-FITC-0.12%GOQDs-HA-Rhod.B and the perfect matching between green and red colors proves the effectiveness of the deposition homogeneity (Fig. 4.6). Interestingly, in the bilayer, when irradiated with 780 nm radiation at, a rapid bubbling phenomenon was observed (Fig. 4.7) which was not evident in the bilayer with fluorophores without GO (data not shown). This phenomenon could be attributed to the presence of GOQDs, but further experiments are needed to prove it.

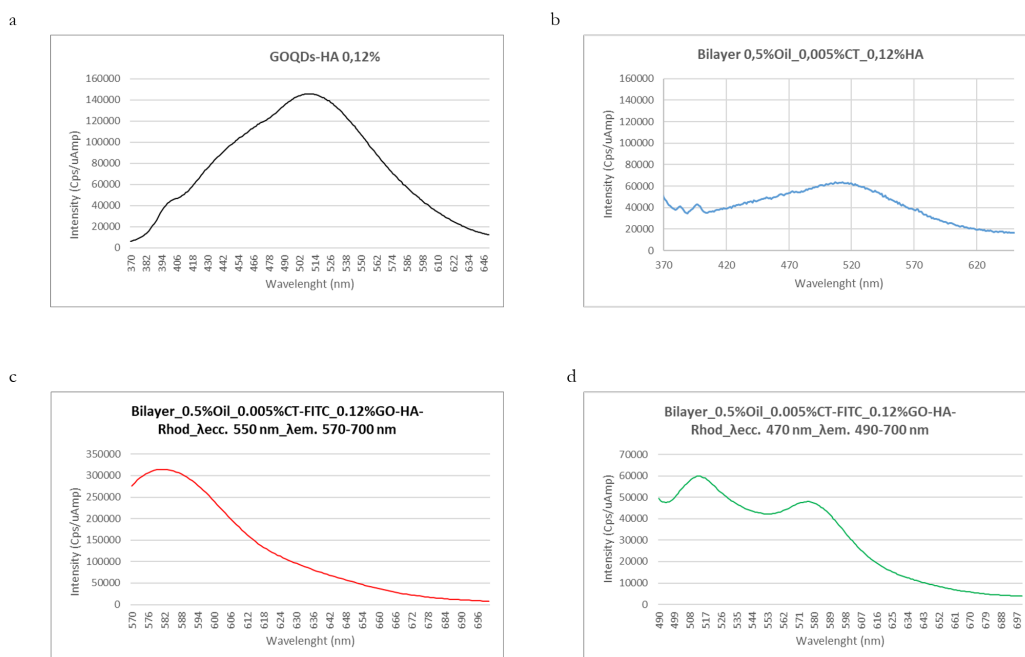


Figure 4.5: Fluorescence spectra of a) GOQDs-HA λ_{EX} 350nm, λ_{EM} 370-650 nm; b) Bilayer 0.5%Oil-0.05%CT-0.12%GOQDs-HA λ_{EX} 350nm, λ_{EM} 370-650 nm; c) Bilayer 0.5%Oil-0.05%CT-FITC-0.12%GOQDs-HA-Rhod.B; d) Bilayer 0.5%Oil-0.05%CT-FITC-0.12%GOQDs-HA-Rhod.B

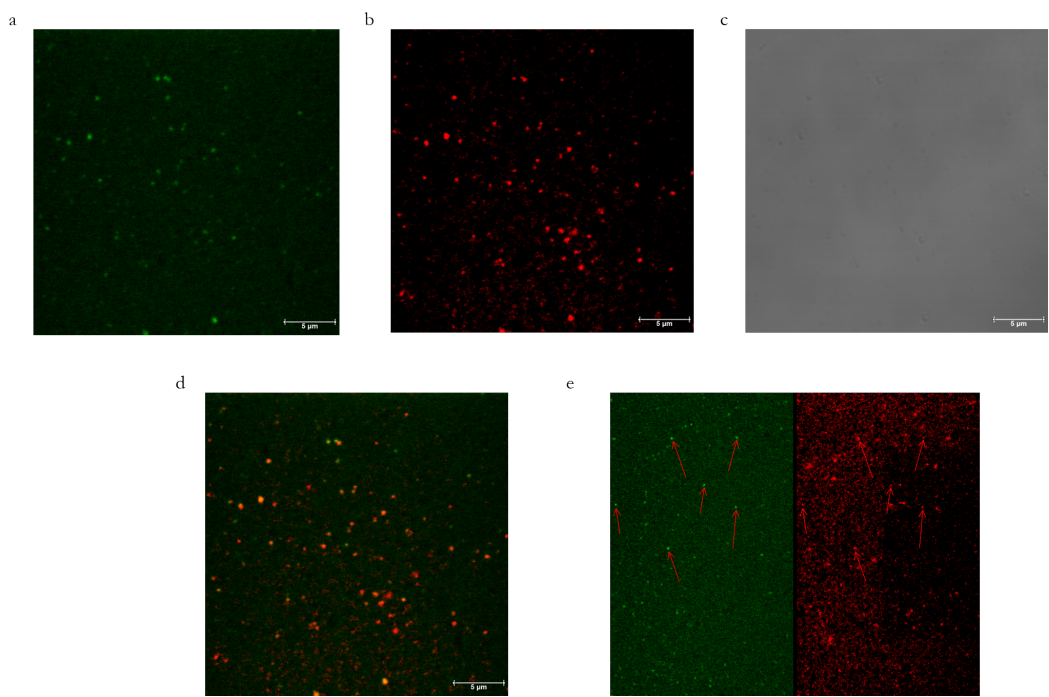


Figure 4.6: Multifoton Confocal images of Bilayer 0.5%Oil-0.05%CT-FITC-0.12%GOQDs-HA-Rhod.B a) FITC Fluorescence, b) Rhodamine Fluorescence; c) Bright field; d,e) overlay

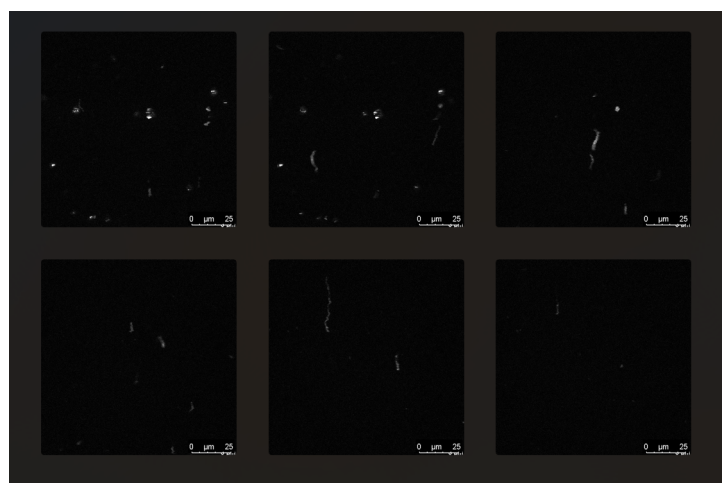


Figure 4.7: Multifoton Confocal images of Bilayer 0.5%Oil-0.05%CT-FITC-0.12%GOQDs-HA-Rhod.B irradiated at 780 nm

4.4.2 Cellular Internalization and Cell viability

Given the low fluorescence intensity of the GOQDs, for cell internalization on HDFs, MCF10A and MDA-MB-231 we decided to use the systems labelled with the fluorophores. GOQDs-HA-Rhod.B was first analysed to demonstrate that labelling with the fluorophore did not change the internalization capacity and did not alter the non-cytotoxicity of the system. The fluorescence intensity for QDs-GO-HA-Rhod (λ_{exc} 349 nm and λ_{em} 577 nm) was quantified for 4 different concentrations and for the blank 1x TNE buffer. Then, the best fitting linear regression models (i.e. calibration curves) for the three systems were evaluated in Excel 2021. Uptake experiments were performed by incubating MCF10A and MDA-MB-231 cells with GOQDs-HA-Rhod.B for 24 h at 37 °C. The data clearly showed that the presence of Rhod.B did not alter the cellular uptake nor the cytotoxicity of GOQDs in both tested cell lines (Fig. 4.8). The approach described

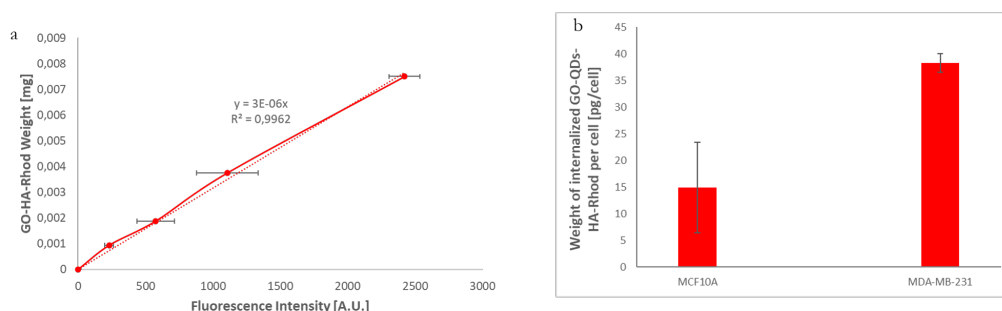


Figure 4.8: Calibration curves from GOQDs-HA-Rhod b) Internalization of GOQDs-HA-Rhod.B in MCF10A and MDA-MB-231 cells.

above was used to calculate the calibration curves for the bilayer systems (NE-CT-FITC-HA and CT-GOQDs-HA-Rhod). For both systems, 4 different concentrations and the blank 1x TNE buffer were used to derive the best fitting linear regression models (Fig. 4.9). Uptake experiments were performed by incubating both cell lines with bilayer NPs for 24 h at 37 °C. In both cell lines, the uptake of CT-GOQDs-HA-Rhod resulted one order of magnitude higher than that of CT-FITC-HA. This type of internalization is very similar to that of GOQDs-HA-Rhod. (Fig. 4.8) and could be justified with the direct uptake of the GOQDa-HA upon bilayer degradation. If confirmed, these cellular internalization data provide further evidence of the multistage approach we are exploring. Cell viability

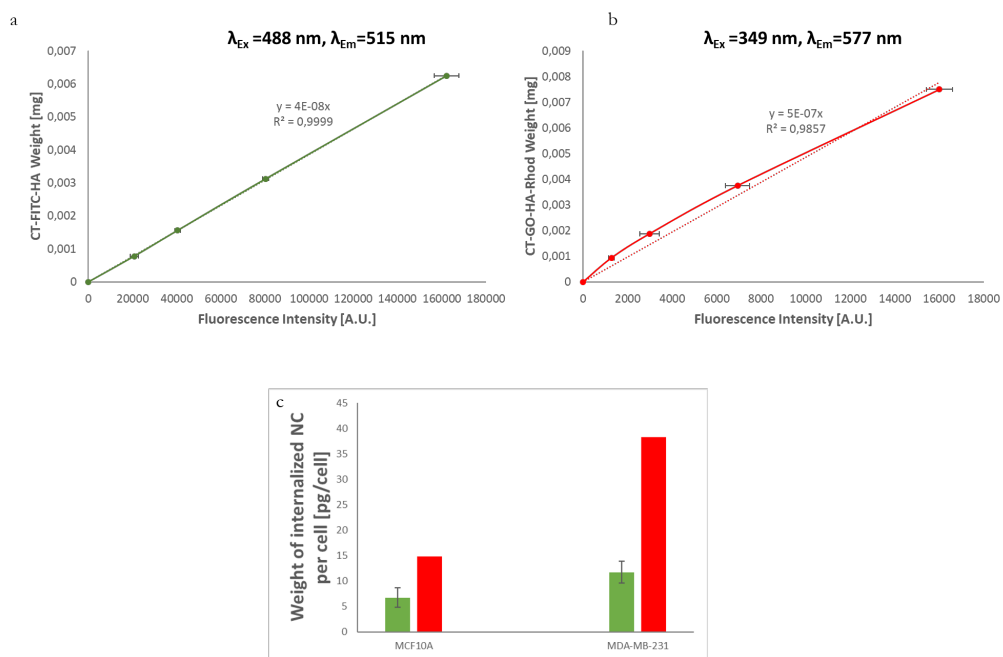


Figure 4.9: Calibration curves of Bilayer 0.5%Oil-0.005%CT-FITC-0.12%HA in MCF10A cells and MDA-MB-231 cells b) Calibration curves of Bilayer 0.5%Oil-0.005%CT-FITC-0.12%GOQDsHA-Rhod in MCF10A cells and MDA-MB-231 cells, c) cell internalization

was assessed 24 h after incubation with different NPs systems in HDF cells. As reported in Fig.4.10, at the concentration of 0.01 mg/ml, all NP systems here investigated possess no significant toxic effects on viability of both HDFs and MCF7 cell. Representative confocal images of HDFs incubated with GOQDs-

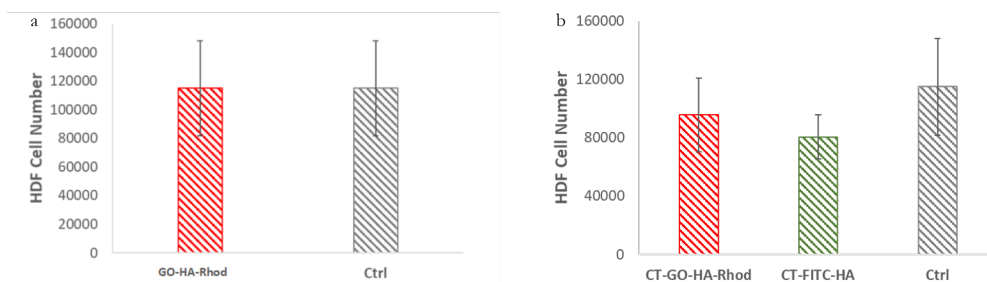


Figure 4.10: Cell viability of a) HDFs cell treated with 0.01mg/ml of GOQDs-HA-Rhod. and b) HDFs cell treated with 0.01mg/ml of Bilayer 0.5%Oil-0.005%CT-FITC-0.12%HA and 0.01 mg/ml Bilayer 0.5%Oil-0.005%CT-FITC-0.12%GOQDsHA

HA-Rhod, CT-GO-HA-Rhod and CT-FITC-HA are reported in Fig. 4.11. The overlap coefficient between the three NP systems and lysosomes was calculated and resulted to be almost 0.9 for GOQDs-HA-Rhod and CT-FITC-HA and greater than 0.7 for CT-GO-HA-Rhod. The accumulation of all three NP systems in lysosomes indicates that they are mainly delivered by classical endocytosis.

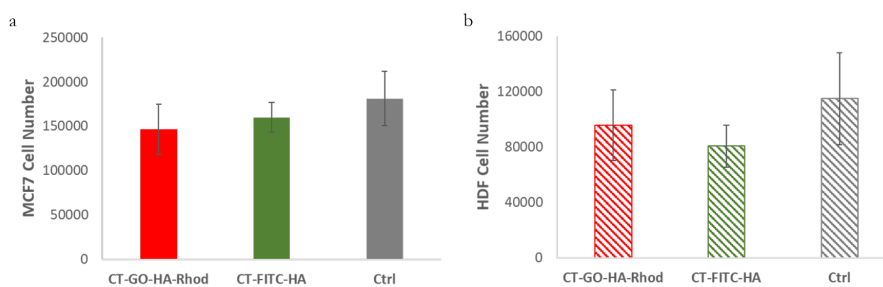


Figure 4.11: Confocal images of HDFs incubated with GOQDs-HA-Rhod, Bilayer 0.5%Oil-0.005%CT-0.12%GOQDsHA-Rhod and Bilayer 0.5%Oil-0.005%CT-FITC-0.12%HA

4.5 Conclusion

Nanoparticles have the potential to revolutionize modern therapies of many diseases, including cancer by the potential to combine in a single system, nanoscale, therapeutic and imaging agents making the therapy process effective and detectable in real-time. However, in rationally designing a system for nanomedicine, both the heterogeneous and complex tumor microenvironment and the physiological barriers of the organism must be carefully considered. Generally, systems with dimensions greater than 100 nm can selectively accumulate in tumor tissues by exploiting the high permeability of a growing tumor mass, but have poor diffusion in the dense collagen matrix of the interstitial space, resulting in restrictive nanoparticle accumulation around tumor blood vessels and little penetration into the tumor parenchyma. On the other hands, 10-30 nm nanoparticles show high cellular uptake, but can be easily sequestered by the mononuclear phagocytic system and eliminated. To overcome this problem, we have designed a multistep approach where GOQDs-HA were deposited on an O / W emulsion coated with a layer of chitosan through a layer-by-layer technique optimized for liquid templates. The GO-QDs-HA concentration required to stabilize the bilayer was determined through a saturation curve starting from concentrations of 0.05% w/v of QDs up to a concentration of 0.30% w/v. The bilayers obtained with a GOQDs-HA concentration of 0.12% showed the best stability, as evidenced by the measurements of the size at the nano tracking and the ζ potential at the DLS. The formed systems exhibited stability up to 180 days after their formation. In vitro test showed no evident cytotoxicity towards MCF7 HDFs cell lines despite the huge uptake shown in both cell lines.

4.6 Future Perspectives

The high stability of the obtained system makes it very interesting to continue the studies on this type of approach. However, the aim is to upgrade the system by integrating a stimuli-responsive degradation mechanism in order to make the release of the smallest nanoparticles highly controllable in terms of kinetics and selectivity. In particular, we thought of connecting the two nanocar-

riers through a responsive stimuli linker. Commonly this approach is implemented with biocompatible materials properly engineered to undergo a specific protonation, a hydrolytic rupture, a conformational change in response to a specific stimulus. Lowered interstitial pH, altered redox potential, and up-regulation of certain enzymes, are potentially endogenous stimuli associated with the tumor microenvironment. In particular, matrix metalloproteinase-2 (MMP-2) is a family of proteolytic enzymes playing a central role in tumor angiogenesis, progression, and invasion by the remodeling of the extracellular matrix (ECM)[32]. These enzymes, also known as gelatinase A, hydrolyze type IV collagen, which is a major constituent of tumor ECM. Iaccarino et al. in 2019 proposed a cross-linked polyelectrolyte nanocapsules based on an oil-core loaded with hydrophobic drugs and a matrix metalloproteinase-2 (MMP-2)-cleavable shell[33]. They tested the nanocapsules on 3D tumor and healthy spheroid models, and founded that the high level of MMP-2 enzymes expressed by tumor spheroids catalyzed the disassembly of the nanocapsules, which ultimately did lead to drug release. Inspired by this work, we planned to coat O/W NE with an additional layer of hyaluronic acid functionalized with a modified peptide containing the metalloprotease sensitive amino acid sequence and a terminal lysine containing an azido group. Instead, the GOQDs will be coated with functionalized alkyne hyaluronic acid. Based on the biocompatible copper free azido-alkyne click reaction, we can obtain, through an additive approach, a system with GOQDs tailor-made release profiles with excellent spatial and temporal control. Furthermore, we will better study the interaction of obtained GOQDs with NIR light and the ability to transform it into heat, to combine the high capacity of drug loading and release with photothermal therapy.

References

- [1] Chaturvedi VK, Singh A, Singh VK, Singh MP. Cancer nanotechnology: a new revolution for cancer diagnosis and therapy *Curr Drug Metab* 2019;20(6):416-29-88.
- [2] He L, Huang Y, Zhu H, Pang G, Zheng W, Wong Y, et al. Cancer-Targeted Monodisperse Mesoporous Silica Nanoparticles as Carrier of Ruthenium Polypyridyl Complexes to Enhance Theranostic Effects; *Adv Funct Mater* 2014;24(19):2754-63.
- [3] Muthu MS, Kulkarni SA, Raju A, Feng S-S. Theranostic liposomes of TPGS coating for targeted co-delivery of docetaxel and quantum dots; *Biomaterials* 2012;33(12):3494-501.
- [4] Lee JY, Kim J, Bae KH, Oh MH, Kim Y, Kim JS, et al. Low-Density Lipoprotein-Mimicking Nanoparticles for Tumor-Targeted Theranostic Applications; *Small* 2015;11(2):222-31.
- [5] Zhu L, Zhou Z, Mao H, Yang L. Magnetic nanoparticles for precision oncology: theranostic magnetic iron oxide nanoparticles for image-guided and targeted cancer therapy.; *Nanomedicine* 2017;12(1):73-87.
- [6] Jing L, Liang X, Li X, Lin L, Yang Y, Yue X, et al. Mn-porphyrin conjugated Au nanoshells encapsulating doxorubicin for potential magnetic resonance imaging and light triggered synergistic therapy of cancer; *Theranostics* 2014;4(9):858.
- [7] Doane TL, Burda C. The unique role of nanoparticles in nanomedicine: imaging, drug delivery and therapy; *Chem Soc Rev.* 2012;41(7):2885-911.

- [8] Wong C, Stylianopoulos T, Cui J, Martin J, Chauhan VP, Jiang W, et al. Multi-stage nanoparticle delivery system for deep penetration into tumor tissue; *Proc Natl Acad Sci USA* 2011;108(6):2426-31.
- [9] Jin Y, Jia C, Huang S-W, O'donnell M, Gao X. Multifunctional nanoparticles as coupled contrast agents; *Nat Commun* 2010;1(1):1-8.
- [10] Yan Y, Bjornmalm M, Caruso F. Assembly of layer-by-layer particles and their interactions with biological systems; *Chem Mater* 2014;26(1):452-60.
- [11] Johnston APR, Cortez C, Angelatos AS, Caruso F. Layer-by-layer engineered capsules and their applications; *Curr Opin Colloid Interface Sci* 2006;11(4):203-9.
- [12] Fleige E, Quadir MA, Haag R. Stimuli-responsive polymeric nanocarriers for the controlled transport of active compounds: concepts and applications; *Adv Drug Deliv Rev* 2012;64(9):866-84.
- [13] Vecchione R, Ciotola U, Sagliano A, Bianchini P, Diaspro A, Netti PA. Tunable stability of monodisperse secondary O/W nano-emulsions; *Nanoscale*. 2014;6(15):9300-7.
- [14] Vecchione R, Quagliariello V, Calabria D, Calcagno V, De Luca E, Iaffaioli R V, et al. Curcumin bioavailability from oil in water nano-emulsions: In vitro and in vivo study on the dimensional, compositional and interactional dependence; *J Control Release* 2016;233:88-100.
- [15] Vecchione R, Quagliariello V, Giustetto P, Calabria D, Sathya A, Marotta R, et al. Oil/water nano-emulsion loaded with cobalt ferrite oxide nanocubes for photo-acoustic and magnetic resonance dual imaging in cancer: in vitro and preclinical studies; *Nanomedicine Biol Med* 2017;13(1):275-86.
- [16] Lerf A, He H, Forster M, Klinowski J. Structure of graphite oxide revisited; *J Phys Chem B* 1998;102(23):4477-82.
- [17] Jun SW, Manivasagan P, Kwon J, Nguyen VT, Mondal S, Ly CD, et al. Folic acid-conjugated chitosan-functionalized graphene oxide for highly effi-

- cient photoacoustic imaging-guided tumor-targeted photothermal therapy; *Int J Biol Macromol* 2020;155:961-71.
- [18] Tufano I, Vecchione R, Netti PA. Methods to Scale Down Graphene Oxide Size and Size Implication in Anti-cancer Applications; *Front Bioeng Biotechnol* 2020;7(8):1381-45.
- [19] Gonçalves G, Vila M, Portolés MT, Vallet-Regi M, Gracio J, Marques PAAP. Nano-graphene oxide: A potential multifunctional platform for cancer therapy; *Adv Healthc Mater* 2013;2(8):1072-90.
- [20] Zhang H, Li Y, Pan Z, Chen Y, Fan Z, Tian H, et al. Multifunctional Nanosystem Based on Graphene Oxide for Synergistic Multistage Tumor-Targeting and Combined Chemo-Photothermal Therapy; *Mol Pharm* 2019;16(5):1982-98.
- [21] Depan D, Shah J, Misra RDK. Controlled release of drug from folate-decorated and graphene mediated drug delivery system: Synthesis, loading efficiency, and drug release response.; *Mater Sci Eng C* 2011;31(7):1305-12.
- [22] Weissleder R. A clearer vision for in vivo imaging; *Nat Biotechnol* 2001;19(4):316-317.
- [23] Gonçalves G, Vila M, Bdikin I, De Andrés A, Emami N, Ferreira RAS, et al. Breakdown into nanoscale of graphene oxide: Confined hot spot atomic reduction and fragmentation; *Sci Rep* 2014;4(1):1-8.
- [24] Sun X, Liu Z, Welsher K, Robinson JT, Goodwin A, Zaric S, et al. Nano-graphene oxide for cellular imaging and drug delivery; *Nano Res* 2008;1(3):203-12.
- [25] Kim HC, Park WH. Fluorescent property of glycol chitosan-fluorescein isothiocyanate conjugate for bio-imaging material; *Int J Biol Macromol* 2019;135:1217-21.
- [26] Bolte S, Cordelières FP. A guided tour into subcellular colocalization analysis in light microscopy; *J Microsc* 2006;224(3):213-32.

- [27] Dash M, Chiellini F, Ottenbrite RM, Chiellini E. Chitosan-A versatile semi-synthetic polymer in biomedical applications; *Prog Polym Sci* 2011;36(8):981-1014.
- [28] Lal S, Hall RM, Tipper JL. Concentration and size distribution data of silicon nitride nanoparticles measured using nanoparticle tracking analysis; *Data Br* 2017;15:821-23.
- [29] Amaro-Gahete J, Benítez A, Otero R, Esquivel D, Jiménez-Sanchidrián C, Morales J, et al. A comparative study of particle size distribution of graphene nanosheets synthesized by an ultrasound-assisted method; *Nanomaterials* 2019;9(2):152.
- [30] Guidetti G, Cantelli A, Mazzaro R, Ortolani L, Morandi V, Montalti M. Tracking graphene by fluorescence imaging: A tool for detecting multiple populations of graphene in solution; *Nanoscale* 2016;8(16):8505-11.
- [31] Li Y, Sun H, Shi F, Cai N, Lu L, Su X. Multi-positively charged dendrimeric nanoparticles induced fluorescence quenching of graphene quantum dots for heparin and chondroitin sulfate detection; *Biosens Bioelectron* 2015;74:284-90.
- [32] Egeblad M, Werb Z. New functions for the matrix metalloproteinases in cancer progression; *Nature Reviews Cancer* 2002;2(3):161-174.
- [33] Iaccarino G, Profeta M, Vecchione R, Netti PA. Matrix metalloproteinase-cleavable nanocapsules for tumor-activated drug release; *Acta Biomater* 2019;89:265-78.

Chapter 5

Conclusion

Nanotechnology has been recognized in 2006 by the National Cancer Institute as the science that can effectively change the basis for the diagnosis, treatment, and prevention of cancer, allowing the study and treatment of this disease at a molecular scale, in real-time and during the early stages of the process. 2D nanomaterials possess special physicochemical properties (e.g., light, ultrasonic and magnetic responses) and biological behaviors such as endocytosis, biodistribution, biodegradation, and excretory pathways, which lead to their use in various biomedical applications. In particular, among 2D nanomaterials, graphene and its derivatives have attracted enormous attention in cancer diagnosis and therapy because they combine, in a unique material, extremely small size, NIR absorption, delocalized electrons, extremely high surface area, and versatile surface functionality. GO, initially considered as an intermediate of one of the graphene production processes, has become a material that can be considered both for fundamental research and for its potential applications. GO is one of the most explored materials in nanomedicine due to its extraordinary intrinsic properties. The GO has a high surface area that can be exploited for the loading of drugs and biomolecules, forms stable colloidal dispersions in water and its structure contains a variety of oxygenated functional groups useful for the covalent modification. Furthermore, GO has interesting optical properties useful for phototherapy and biomedical imaging. Known since the beginning of the last century, the oxidation of graphite with strong oxidants in

concentrated acid media remains the most commonly used method to produce GO on a large scale. However, this method raises many concerns regarding the large quantities of acids required and the costs of disposing of acidic waste water containing metal impurities from the oxidants used. It is in this direction that the first efforts of this research work were devoted. Indeed, we developed a new method to obtain nano-GO in the absence of acid, by combination of mechanical grinding (ball milling) and photo-Fenton reaction. Obtaining GO sheets with narrow size distribution in the nanometer range is very desirable especially for the nascent biomedical applications of GO. As is known, the physicochemical properties of the material, in particular the lateral dimensions, influence both the optical properties and the absorption and cellular response. Therefore, size is one of the first factors to check when considering GO as a therapeutic platform. Considering the importance of reducing the lateral size of GO nanosheet below 50 nm, we used an environmentally friendly oxidative cutting with hydrogen peroxide and ammonia with uniform lateral dimensions of less than 20 nm were synthesized using Then the surface of the nano-GO nanoparticles was functionalized with hyaluronic acid (GOQDs-HA) to increase biocompatibility and to exploit the active targeting properties of this natural polymer. This GOQDs-HA showed a high loading capacity of Curcumin, select as a model pharmacological molecule and a high cellular internalization so they GOQDs-HA could be explored as the ideal nanocarriers for drug delivery. nano-GO platforms are widely explored for combined anticancer therapies. Indeed, together with the ability to accumulate a large amount of drug, for high surface development, they can be photo-stimulated producing heat and CO₂, which both induce cell death. Moreover, they can be detected for their photo-luminescence properties providing the possibility to have a theranostic tool. All these features represent an important goal for next-generation cancer treatments as they allow a controlled and higher death rate of cancer cells with a lower dose of the drug, minimizing side effects and multidrug resistance. However, the other side of the coin is that they can be easily sequestered by the mononuclear phagocytic system and eliminated due the small size. To overcome this limitation, a multistage platform was designed in wich graphene oxide nanosheets coated with hyaluronic acid (GOQDs-HA) are deposited through a Layer by Layer tech-

nique on an Oil / Water emulsion (O/W NE) coated with a layer of a biodegradable polymer, chitosan. In this complex system, NE O/W has the potential to remain stable during blood circulation and accumulate preferentially in tumor tissues due to enhanced permeability and retention. After extravasation in the tumor tissue, the degradation of the polymeric matrix should allow the release of GOQDs-HA which, having dimensions around 12 nm and an active targeting system given by hyaluronic acid on their surface, can easily diffuse in the tissue and selectively recognize and penetrate cancer cells. Taken altogether the results of this work of thesis encourage the use nano-Graphene Oxide for the implementation of engineered theranostic systems for nanomedicine.